INTEGRATED CONVERTER FOR PLUG-IN ELECTRIC VEHICLES

Ph.D. THESIS

by

ANKIT KUMAR SINGH

DEPARTMENT OF ELECTRICAL ENGINEERING
INDIAN INSTITUTE OF TECHNOLOGY ROORKEE
ROORKEE – 247667 (INDIA)
JUNE, 2018

INTERGRATED CONVERTER FOR PLUG-IN ELECTRIC VEHICLES

A THESIS

Submitted in partial fulfilment of the requirements for the award of the degree

of

DOCTOR OF PHILOSOPHY

in

ELECTRICAL ENGINEERING

by

ANKIT KUMAR SINGH

DEPARTMENT OF ELECTRICAL ENGINEERING
INDIAN INSTITUTE OF TECHNOLOGY ROORKEE
ROORKEE – 247667 (INDIA)
JUNE, 2018

INDIAN INSTITUTE OF TECHNOLOGY ROORKEE
ROORKEE

CANDIDATE'S DECLARATION

I hereby certify that the work which is being presented in this thesis entitled **"INTEGRATED CONVERTER FOR PLUG-IN ELECTRIC VEHICLES"** in partial fulfilment of the requirements for the award of the Degree of Doctor of Philosophy and submitted in the Department of Electrical Engineering of the Indian Institute of Technology Roorkee, Roorkee is an authentic record of my own work carried out during a period from July, 2014 to June, 2018 under the supervision of Dr. M.K Pathak, Associate Professor, Department of Electrical Engineering, Indian Institute of Technology Roorkee, Roorkee.

The matter presented in this thesis has not been submitted by me for the award of any other degree of this or any other Institution.

(ANKIT KUMAR SINGH)

This is to certify that the above statement made by the candidate is correct to the best of my knowledge.

(M. K. Pathak)
Supervisor

Dated:

ABSTRACT

This thesis is focused on evolution, analysis and design of improved single-stage based integrated converters (achieving all modes of vehicle operation, i.e., plug-in charging, propulsion and regenerative braking using single-converter) for on-board applications of plug-in electric vehicles (PEVs).

The research work in this thesis is divided into development of four integrated converter topologies, each one of which is briefly discussed below.

The first proposed topology is a ZETA-SEPIC based integrated converter. It operates as ZETA converter during plug-in charging and regenerative braking modes (battery charging operation), and as SEPIC converter for propulsion mode. Due to ZETA and SEPIC operation, the converter has buck/boost capabilities in each mode; The battery can therefore be charged from universal input voltage. Further, the stored mechanical energy can be captured entirety to charge battery during regenerative braking of vehicle. During propulsion mode, the dc-link voltage can be controlled for wide range of battery voltages. Moreover, in this converter only one switch operates for any given mode which simplifies the control implementation. The theoretical efficiency of the converter in plug-in charging, propulsion and regenerative braking modes are computed and compared with existing integrated converters. This converter is then evaluated for voltage and current stresses on semiconductor devices during above-mentioned modes of operation. It has a limitation of high voltage/current stresses (sum of input/output quantities (voltage/current)) on semiconductor devices. The voltage stress on semiconductors in propulsion and regenerative braking modes are a sum of dc-link voltage and battery voltage usually higher than plug-in charging mode (sum of grid voltage and battery voltage). The power rating of converter in propulsion mode is usually much higher than other two modes; therefore, high stresses in propulsion mode are downside for vehicle application.

To overcome above-mentioned limitation of ZETA-SEPIC converter, another modified ZETA based integrated converter has been proposed, which has lower stresses in propulsion and regenerative modes. Also, the proposed converter has higher efficiency in these two modes compared to other existing integrated converters . Efficiency improvement in these two

modes leads to a longer run of vehicle. The peak efficiencies of propulsion and regenerative braking modes are 97.2% and 98.1%, respectively.

To take forward this work, another integrated converter is developed from conventional SEPIC which has also lower stresses (in propulsion and regenerative braking modes) same as the modified ZETA based converter. Moreover, this converter utilizes a nonlinear carrier control method which saves voltage sensor requirement for power factor correction (PFC) in continuous conduction mode (CCM) operation. Reduction of feedback circuitry enhances compactness of the converter making it more suitable for on-board charger (OBC). The control scheme for PFC gives high power factor (PF) and low total harmonic distortion (THD) for both simulation and experimental validation. Further, converter stress and loss analysis have been carried out for selection of proper rating of semiconductor devices. The total losses of the proposed converter in ac/dc (plug-in charging) and dc/dc (propulsion and regenerative braking) stages have been found close to their conventional counterparts. It is due to the fact that both in ac/dc and dc/dc stages, one additional mechanical switch in the current path compared to conventional converters, and calculated loss in mechanical switch is negligible compared to semiconductor devices and passive components.

An integrated converter has been derived from conventional two-switch buck/boost converter capable of operating for charging, propulsion and regenerative modes have been further investigated. The main advantage of this integrated converter is a peak efficiency improvement in propulsion boost and regenerative buck modes compared to an existing integrated converter which is most competent to the proposed converter, and low voltage/current stresses in each mode. Efficiency improvements in aforementioned modes are desirable in vehicle applications because the occurrence of these modes is more common than propulsion buck and regenerative boost modes. Moreover, this converter has two inductors but the size of the second inductor, i.e., L_2 is approximately reduced by more than 25% compared to existing integrated converter.

All the proposed converters are verified through simulation and experiment undertaken using laboratory prototype. The waveforms obtained from simulation and experiment are presented in this thesis.

ACKNOWLEDGMENTS

It is my desire and a great pleasure to offer my sincere thanks to all those who have contributed, in whatever way, to the completion of my work.

First, I take this opportunity to express my sincere gratitude to my supervisor Dr. M. K.Pathak, Associate Professor, Department of Electrical Engineering, Indian Institute of Technology (IIT) Roorkee, Roorkee, India for his constant encouragement and motivation throughout the duration of this research work. I also express my sincere gratitude to Dr. G.K. Singh, Professor, Department of Department of Electrical Engineering, IIT Roorkee, India who constantly encouraged me during my Ph.D programme.

I am also thankful to my research committee members, Prof. S.P. Singh and Prof. B.K. Kaushik, for their constructive suggestions during several meetings held for this research work. I would also like to thank the Head of the Department and other faculty members of Electrical Engineering Department, IIT Roorkee for their moral support and providing the excellent laboratory facilities during this research work at IIT Roorkee. I would thank the Ministry of Human Resources Development (MHRD), Government of India for providing the fellowship for carrying out this research work. I would like to thank the anonymous reviewers of my research work, who gave me the suggestions to improve the quality of the research work and the direction for the additional work.

My journey in IIT Roorkee has been blessed with many friends who played a major role in maintaining a constantly high level of motivation, and thus help me in the progress of my work. I would give special acknowledgment to my fellow researchers, Mr. Vishwanatha Siddhartha, Mr. Y. Srinivasa Rao, Dr. Aurbindo Panda, Mr. Santosh Kumar Singh, Mr. Saran Satsangi, Mr. Praveen Kumar, Mr. Sandeep Hanwate, Mr. Ajay Kumar Maurya and Dr. Manmohan Garg.

I wish to express my hearty gratitude to my parents and all my family members, for their endless moral support and encouragement. Finally, I am very thankful to all-merciful God who gave me blessing and wisdom to carry out this Ph.D. research work.

(Ankit Kumar Singh)

CONTENTS

LIST OF FIGURES

LIST OF TABLES

LIST OF ABBREVIATIONS

ac	Alternating Current
CCM	Continuous Conduction Mode
DCM	Discontinuous Conduction Mode
EMC	Electromagnetic Compactiblity
EMF	Electromagnetic Force
EMI	Electromagnetic Interefernce
EVs	Electric Vehicles
FPGA	Field Programming Gate Array
ICEs	Internal Combustion Engines
NLCC	Nonlinear Carrier Control
OBC	On-board Charger
PCB	Printed Circuit Board
PEVs	Plug-in Electric Vehicles
PF	Power Factor
PFC	Power Factor Correction
PI	Proportional Integral
PLL	Phase-Locked Loop
PMSM	Permanent Magnet Synchronous Motor
PV	Photovoltaic
PWM	Pulse Width Modulation
RMS	Root Mean Square
SAE	Sociaty of Automtive Enginners
SOC	Sate of Charge
SRM	Switch Reluctance Motor
THD	Total Harmonic Distortion
TSBuB	Two-Switch Buck/Boost
UPF	Unity Power Factor
V2G	Vehicle to Grid

CHAPTER 1

INTRODUCTION

1.1 Background and Motivation

Land transport sector mainly depends on oil products. Several actions have been taken in order to mitigate this dependency. On one hand, public transport has been developed as electric trains (trams, subway and high speed trains). On other hand, efficiency of private transport has been improved by reducing the weight of vehicle by using more efficient internal combustion engines (ICEs). However, the improvements in the ICEs technology are not enough to significantly reduce oil consumption. In this direction, researchers and carmakers have been working on several options including vehicles powered by biodiesel, ethanol, compressed natural gas (CNG), liquefied natural gas (LNG), hydrogen, compressed air, electric vehicles (EVs), etc.

Recent developments have led to penetration of EVs into market as an alternative to conventional vehicles employing ICEs. Enabling policy of developed as well as developing countries and ever-growing need to curb air pollution of cities has created most suitable environment for these developments. Several countries have established emission standards which are designed to limit the pollutant emissions of upcoming vehicles sold in the countries. Furthermore, growing research in the battery technology provides improved and more affordable batteries for upcoming EVs; hence, the overall cost of EVs is reducing fast. It is expected that sales of EVs will grow continuously for two main reasons: economy of scale and new developments in the battery technology. As for the economy of scale, some companies have established battery manufacturing facility of their own to cut its costs. Moreover, it must be noted that batteries are being widely used in distributed generation, unmanned vehicle aviation applications, etc., and their cost is bound to fall rapidly.

Most of the EVs are charged through a direct connection between vehicle and low voltage distribution network and this type of EVs which are connected to the grid, known as plug-in electric vehicles (PEVs). The PEVs can be classified, mainly plug-in hybrid electric vehicles (PHEVs), battery electric vehicles (BEVs) and fuel cell plug-in hybrid electric vehicles (FC-

PHEV). On other hand, vehicles such as hybrid electric vehicles (HEVs) are not considered as PEVs. As the batteries of these types of vehicles are charged with internally generated electricity by ICE and they need not be charged from the grid.

The PEVs are now a promising solution to curb the air pollution that uses pollution free battery power to produce clean energy for the vehicle [1]. The PEVs are a combination of add-on charger, battery and the inverter-drive system [2–5]. Battery plays a critical role in the evolution of PEVs. Its cost, weight, energy density, charging time and lifetime are still challenges for full commercialization. As the charging time and lifetime of the battery have a strong reliance on the characteristics of the battery chargers [6–16]. The battery chargers for on-board applications have to be small and light since it is placed into vehicles. Therefore, in this direction researchers across the world are working to develop and design of compact charging system for PEVs.

1.2 Literature Review

This Section focuses on classification of battery chargers, and literature review of single-stage based chargers for on-board applications. The single-stage chargers are classified into conventional and integrated chargers. These chargers generally employ non-isolated converters which are suitable for compact charging system for on-board charger (OBC).

1.2.1 Classification of chargers

Two types of battery chargers are employed for PEVs; stand-alone (off-board) charger and OBC. Off-board charging system is used when higher charging power is required. The size and weight of the charger are easier to handle with an off-board charger. The OBC is more prevalent because it is placed inside the vehicle; therefore, vehicle can be charged anywhere [17,18]. The desired features of OBC are light weight, high power density and high efficiency [15, 19]. The OBC may have two-stage converter (Fig. 1.1) or single-stage converter (Fig. 1.2), but due to a large number of components in two-stage chargers [3, 20–25], the single-stage chargers [26–30] are more attractive for on-board applications, even though it suffers from low frequency battery current ripple. The OBC adds weight, volume, and cost to the vehicle; therefore, usually, it is designed for power levels ($\leq$ 3.5 kW) [30, 31]. However, a two-stage converter using transformer as an isolation is a common rule in OBC

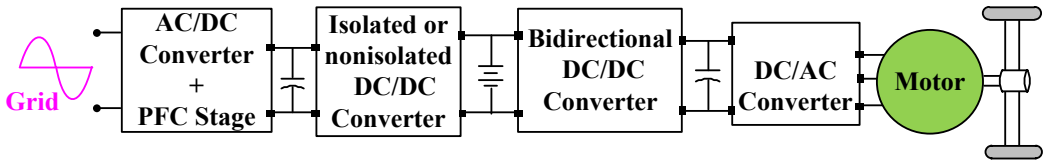

Fig. 1.1. Block diagram of conventional two-stage EV battery charger

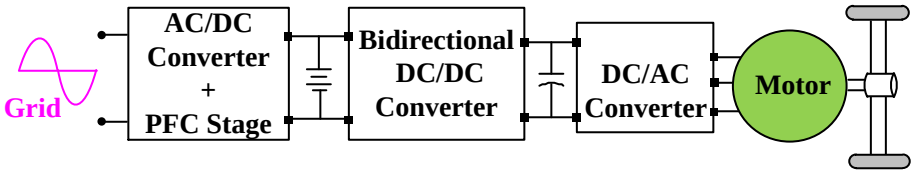

Fig. 1.2. Block diagram of single-stage EV battery charger

design. Moreover, a high-frequency transformer for wide-range output voltage and galvanic isolation has a negative impact on efficiency and power density [32–34]. As such, there is no requirement of isolation for the safety of EVs as per SAE (Society of Automotive Engineers) J1772 [18] . Also, there is no electrical constraint that the battery should be isolated from ac input, because its ground is generally floating with the body ground of the vehicle [18]. Nevertheless, from the safety point of view, a relay protective circuit can be added at the output battery terminals. Another classification of chargers is described in terms of power levels and charging time. The choice of classification is based on nationally available power levels [20], which is shown in Table 1.1. Further, chargers are also classified as: unidirectional charger and bidirectional charger.

Unidirectional charger can charge the battery but can not inject energy into the grid. Usually, these chargers are implemented in a single-stage to limit cost, weight, volume, and losses. The block diagram of single-stage charger (Fig. 1.2) is a typical example of unidirectional chargers. High-frequency isolation transformers can be employed when desired. Simplicity in the control of unidirectional chargers makes it relatively easy for an utility to manage heavily loaded feeders due to multiple EVs. With a high penetration of EVs and active control of charging current, these chargers can meet most utility objectives while avoiding cost, performance, and safety concerns associated with bidirectional chargers [35, 36].

A bidirectional charger supports charging from the grid, battery energy can be injected

Table 1.1. Charger classification in terms of power levels

Power level types	Charger location	Typical uses of place	Power level	Charging time
Level-1				
120 Vac (US)	On-board, 1-phase	Charging at home	1.4 kW (12A)	4-11 hours
230 Vac (EU)			1.9 kW(20A)	11-36 hours
Level-2				
240 Vac (US)	On-board 1-or-3-phase	Charging at private or public outlets	4 kW (17A)	1-4 hours
400 Vac (EU)			8 kW (32A)	2-6 hours
Level-3				
(208-600 Vac or Vdc)	Off-board, 3-phase	Commercial or public	Commercial or public	0.2-0.5 hours

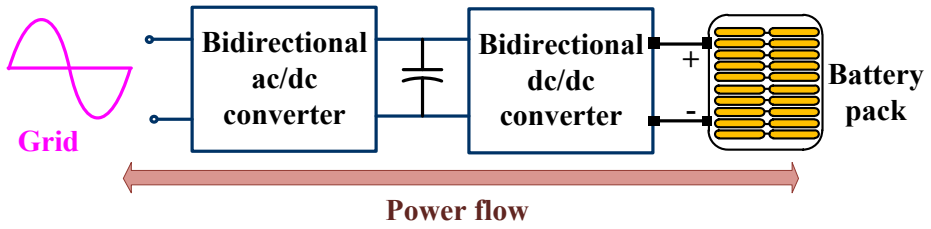

Fig. 1.3. Block diagram of bidirectional charger

back to grid, referred as vehicle-to-grid (V2G) operation mode. A typical block diagram of such charger is shown in Fig. 1.3. The bidirectional charger has two stages: an active grid connected bidirectional ac/dc converter that enforces power factor and a bidirectional dc/dc converter to regulate battery current. But bidirectional power flow limitations such as, battery degradation due to frequent cycling, high cost of a charger with bidirectional power flow capability, metering issues, and necessary distribution system up-gradation. Moreover, use of bidirectional charger will require extensive safety measures.

With a significant increase of PEVs, a single-stage based OBC can be more attractive than off-board charger because OBC avoids lesser deployment of off-board charging stations as well as controls crowd at the charging stations. To further reduce cost, weight and volume of the OBC, researchers have developed integrated type of chargers. Which can be classified as integrated chargers utilizing machine windings and traction converter into charging circuit, and integrated chargers incorporating bidirectional dc/dc converter into the charging circuit. In subsequent Sections, single-stage based chargers (conventional and integrated) are reviewed.

1.2.2 Conventional single-stage chargers

A systematic block diagram of a conventional single-stage charger has been shown in Fig. 1.2. In the following paragraph conventional single-stage chargers have been reviewed.

In [29], a SEPIC based converter has been proposed for OBC using three inductors and at least one additional inductor is required to achieve propulsion and regenerative braking modes. Therefore, an increase of magnetic components will have a negative effect on weight, cost and volume of the charger. Authors in [27] and [28] have proposed a Cuk converter based OBC using two inductors, and to achieve other modes of vehicle some additional components will be utilized. As a result, this charger is less suitable for on-board applications. A charger in [30] utilizes four switches, eight diodes and two inductors for charging operation. Therefore, this charger uses a number of active and passive components to accomplish all modes which results in an adverse effect on cost and compactness of the charger. Authors in [37] have proposed a bridgeless type front-end power factor correction (PFC) converter for a battery charger which uses four inductors hence this converter is not an adequate solution for compact OBC. However, this converter has high efficiency due to its bridgeless nature. A multi device based interleaved boost PFC converter has been proposed in [38]. This converter has four switches, six diodes and two inductors with only boosting capability. Therefore, the battery voltage, 200-450 V [10, 32] can not be charged from universal input voltage range (90-260 V). Authors in [26] have proposed a battery charger for wide range of battery voltage but it uses a number of passive components and semiconductor devices; therefore, the floor area of the charger will increase and less suitable for OBC applications. Authors in [39] have proposed an OBC for PEVs using isolated converter which utilizes a large number of active and passive components for charging operation. A zero voltage switching (ZVS) based interleaved boost converter has been proposed in [40] for efficiency improvement in plug-in charging mode which uses four auxiliary components, two switches, one capacitor and one inductor.

1.2.3 Integrated chargers utilizing machine windings into the charging circuit

In this type of integrated chargers, electric motor windings and traction converters are used in the charging with the help of some relays and mechanical switches, which eliminates the

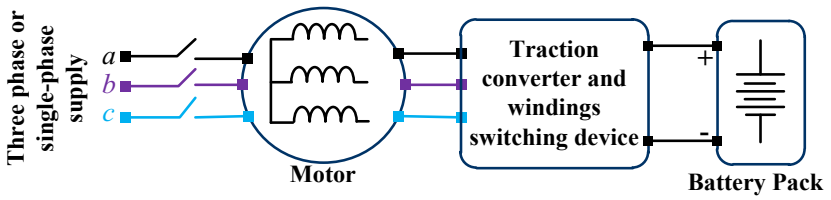

Fig. 1.4. Block diagram of an integrated charger utilizing machine windings into the charging circuit

use of extra converter (set of inductors and switches) for charging operation. This reduces the weight of charger because inductors are the heaviest components in converter compared to other components such as switches, diodes and capacitors. A block diagram of such charger shown in Fig. 1.4. The various types of these chargers have been reported in [15, 41–57]; these chargers are incidentally based on induction, permanent magnet and switch reluctance machines [58–66]. All these solutions mostly based on changing or rearranging the winding configuration of the motor, and inverter serves as a bidirectional ac/dc converter. These chargers use both single-phase and three-phase supplies; therefore, they can be used for both low power as well as high power charging applications. But, these chargers always operate in boost mode then to provide adequate voltage and current to the battery, a bidirectional dc/dc converter is utilized between dc-link and the battery [67–70]. And the addition of bidirectional dc/dc converter leads to add weight and cost to the charging system. Furthermore, these integrated chargers exhibit one or more of the following disadvantages: 1) difficulty in accessing the neutral point of windings; 2) applicability to a certain type of electric machines; 3) reduced reliability due to mechanical contacts and 4) control complexity and extra hardware are challenges to implementation in commercial products.

1.2.4 Integrated chargers incorporating bidirectional dc/dc converter into the charging circuit

A systematic block diagram of this type of integrated charger is shown in Fig. 1.5, which is derived from conventional single-stage charger. The bidirectional dc/dc converter connected between the battery and dc/ac converter [33, 71–78] is combined with PFC stage [4, 23, 37, 79–94] to have single power electronic converter for all modes. Therefore, a total number of components are reduced compared to conventional single-stage chargers because some of

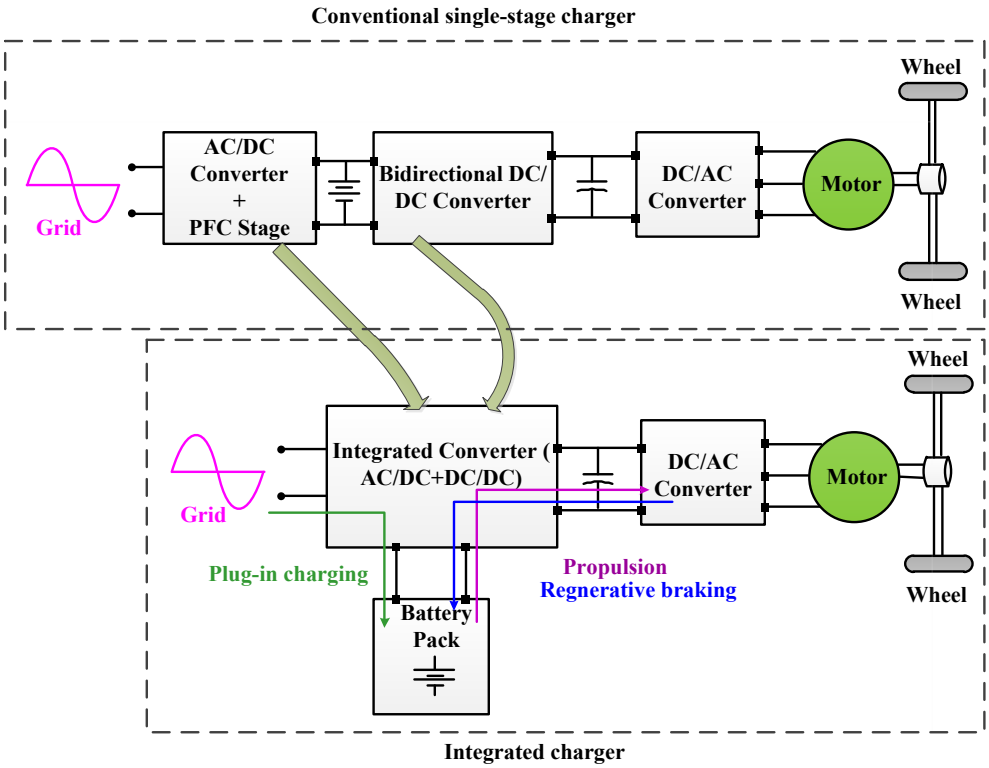

Fig. 1.5. Block diagram of an integrated charger utilizing dc/dc converter into the charging circuit

the switches, diodes and passive components are shared among the modes. Various types of these chargers are reported in [95–100], and all are reviewed. It is assumed that during charging period vehicle is not driven and during driving period, it is not possible to charge the battery pack except for regeneration braking period.

An integrated charger was proposed in [95], as shown in Fig. 1.6, for all modes of vehicle with buck/boost operation in each mode. The buck/boost operations of the converter allow more flexible control and capability of efficiently capturing regenerative braking energy. In addition to this, a wide range of battery voltage, i.e., 200-450 V can be charged from universal grid voltage. Moreover, in this converter, three or four semiconductor devices (depending on mode) are in the current path which increases conduction losses and reduces efficiency.

Authors in [96] have proposed an integrated charger using nine switches for any battery voltage levels, as shown in Fig. 1.7. The converter has bridgeless nature in plug-in charging mode; therefore, this converter avoid heat management problem of bridge rectifier and

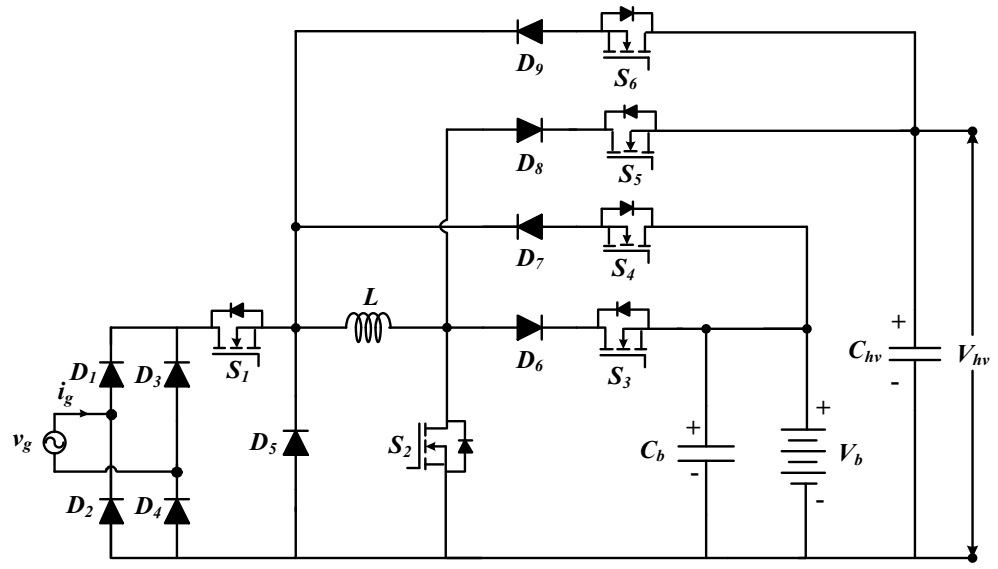

Fig. 1.6. Integrated charger [95]

associated losses. But presence of the large number of switches leads to less appealing for OBC application. Moreover, in this converter, a complex control strategy requires to turn on co-packed IGBT switches.

An integrated charger was in proposed in [97], as shown in Fig. 1.8 using four semiconductor switches, one mechanical switch and one inductor for all modes. The converter operates as an inverting buck/boost, boost and buck in plug-in charging, propulsion and regenerative braking modes, respectively. Moreover, this converter shows improvement over converter [95] in terms of a number of components and efficiency in each mode. Therefore, it

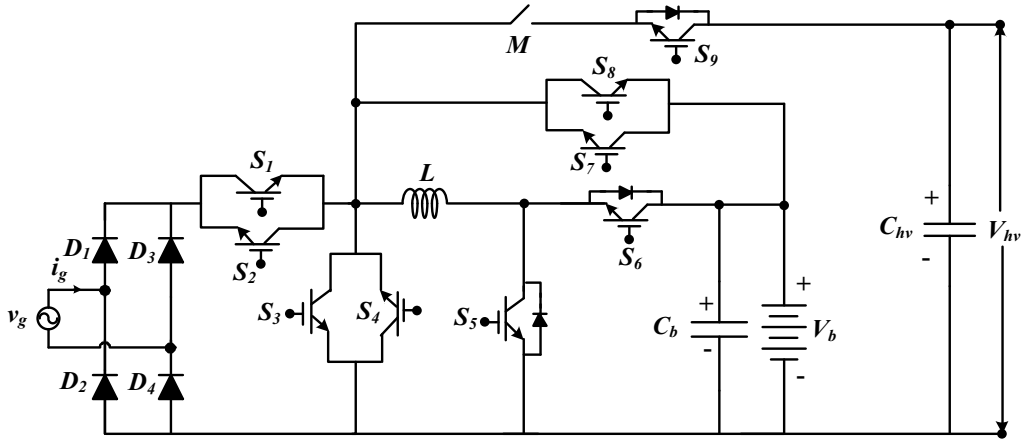

Fig. 1.7. Integrated charger [96]

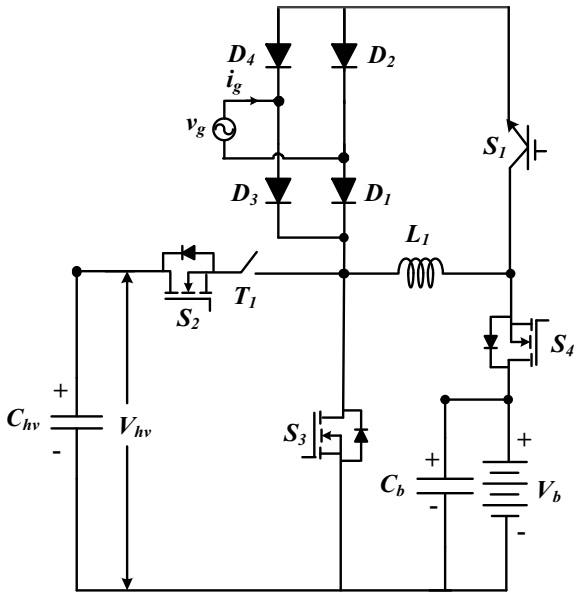

Fig. 1.8. Integrated charger [97]

is a low cost solution for manufacturers. Nevertheless, the major drawbacks of this converter are increased voltage and current stresses in semiconductors and increased current stress in magnetic component. Moreover, it has an additional conduction loss compared to their conventional counterpart (two-switch buck/boost converter [101]) in propulsion and regenerative braking modes due to the mechanical switch (T_1).

Dusmez and Khalig [98] have proposed an integrated charger, as shown in Fig. 1.9 using four switches and one inductor with one or two semiconductor devices (depends on mode) in the main current path. Therefore, each mode has same conduction and switching losses

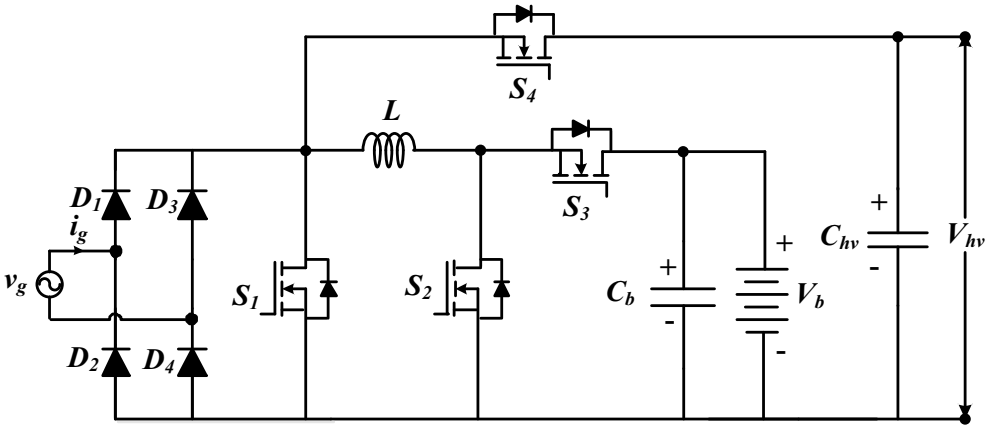

Fig. 1.9. Integrated charger [98]

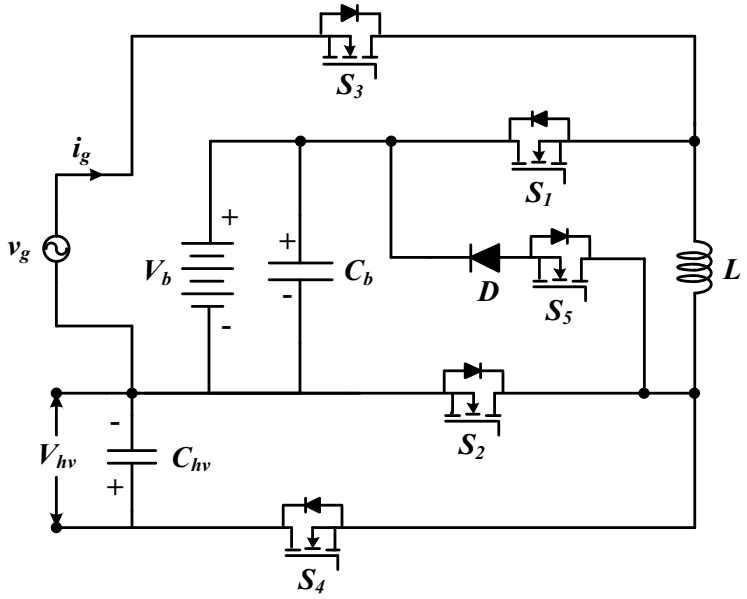

Fig. 1.10. Integrated charger [99]

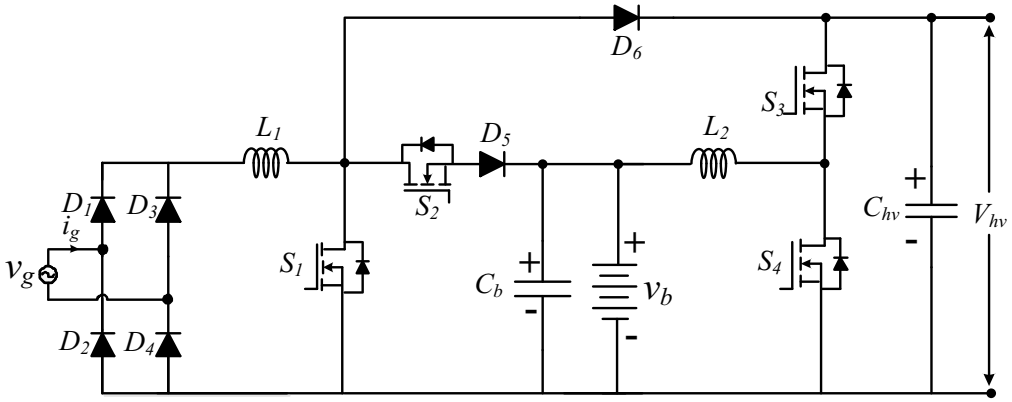

Fig. 1.11. Integrated charger [100]

compared to their conventional counterparts (single-switch boost converter or two-switch buck/boost converter). Moreover, this converter has low voltage/current stresses; resulting in lower losses and smaller heat sink, which ultimately results in miniaturization of the charger. Moreover, single current transducer is utilized in each mode (by sensing the inductor current); therefore, feedback circuitry reduces and making it more compact. But boost operation during charging; it is not possible to charge the battery when peak grid voltage becomes more than battery voltage.

Authors in [99] have proposed a charge non-linear carrier control based bridgeless inte-

grated charger shown in Fig. 1.10. The charge non-linear control based controller has been used in plug-in charging mode which requires only current feedback for PFC in continuous conduction mode (CCM). Therefore, reduction of feedback circuity leads to compactness of the charger. The bridgeless nature of the converter improves the converter efficiency in plug-in charging mode by reducing devices in the current path. But in a negative half cycle of the grid, the converter operates as conventional inverting buck/boost which results in high stresses on the components and leads to higher losses (conduction and switching losses). Therefore, the advantage of bridgeless nature is partially sacrificed in the negative half cycle of grid voltage. Moreover, none of the operational modes possesses both buck and boost capabilities leading to limited voltage range of battery and grid.

In [100], a quasi two-stage charger has been proposed for a wide range of battery voltage shown in Fig. 1.11. When the battery voltage $V_b >$ peak grid voltage $V_{g,max}$, the proposed converter operates as the conventional boost converter (single-stage operation) and when $V_b < V_{g,max}$, the battery draws power through two-stage conversion; therefore, it is named as quasi-two stage converter. Moreover, two-stage operation results in lower efficiency. This converter has slightly higher conduction losses in plug-in charging mode compared to conventional boost PFC converter, it is due to conduction of a additional switch. But this converter has lower switching losses due to its three-level output voltage characteristics. Moreover, in propulsion and regenerative braking modes, the proposed converter operates in boost and buck modes, respectively.

1.2.5 Comparison of integrated chargers

In this Section, a comparison of integrated chargers mentioned in Section 1.2.4 have been established based on voltage/current stresses on semiconductor devices and buck/boost operation of the converter in each mode along with the total number of components.

The stresses on semiconductor devices in each mode are tabulated in Table 1.2 where "High" denotes the sum of input/output quantities [$V_{out} + V_{in}$ and $I_{out} + I_{in}$] and "Low" denotes either input or output quantity [(V_{out} or V_{in}) and (I_{out} or I_{in})]. From Tables 1.2 and 1.3, the integrated charger [95] has both buck/boost operation and low stresses in each mode but at the expense of large number of semiconductor devices. The converter [96] has an

Table 1.2. Voltage and current stresses in semiconductors in each mode

Integrated chargers	**Plug-in charging**		**Propulsion**		**Regenerative braking**	
	Voltage	**Current**	**Voltage**	**Current**	**Voltage**	**Current**
Fig. 1.6	Low	Low	Low	Low	Low	Low
Fig. 1.7	Low	Low	Low	Low	Low	Low
Fig. 1.8	High	High	Low	Low	Low	Low
Fig. 1.9	Low	Low	Low	Low	Low	Low
Fig. 1.10	High	High	Low	Low	Low	Low
Fig. 1.11	Low	Low	Low	Low	Low	Low

Table 1.3. Comparative study of the integrated chargers in terms of buck/boost capabilities of each mode and number of components

Integrated chargers	**Mode of operation**			**Number of components**			
	Plug-in charging	**Propulsion**	**Regenerative braking**	**Switch**	**Diode**	**Inductor**	**Capacitor**
Fig. 1.6	Buck/boost	Buck/boost	Buck/boost	6	9	1	2
Fig. 1.7	Buck/boost	Buck/boost	Buck/boost	9	4	1	2
Fig. 1.8	Buck/boost	Boost	Buck	5	5	1	2
Fig. 1.9	Boost	Buck/boost	Buck/boost	4	4	1	2
Fig. 1.10	Boost or Buck/boost (negative half cycle)	Boost	Buck	5	1	1	2
Fig. 1.11	Boost	Buck/boost	Buck/boost	4	6	2	2

efficiency improvement over converter [95] by cutting the number of devices in the current path but cost of the charger increases due to increase number of switches. The charger [97] is an improvement over charger [95,96] in terms of the number of components. The charger [98] has fewer components compared to all existing converter as well as low stresses in each mode with only boost charging capability. The charger in [100] has buck/boost operation in plug-in charging mode but it requires a complex control strategy during this mode. Moreover, the two-stage operation of the converter during buck mode sacrifices its advantages.

From the above literature review, it is evident that there is a scope of further improvement in integrated converters by developing converters with have buck/boost capabilities in each mode, reduce the number of components and improve the efficiency in propulsion and regenerative braking modes so that vehicle can run for longer distance. In addition to this, reduction of complexity of feedback circuit will reduce size of the converter and improves reliability of the converter.

1.3 Objectives of the Thesis

Based on above-mentioned research gaps, the principle objective of this thesis is to develop improved integrated converters for on-board applications of PEVs with focus on one or more of the following points: reduction of active and passive components, improvement of operational efficiency, reduction of feedback element and buck/boost operations in each mode.

To accomplish this, the following research objectives have been formulated:

- The developed topologies have been analyzed for detailed operation, loss analysis, stress (voltage/current) analysis of switching devices and passive components design.
- Creation of computer simulation for each topology using MATLAB/Simulink software. Detailed simulation results are presented to verify the suitability of the converter for charging, propulsion and regenerative braking modes.
- Comparative analysis of the proposed integrated converters is carried out with existing integrated converters in terms of efficiency, number of components and buck/boost capabilities for each mode.
- A laboratory prototype has been developed using the field programming gate array

(FPGA) based dSPACE-1104 controller. The simulation results of the proposed converters have been validated through experimental results of the developed hardware.

1.4 Organization of Thesis

Apart from this chapter the thesis contains five more chapters and two Appendices. The works included in each chapter and appendix are briefly outlined as follows:

Chapter 2 presents a ZETA-SEPIC based integrated converters which operates as ZETA converter in plug-in charging and regenerative braking and as SEPIC converter in propulsion mode. Therefore, it is known as ZETA-SEPIC integrated converter. Due to both ZETA and SEPIC operations, the converter has buck/boost operation in each mode which is desirable for vehicle applications. Moreover, in the proposed converter only one switch conducts in each mode which provides easier control implementation.

Chapter 3 presents a new modified ZETA based integrated converter. The ZETA-SEPIC integrated converter in Chapter 2 has the problem of high voltage/current stresses on semiconductors in each mode. The voltage stress in propulsion and regenerative braking modes usually much higher than plug-in charging mode as well as high power rating of propulsion mode result in some of the semiconductor devices are in high stresses. As a result, converter reliability and devices lifetime are compromised. The proposed converter in this Chapter overcomes the limitation of high stresses in ZETA-SEPIC integrated converter in propulsion and regenerative braking modes. Moreover, this converter has higher efficiency in these two modes compared to other integrated converters.

Chapter 4 focuses on an integrated converter with reduced feedback part. A non-linear carrier control method is used for PFC operation which saves voltage sensor requirement for CCM operation. Reduction of feedback circuitry enhances compactness of the converter and provides more suitability to OBC.

Chapter 5 presents an integrated converter which has efficiency improvement in propulsion boost and regenerative braking modes compared to existing integrated converters. The efficiency improvement in these two modes leads to a longer distance covered by vehicle per charging. Moreover, this converter has low stresses in each mode.

Chapter 6 summarizes the conclusions drawn from the exhaustive simulation and exper-

imentation carried out for each converter topology.

Appendix A describes about simulation and experimental setups. Publications during the research work are provided in **Appendix B.**

1.5 Conclusion

This chapter is mainly focused on literature review of conventional single-stage and integrated chargers, thesis objectives and structure of the thesis. The conventional single-stage chargers operate only in charging mode; therefore, to achieve other modes a separate converter is utilized which adds weight and cost to the system. Therefore, these chargers are not attractive for OBC applications. In integrated chargers, it is attempted that all modes should be achieved through a single converter. The integrated chargers can be two types; first which utilizes machine winding and traction converter in charging circuit. In these chargers, both single-phase and three-phase supplies can be used for charging operation. Therefore, this type of integrated chargers can be used for low power as well as high power charging applications. But high power charging is not popular for on-board applications. These chargers usually operate in boost mode; therefore, to provide the adequate voltage and current to the battery some manufactures deploy a bidirectional dc/dc converter between dc-link and the battery which adds weight and cost to the charging system. Moreover, there is a difficulty to accessing neutral point of windings and extra hardware requires to implementation in commercial products. In second type of integrated chargers, bidirectional dc/dc converter which is placed between battery and dc-link, is incorporated into the charging circuit and does not pose any complexity to the charger. Therefore, it is much popular for OBC.

CHAPTER 2

ZETA-SEPIC BASED INTEGRATED CONVERTER

2.1 Introduction

This chapter focuses on development of a ZETA-SEPIC based integrated converter topology shown in Fig. 2.1. This topology is derived from conventional ZETA converter as shown in Fig. 2.2. The proposed integrated converter operates as a ZETA converter in plug-in charging and regenerative braking modes (battery charging operation), and as a SEPIC converter in propulsion mode. As both ZETA and SEPIC converters have buck/boost capabilities; therefore, the proposed converter has buck/boost capabilities in each mode. Therefore, a wide range of battery voltage (due to variation in SOC of the battery) can be charged from the grid. Moreover, the energy stored in the rotating parts can be fully captured during regenerative braking mode owing to buck/boost capabilities during this mode also. Further, this converter has fewer number of components compared to the existing converters which have buck/boost capabilities in all modes. The proposed converter is found to have higher efficiency in each mode compared to integrated converter (buck/boost capability in each mode) in [95]. As one switch is in operation during each mode, the controller implementation becomes simpler in this converter. For the purpose of selection of power switches, voltage/current stresses analysis and power loss analysis have been carried out for ac/dc and dc/dc conversion stages.

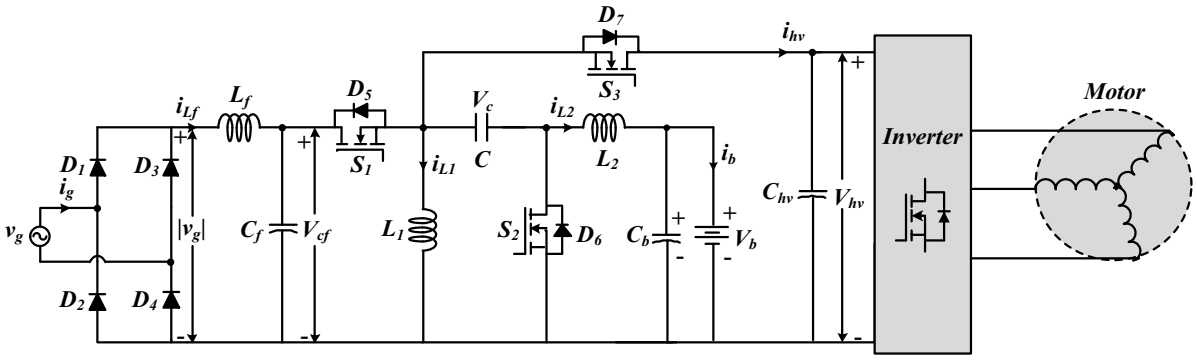

Fig. 2.1. Proposed ZETA-SEPIC based integrated converter for PEVs

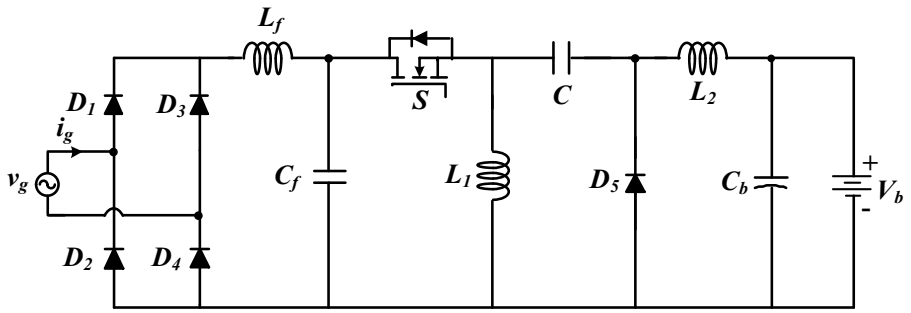

Fig. 2.2. Conventional ZETA converter for power factor correction

2.2 Conventional ZETA Converter

Fig. 2.2 shows circuit arrangement of conventional ZETA converter for PFC operation. The converter can operate in either CCM or discontinuous conduction mode (DCM). But for high power applications, e.g., PEVs, the DCM operation is not preferred because of high current stress produced in semiconductor devices which in-turn will necessitate use of high current rating devices. In addition, when converter operates in DCM, the electromagnetic interference (EMI) problem increases which may cause malfunctioning of other systems too. Therefore, the CCM operation of the converter is more prevalent for high power applications. The conventional ZETA converter with single switch can operate only in plug-in charging mode; to achieve other modes (propulsion and regenerative braking) some additional component(s) are employed. The operation of the proposed integrated converter are described in the following Section.

2.3 Operation of the Proposed Converter

The proposed integrated converter shown in Fig. 2.1 consists of three switches, four diodes three capacitors (excluding filter capacitor) and two inductors (excluding filter inductor). In the following Sections, operation of the converter is discussed using operational waveforms.

2.3.1 Plug-in charging mode

The plug-in charging mode of vehicle is possible only when vehicle is not in motion and then charger plug is connected to single phase supply socket to charge the battery.

In this mode, the proposed converter operates as ZETA PFC converter and switch S_1 is operated through PWM signal and remaining switches S_2 and S_3 are kept in OFF-state.

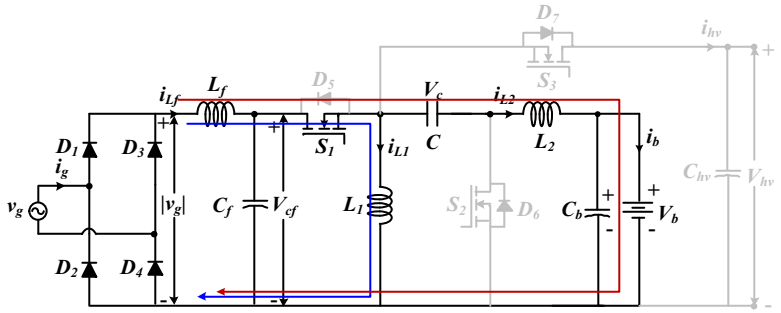

(a)

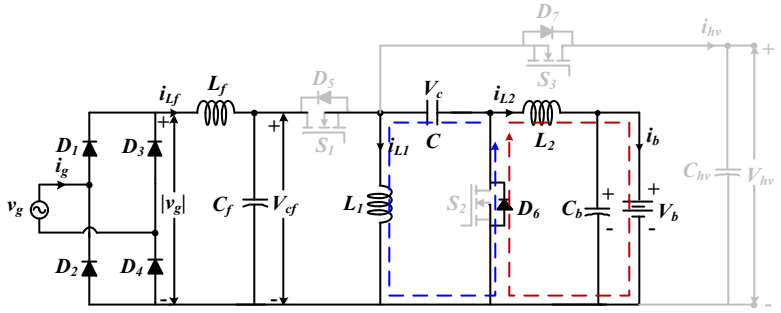

(b)

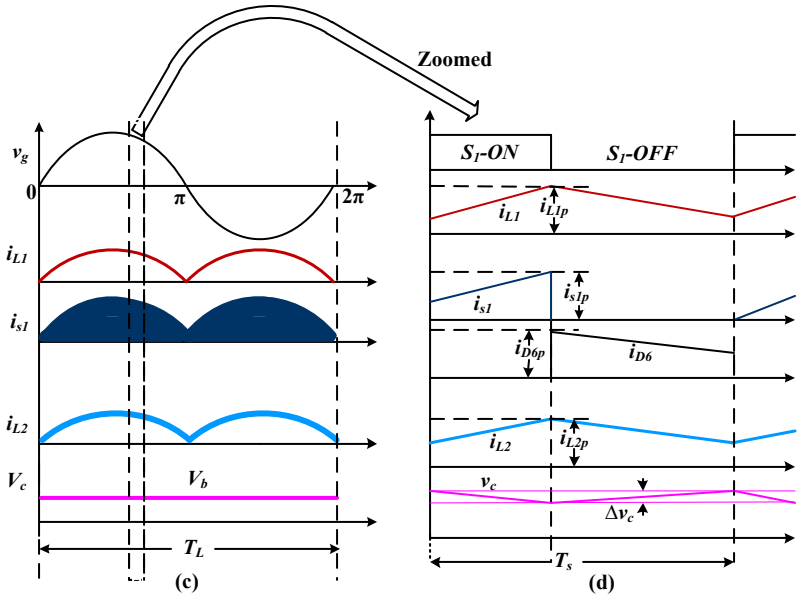

Fig. 2.3. Operation of the converter during plug-in charging mode, (a) when switch S_1 is ON, (b) switch S_1 is OFF, (c) switching waveforms during one line cycle, (d) one switching cycle

When switch S_1 is turned ON, inductor L_1 stores energy through the path $|v_g|$-L_f-S_1-L_1-$|v_g|$ and inductor L_2 stores energy through the path $|v_g|$-L_f-S_1-*C*-L_2-V_b-$|v_g|$, as shown Fig. 2.3(a). When switch S_1 is turned OFF, inductor L_1 discharges by supplying its stored energy to the capacitor *C*, and voltage across capacitor gradually increases, which is shown in Fig. 2.3(d), and the capacitor gets charged up to the battery voltage V_b. While inductor L_2 supplies energy to the output stage (capacitor and battery) shown in Fig. 2.3(b) and current through L_2 decreases linearly, as shown in Fig. 2.3(d). The capacitor C_{hv} gets charged up to $V_{g,max}$ through the body diode of S_3 (D_7) in short duration then after it retains this value forever in this mode.

If the duty ratio of the switch S_1 is d_1, then volt-second balance of inductor L_1 or L_2 for one switching period T_s can be given as

$$V_{g,max}|sin(\omega t)| * d_1(t) = V_b * (1 - d_1(t)) * T_s \tag{2.1}$$

From (2.1), the voltage conversion ratio M_1 as

$$M_1 = \frac{V_b}{V_{g,max}\,|\sin \omega t|} = \frac{d_1(t)}{1 - d_1(t)} \tag{2.2}$$

2.3.2 Propulsion mode

When this mode begins, the battery started supplying power to the dc-link of the inverter and vehicle comes in running phase.

In this mode, switches S_1 and S_3 are kept in OFF state using mode selector logic, and switch S_2 is gated through PWM signal. When switch S_2 is turned ON, inductor L_2 stores energy through the path V_b-L_2-S_2-V_b, and capacitor *C* discharges through inductor L_1, as shown in Fig. 2.4(a) and inductor current through L_1 is linearly increasing, which is shown in Fig. 2.5(a). When S_2 is turned OFF, inductor L_2 transfers its stored energy in the capacitor *C* and dc-link capacitor C_{hv} through the path V_b-L_2-*C*-D_7-V_{hv}-V_b and capacitor C is charged to the battery voltage. The inductor L_1 transfers its stored energy to the dc-link through the path L_1-D_7-V_{hv}-L_1, as shown in Fig. 2.4(b), and current through L_1 gradually decreases, which is shown in Fig. 2.5(a). If the duty ratio of the the switch S_2 is d_2, applying volt-second balance either in inductor L_1 or L_2 for one switching period then one can obtain:

$$V_b * d_2 * T_s = V_{hv} * (1 - d_2) * T_s \tag{2.3}$$

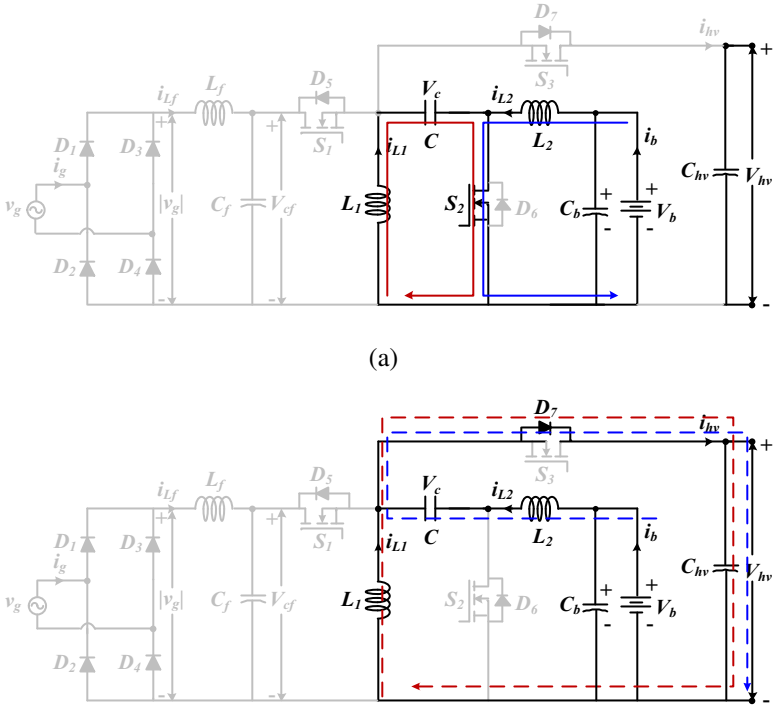

Fig. 2.4. Operation during Propulsion mode, (a) switch S_2 is ON, (b) switch S_2 is OFF

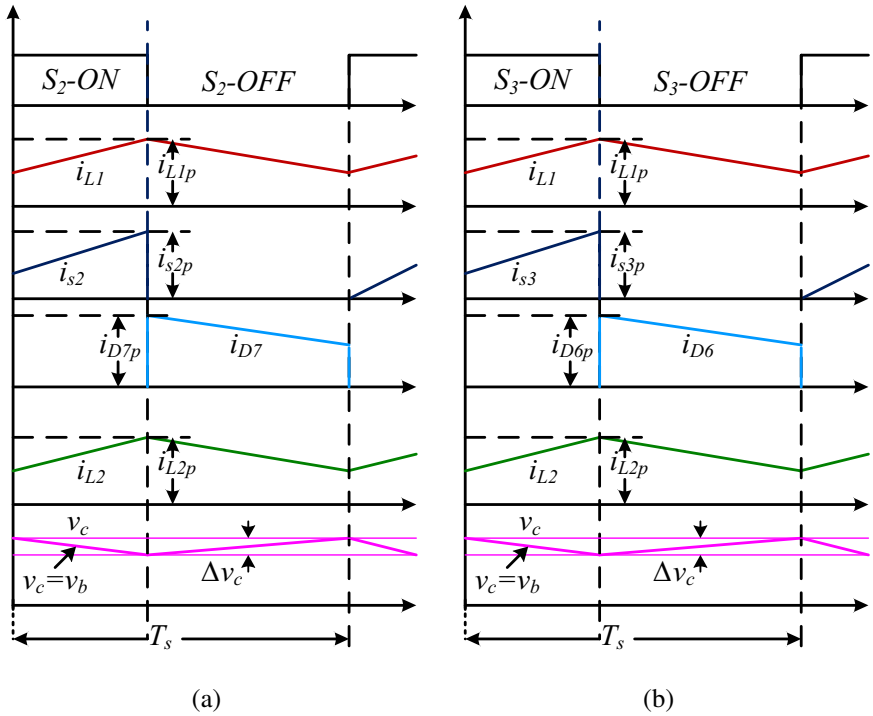

Fig. 2.5. Switching waveforms during (a) propulsion mode, (b) regenerative braking mode

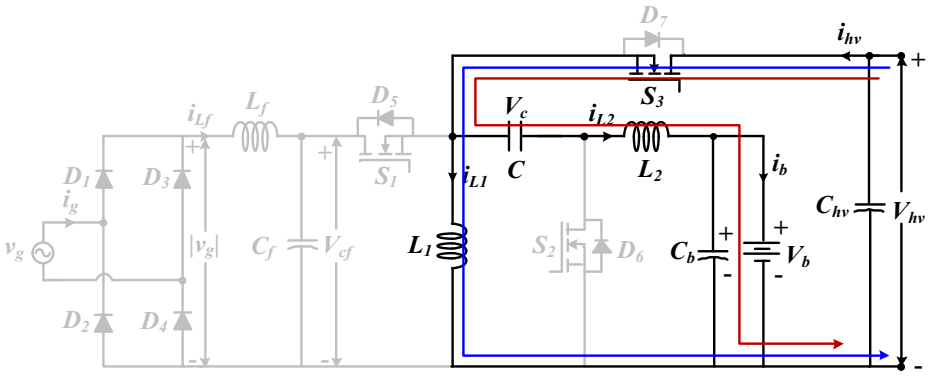

(a)

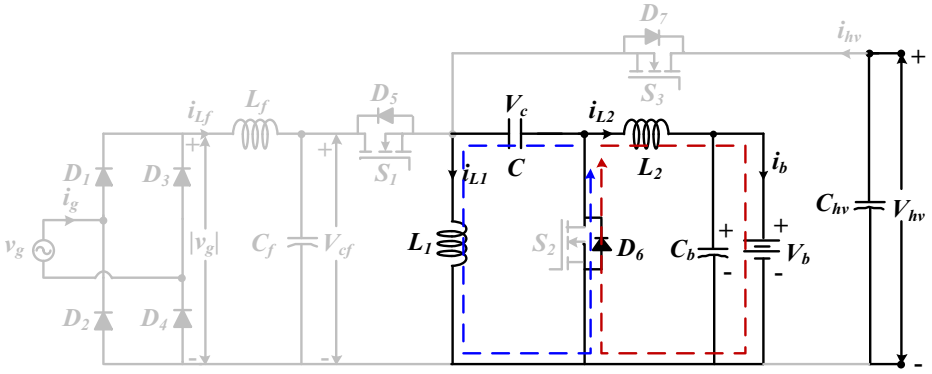

(b)

Fig. 2.6. Operation of regenerative braking mode, (a) switch S_3 is ON, (b) switch S_3 is OFF

The voltage conversion ratio M_2 from (2.3) can be expressed as

$$M_2 = \frac{V_{hv}}{V_b} = \frac{d_2}{1 - d_2} \tag{2.4}$$

2.3.3 Regenerative braking mode

During regenerative braking mode switches S_1, S_2 are OFF and switch S_1 is in PWM. When switch S_3 is turned ON, inductor L_1 stores energy through the path V_{hv} S_3-L_1-V_{hv} and inductor L_2 stores energy through the path V_{hv}-S_3-C-L_2-V_b-V_{hv}, as shown Fig. 2.6(a). When S_3 is turned OFF L_1 transfers its stored energy to the capacitor (C) through the path C - L_1-D_6 shown in Fig. 2.6(b) and capacitor voltage V_c gradually increases, which is shown in Fig. 2.5(d). While, L_2 transfers its stored energy to capacitor C_b / battery and thus charging the battery in the process (Fig. 2.6(b)). If the duty ratio of the switch S_3 is d_3, applying

Table 2.1. Peak voltage and current ratings of switches in all modes

Mode	S_1		S_2		S_3	
	Voltage	**Current**	**Voltage**	**Current**	**Voltage**	**Current**
Plug-in charging	$[v_g(\omega t)_{\omega t=\pi/2} + V_b]$	$[i_g(\omega t)_{\omega t=\pi/2} + I_b]$	$[v_g(\omega t)_{\omega t=\pi/2} + V_b]$	$[i_g(\omega t)_{\omega t=\pi/2} + I_b]$	$v_g(\omega t)_{\omega t=\pi/2} + V_C$	NC
Propulsion	V_{hv}+ V_b	NC	V_{hv}+ V_b	I_b + I_{hv}	V_{hv}+ V_b	I_b + I_{hv}
Regenerative braking	V_{hv}+ V_b	NC	V_{hv}+ V_b	I_b + I_{hv}	V_{hv}+ V_b	I_b + I_{hv}

NC=Not conducting

volt-second balance in inductor L_1 or L_2, and given:

$$V_{hv} * d_3 * T_s = V_b * (1 - d_3) * T_s \tag{2.5}$$

The voltage conversion ratio M_3 from (2.5) can be expressed as

$$M_3 = \frac{V_b}{V_{hv}} = \frac{d_3}{1 - d_3} \tag{2.6}$$

2.4 Components Selection

2.4.1 Selection of semiconductor devices

Usually, power rating and voltage stress on switches in each mode of PEVs are not same. Therefore, voltage/current rating of a particular switch is selected based on peak voltage/current developed either in switch or its body diode. It is assumed that voltage stress on body diode is the same as the switch voltage stress. Table 2.1 shows peak voltage/current stresses in switches for all modes. From Table 2.1 switch rating is selected as follows:
peak voltage rating of S_1 and S_2 = max($v_g(\omega t)_{\omega t=\pi/2}$+$V_b$, V_b+V_{hv}) and peak current rating of S_1 = $i_g(\omega t)_{\omega t=\pi/2}$ +I_b. The peak current rating of S_2= max ($i_g(\omega t)_{\omega t=\pi/2}$ +I_b, I_b+I_{hv}). While voltage and current rating of S_3 is chosen same as S_2 because body diode of S_3 conducts in propulsion mode and power rating of propulsion mode in PEVs usually highest among modes [98].

2.4.2 Selection of inductors L_1 and L_2

In the PEVs, usually, the power level is high. At high power level CCM operation of converter is preferred over DCM. During time interval [0, $d_1(t)T_s$], the inductor current ripple of L_1

can be written as

$$\triangle i_{L1} = \frac{|v_g|}{L_1} d_1(t) T_s \tag{2.7}$$

Boundary condition for inductor current ripple happens when current ripple is the twice of the average input current. Thus,

$$\triangle i_{L1} = \frac{|v_g|}{L_1} d_1(t) T_s = 2 i_g \tag{2.8}$$

Assuming unity power factor, the ratio of input voltage and input current can be expressed by an effective resistor, R_e

$$R_e = \frac{v_g}{i_g} = \frac{V_g^2}{p_g} \tag{2.9}$$

Thus, the CCM condition for inductor current i_{L1} can be expressed as

$$L_1 > max\left(\frac{R_e d_1(t)}{2 f_s}\right) > \frac{V_g^2}{p_g} \frac{1}{2 f_s} \frac{V_b}{|V_{g,max}| + V_b} \tag{2.10}$$

From (2.10), larger are the minimum input power Pg_{min} and switching frequency f_s, the easier it is for the converter to enter into CCM. Similarly, the boundary condition for L_2 can be derived. The CCM condition for inductor current i_{L2} can be expressed as

$$L_2 > \left(\frac{R_L d_1'(t) T_s}{2}\right) > \frac{R_{L,max}}{2} \frac{|V_{g,max}|}{|V_{g,max}| + V_b} \frac{1}{2 f_s} \tag{2.11}$$

According to (2.11), higher are the switching frequency and smaller load resistance, $R_{L,max}$, the easier it is for the converter to enter into CCM. Using specification given in Table 2.6, the value of both inductors is selected as 2 mH in the simulation as well as in hardware.

2.4.3 Selection of capacitor *C*

The coupling capacitor *C* is an important element in the proposed converter since its value greatly influence the quality of input current. Therefore, this capacitor will be designed under the following constraints:

The resonant frequency of L_1, L_2 and *C* during CCM operation must be greater than line frequency f_L to avoid input current oscillations at every half line cycle and lower than switching frequency f_s to assure constant voltage in a switching period, i.e.,

$$f_L < f_r < f_s \tag{2.12}$$

where

$$f_r = \frac{1}{2\pi\sqrt{(L_1 + L_2)C}} \tag{2.13}$$

In this work, switching frequency, f_s is set as 20 kHz, and f_r is set as 1 kHz. The capacitor *C* is selected as 10 μF both in simulation and hardware. The voltage rating of this capacitor is selected based on battery voltage range because both in ZETA and SEPIC modes, the voltage across coupling capacitor follows battery voltage.

2.4.4 Selection of L_f and C_f

The design of input filter is essential for maintaining low harmonic distortion in grid current [91], [102]. The maximum value of filter capacitance is expressed as

$$C_{f_{max}} = \frac{I_{g,max} \tan(\theta)}{2\pi f_L V_{g,max}} \tag{2.14}$$

where $V_{g,max}$ and $I_{g,max}$ are peak input voltage, and θ is considered below 5° for maintaining high input power factor. The capacitance $C_{f_{max}}$ is calculated as 1.14 μF and selected value in the simulation and hardware is 1 μF.

The filter inductor to maintain low ripple is calculated as

$$L_f = \frac{1}{4\pi^2 f_c^2 C_f} \tag{2.15}$$

where f_c is cut off frequency, which is selected such that it should more than the grid frequency f_L = 50 Hz and less than switching frequency f_s = 20 kHz . Therefore, it is chosen as 4 *kHz*. The L_f from (2.15) is calculated as 1.58 mH, and the selected value in the simulation and hardware is 1.5 mH.

2.4.5 Selection of capacitor C_b

With regards to the parallel capacitor across the battery terminal, the switching frequency voltage ripple is negligible as this capacitor is typically very large. Twice of the line frequency voltage ripple is more critical since it directly affects the charging voltage. The low-frequency voltage ripple on the battery capacitor is given as [103]

$$C_{b,min} > \frac{P_b}{4 f_L \Delta v_b V_b} \tag{2.16}$$

where f_L is the grid frequency and Δv_b is the capacitor ripple. To reduce the low frequency voltage ripple, a large value of capacitor is preferred. However, this will make the electrolytic

capacitor bulky. Therefore, the trade off between output voltage ripple and capacitor size must be taken into consideration for designing the converter. From above expression, the dc-link capacitance is selected as 2.2 mF for $\Delta v_b < 5$ % of the battery voltage.

2.5 Current Stress and Loss Analyses

2.5.1 Current stress analysis

Further, to investigate the loss analysis of the converter in each mode, we need current stress model of the proposed converter; therefore, in the following paragraphs, current stresses of switches and diodes are developed in plug-in charging mode and similar analysis can be expected for other modes:

Root mean square (RMS) current through switch S_1, first averaged over one switching period, then the result is averaged over ac line period and square root is taken of result.

$$I_{s1,RMS} = \sqrt{\frac{1}{T_L}\int_0^{T_L} \langle i_{s1}^2 \rangle_{T_s} dt} \tag{2.17}$$

where

$$\left\langle i_{s1}^2 \right\rangle = \frac{1}{T_s}\int_t^{t+T_s} i_{s1}^2(t)dt = d_1(t)[i_{L1}(t) + i_{L2}(t)]^2 \tag{2.18}$$

where $d_1(t) = \frac{1}{1+\alpha\sin(\omega t)}$ from (2.2) and $\alpha = \frac{V_{g\max}}{V_b}$. The inductors current can be written as: $i_{L1}(t) = I_{g,max}\sin(\omega t)$ and $i_{L2}(t) = \alpha I_{g,max}\sin^2(\omega t)$. By substituting $d_1(t)$, $i_{L1}(t)$ and $i_{L2}(t)$ in (2.18), which is simplified as

$$I_{s1,RMS} = I_{g,max}\sqrt{\frac{1}{\pi}\int_0^{\pi} \sin^2(\omega t)[1 + \alpha\sin(\omega t)]d(\omega t)} \tag{2.19}$$

$$I_{s1,RMS} = I_{g,RMS}\sqrt{1 + \alpha\frac{8}{3\pi}} \tag{2.20}$$

A similar analysis for RMS diode current $i_{D5,RMS}$ can be expressed as

$$i_{D5,RMS} = I_b\sqrt{\frac{3}{2} + \frac{16}{3\pi}\alpha} \tag{2.21}$$

Average current through the diode D_6 can be expressed as

$$I_{D6,avg} = \frac{1}{\pi}\int_0^{\pi} (1 - d_1(t))[i_{L1} + i_{L2}]d(\omega t) = \frac{I_{g,max}}{\pi}\int_0^{\pi} [\alpha\sin(\omega t)]d(\omega t) \tag{2.22}$$

which yields

$$I_{D6\_avg} = \frac{I_{g,RMS} 2\sqrt{2}}{\pi}\alpha \tag{2.23}$$

The average current through S_1 by similar analysis (diode) gives the following expression

$$I_{s1,avg} = I_{g,RMS}\frac{2\sqrt{2}}{\pi} \tag{2.24}$$

The instantaneous inductor current through L_f and L_1 can be written as

$$i_{Lf} = i_{L1} = I_{g,\max}\sin(\omega t) \tag{2.25}$$

The RMS current through L_f and L_1 can be computed as

$$I_{Lf,RMS} = I_{L1,RMS} = \sqrt{\frac{1}{\pi}\int_0^{\pi}\left[I_{g,\max}\sin(\omega t)\right]^2 d(\omega t)} \tag{2.26}$$

which yields

$$I_{Lf,RMS} = I_{L1,RMS} = I_{g,RMS} \tag{2.27}$$

where $I_{g,RMS}$ = $I_{g,max}/\sqrt{2}$.

The instantaneous current through L_2 is given as

$$i_{L2} = \alpha I_{g,\max}\sin^2(\omega t) \tag{2.28}$$

$$I_{L2,RMS} = \sqrt{\frac{1}{\pi}\int_0^{\pi}\left[\alpha I_{g,\max}\sin^2(\omega t)\right]^2 d(\omega t)} \tag{2.29}$$

which yields

$$I_{L2,RMS} = I_{g,RMS}\alpha\sqrt{\frac{3}{2}} \tag{2.30}$$

The average current through L_f, L_1 and L_2 is computed as

$$I_{Lf,avg} = I_{L1,avg} = \frac{1}{\pi}\left(\int_0^{\pi} I_{g,\max}\sin(\omega t)\right) = I_{g,RMS}\frac{2\sqrt{2}}{\pi} \tag{2.31}$$

$$I_{L2,avg} = \frac{1}{\pi}\left(\int_0^{\pi}\alpha I_{g,\max}\sin^2(\omega t)\right) = \frac{I_{g,RMS}}{2}\alpha \tag{2.32}$$

Table 2.2. Approximate RMS and average current stresses on switches/diodes in each mode.

Device	Plug-in charging		Propulsion		Regenerative braking	
	RMS	**Average**	**RMS**	**Average**	**RMS**	**Average**
S_1	$I_{g,RMS}\sqrt{1+\alpha\frac{8}{3\pi}}$	$I_{g,RMS}\frac{2\sqrt{2}}{\pi}$	NC			
S_2	NC		$I_{hv}\sqrt{\frac{(V_{hv}+V_b)V_{hv}}{V_b^2}}$	$d_2(I_b+I_{hv})$	NC	
S_3			NC		$I_b\sqrt{\frac{(V_{hv}+V_b)V_b}{V_{hv}^2}}$	$d_3(I_b+I_{hv})$
D_5			NC			
D_6	$I_b\sqrt{\frac{3}{2}+\frac{16}{3\pi}\alpha}$	$\frac{I_{g,RMS}2\sqrt{2}}{\pi}\alpha$	NC		$I_{hv}\sqrt{\frac{(V_{hv}+V_b)V_{hv}}{V_b^2}}$	$(I_b+I_{hv})(1-d_3)$
D_7	NC		$I_b\sqrt{\frac{(V_{hv}+V_b)V_b}{V_{hv}^2}}$	$(I_b+I_{hv})(1-d_2)$	NC	
L_f	$I_{g,RMS}$	$I_{g,RMS}\frac{2\sqrt{2}}{\pi}$	NC			
L_1	$I_{g,RMS}$	$I_{g,RMS}\frac{2\sqrt{2}}{\pi}$	$\frac{2}{\sqrt{3}}I_{hv}$	I_{hv}	$\frac{2}{\sqrt{3}}I_{hv}$	I_{hv}
L_2	$I_{g,RMS}\alpha\sqrt{\frac{3}{2}}$	$\frac{I_{g,RMS}}{2}\alpha$	$\frac{2}{\sqrt{3}}I_b$	I_b	$\frac{2}{\sqrt{3}}I_b$	I_b

where NC = Not conducting.

Similarly, the determination of RMS and average current of switches/diodes and passive components in dc/dc stage (propulsion and regenerative braking modes) can be found by integration of currents over one switching period, which are given as

$$I_{x,RMS}^2 = \sqrt{\frac{1}{T_s}\int_t^{t+T_s} i_x^2(t)dt} \tag{2.33}$$

$$I_{x,avg} = \frac{1}{T_s}\int_t^{t+T_s} i_x(t)dt \tag{2.34}$$

where $i_x(t)$ is the instantaneous current through a component.

The RMS and average currents through switches/diodes and passive components in each mode are tabulated in Table 2.2.

2.5.2 Loss analysis

In this Section, an analytical loss analysis of the proposed converter is investigated in each mode. The conduction and switching losses for two semiconductor switches, i.e., 1200V/100 A and 1700 V/72 A in ac/dc stage (plug-in charging mode) and dc/dc stage (propulsion and regenerative braking modes) are analytically calculated using manufacturers data-sheet and current (RMS and average) expressions (Table 2.2). Moreover, the passive components which

are in the main current path also included in this analysis to accurate calculation of efficiency in each mode. The conduction loss for a MOSFET switch can be calculated as follows

$$P_{S,cond} = I_{s,rms}^2 * R_{(on)} \tag{2.35}$$

On other hand, the conduction loss for an IGBT switch will be calculated as:

$$P_{S,cond} = \langle i_s \rangle_{Ts} * V_{CE_{sat}} \tag{2.36}$$

Switching energy losses occur due to the simultaneous presence of significant drain-source voltage and drain current during each transient from turn OFF-state to turn ON-state, and from turn ON-state to turn OFF-state. Then total switching power losses of a switch can be approximately calculated as

$$P_{sw} = \frac{1}{2} \left(V_{s,\max} * I_{s,\max} \right) * (t_r + t_f) * f_s \tag{2.37}$$

where $V_{s,max}$ and $I_{s,max}$ are peak values of voltage and current and t_r and t_f are the rising and falling times of a switch, respectively. Power loss of diode is the sum of diode conduction loss (product of average current (I_F) and knee voltage (V_F)) and reverse recovery loss, which is modeled as

$$P_D = V_F * I_F + P_{Qrr} \tag{2.38}$$

where P_{Qrr} is the reverse recovery loss of a diode. The P_{Qrr} can be neglected for fast recovery diode and lower switching frequency.

The total semiconductor losses P_S is modeled as

$$P_S = P_{S,cond} + P_{sw} + P_D \tag{2.39}$$

The passive components which are in the main current path are L_1, L_2, L_f and capacitor C, then inductors copper losses are modeled as

$$P_L = I_{L_f,rms}^2 * r_f + I_{L_1,rms}^2 * r_1 + I_{L_2,rms}^2 * r_2 \tag{2.40}$$

where r_f, r_1 and r_2 are series resistances of inductors L_f, L_1 and L_2, respectively.
The ohmic loss in equivalent series resistance r_c of the capacitor C is expressed as

$$P_c = I_{c,rms}^2 * r_c \tag{2.41}$$

Table 2.3. Semiconductors and passive components losses of the proposed converter in ac/dc and dc stages with V_b = 300 V and V_{hv} = 400 V

P_{ch} [kW]	P_{prop} [kW]	P_{reg} [kW]	V_{grid} [V]	Switch rating	Total semiconductors losses, P_S [W]			Total passive components losses, P_P [W]		
					Plug-in charging (ac/dc stage)	Propulsion (dc/dc stage)	Regenerative braking (dc/dc stage)	Plug-in charging (ac/dc stage)	Propulsion (dc/dc stage)	Regenerative braking (dc/dc stage)
1.8	5	0.5	120	1200 V/100 A [V_F = 2.55 V, t_r = 65 ns, t_f = 80 ns]	113	100.94	23.86	44.88	47.254	2.2
3.2	5	0.5	240		116.93	100.94	23.86	48.69	47.254	2.2
1.8	10	1	120	1200 V/100 A [V_F = 2.55 V, t_r = 65 ns, t_f = 80 ns]	113	207.39	36.8	40.13	189.079	8.2
6.6	10	1	240		253.12	207.39	36.8	185.445	189.079	8.2
1.8	5	0.5	120	1700 V/72 A [V_F = 3.6 V, t_r = 20 ns, t_f = 18 ns]	87.44	78.95	16.2	44.88	47.254	2.2
3.2	5	0.5	240		94.18	78.95	16.2	48.69	47.254	2.2
1.8	10	1	120	1700 V/72 A [V_F = 3.6 V, t_r = 20 ns, t_f = 18 ns]	87.44	201.66	25.2	44.88	189.079	8.2
6.6	10	1	240		225.46	201.66	25.2	185.445	189.079	8.2

Then total passive components losses P_P is given as

$$P_P = P_{Lf} + P_{L1} + P_{L2} + P_c \tag{2.42}$$

where P_{Lf}, P_{L1} and P_{L2} are the copper loss in L_f, L_1 and L_2, respectively. To use (2.42) for loss calculation of passive components in dc/dc stage, the P_{Lf} will be discarded.

Using loss equations (2.35)-(2.42), Table 2.3 shows total semiconductors losses P_S and total passive components losses P_P in ac/dc stage and dc/dc stage where P_{ch}, P_{prop} and P_{reg} denote power rating of plug-in charging, propulsion and regenerative braking modes, respectively. It is noticed that from Table 2.3 in ac/dc stage, the P_S with grid voltage of 240 V is between 2.9-4% of the rated power for mentioned switching devices. With 120 V grid voltage, P_S in ac/dc stage varies between 4.8-6.2% of the rated power for both switching devices. With 120 V grid voltage, percentage of P_S is high compared to 240 V grid voltage. It is because with 120 V, grid current is higher compared to 240 V, leading to higher losses in the components. The P_S in dc/dc stage is 2.5-4.7% of the rated power.

The P_P in ac/dc stage with 120 V grid voltage is 2.5% of the rated power and with 240 V grid voltage is 1.5-2.78% of the rated power. In dc/dc stage, the P_P is between 0.3-2% of the rated power. Moreover, the total losses (semiconductors and passive components) in ac/dc and dc/dc stages are between 6.2-8.2% and 2-5% of the rated power for both devices, respectively. Percentage of total losses in ac/dc stage is higher compared to dc/dc stage, it is because in ac/dc stage additional losses of rectifier diodes and grid side filter components. A loss breakdown of the converter at full load for 1200 V/100 A switch is given in Table 2.4.

Table 2.4. A loss breakdown of the system in ac/dc and dc/dc stages with 400 V dc-link and 300 V battery

Mode	$P_{S,cond}$ [W]	P_{sw} [W]	P_D [W]	P_{Lf} [W]	P_{L1} [W]	P_{L2} [W]	P_c [W]
Plug-in charging [240 V, 6.6 kW]	65	56.62	107.32	45.375	73.18	65.81	1.08
Propulsion [10 kW]	79.4	58.99	69	– –	68.75	115.95	4.379
Regenerative braking [1 kW]	12	10.2	14.6	– –	3.4	4.2	0.6

Table 2.5. Comparative study of the proposed integrated converter with single-stage chargers

Charger topologies	Mode of operation			Number of components			
	Plug-in charging	Propulsion	Regenerative braking	Switch	Diode	Inductor	Capacitor
Boost PFC converter	Boost	Buck/boost	Buck/boost	5	5	2	2
Inverting Buck/boost PFC Converter	Buck/boost	Buck/boost	Buck/boost	5	5	2	2
SEPIC PFC converter	Buck/boost	Buck/boost	Buck/boost	5	5	3	3
CuK PFC converter	Buck/boost	Buck/boost	Buck/boost	5	5	3	3
Integrated converter [95]	Buck/boost	Buck/boost	Buck/boost	6	9	1	2
Integrated converter [98]	Boost	Buck/boost	Buck /boost	4	4	1	2
Integrated converter [99]	Boost	Boost	Buck	5	1	1	2
Proposed integrated converter	Buck/boost	Buck/boost	Buck/boost	3	4	2	3

2.6 Comparative Study

2.6.1 Comparison with single-stage chargers

The conventional single-stage battery charger topologies, namely the boost PFC converter, inverting buck/boost PFC converter, SEPIC PFC converter, and Cuk PFC converter are shown in Fig. 2.7. In order to have a fair comparison of the proposed converter with conventional single-stage converters, the dc/dc converter connected between the battery and dc-link in Fig. 2.7, is assumed to be a four-quadrant bidirectional converter. The boost PFC converter can charge the battery when battery voltage is more than the peak grid voltage ($V_b > V_{g,max}$). While other conventional converters can charge the battery whether battery voltage is higher or lower than the peak grid voltage. But inverting buck/boost and Cuk converter

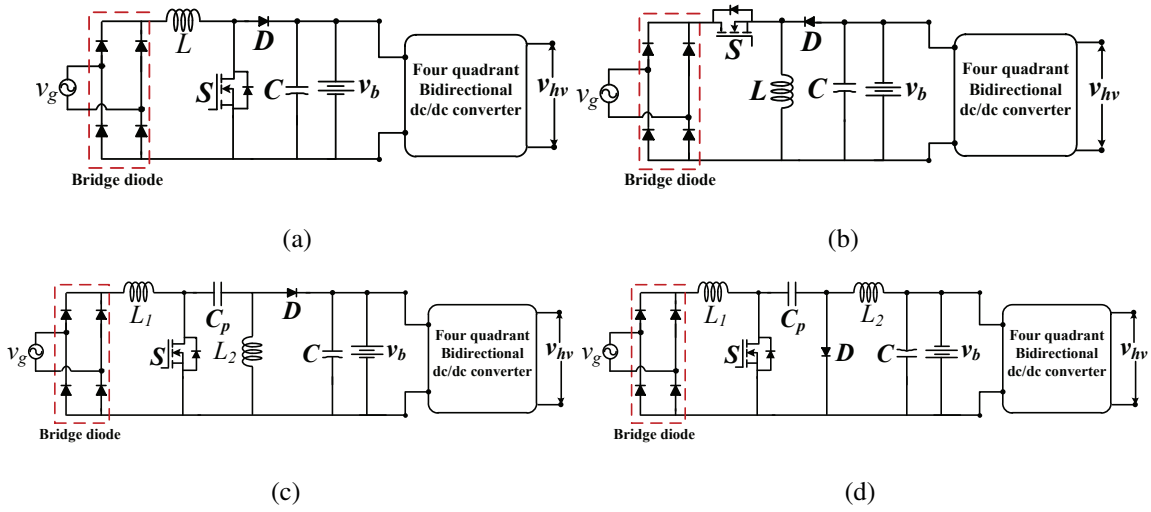

Fig. 2.7. Conventional single-stage EV battery chargers, (a) PFC boost converter, (b) inverting buck/boost PFC converter, (c) SEPIC PFC converter, (d) Cuk PFC converter

both have negative output voltage with respect to the input. The same polarity between the input and the output has an advantage of solving electromagnetic interference (EMI) /electromagnetic compatibility (EMC) problems and in filters design become easy, because the internal ground of a vehicle, the ground of the OBC and the cathode of the battery can have the same potential [30]. However, in Cuk and SEPIC PFC based converter topologies have an additional inductor compared to the proposed integrated converter. In addition to these conventional chargers, other existing integrated chargers are also included in this comparative analysis. It is seen from Table 2.5, the proposed converter has least components compared to those converters which have buck/boost operation in each mode. However, the integrated converter [95] has lower voltage/current stresses in the devices (either input or output voltage/current) as well as buck/boost operations in each mode, but the efficiency of this converter is lower because of three or four semiconductor devices (depending on mode) in the current path. The integrated converter [98] has low stresses as converter [95], but the major limitation of this converter is only have a boost charging capability thereby selection of the wide range of battery voltage is not possible. The efficiency plots of the proposed converter and integrated converters of [95, 98] using 1200 V/100 A device in each mode are shown in Fig. 2.8. The integrated converter [99] has bridge less nature in plug-in charging mode, low volt-

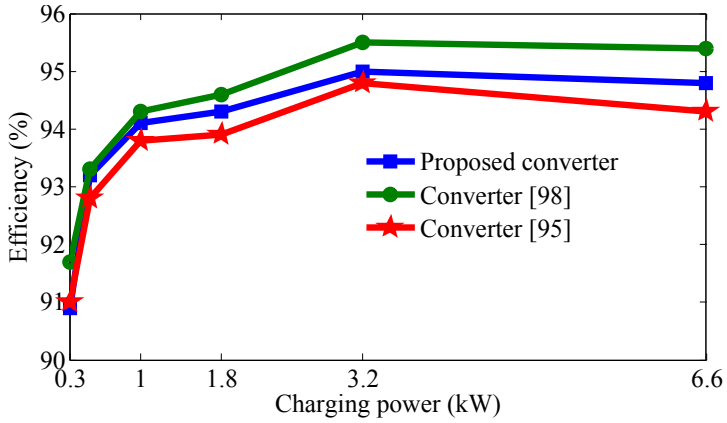

(a)

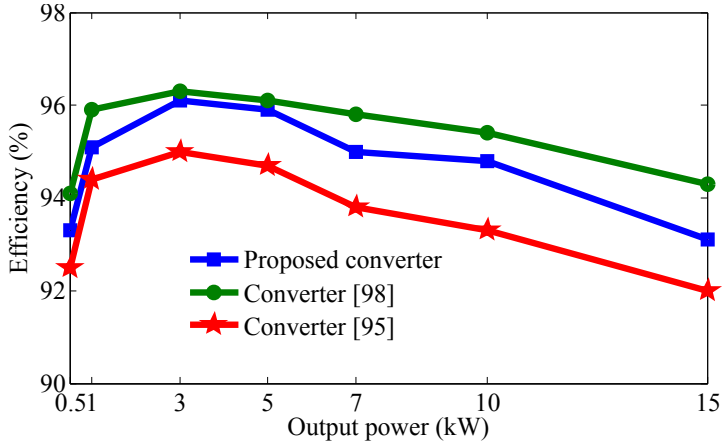

(b)

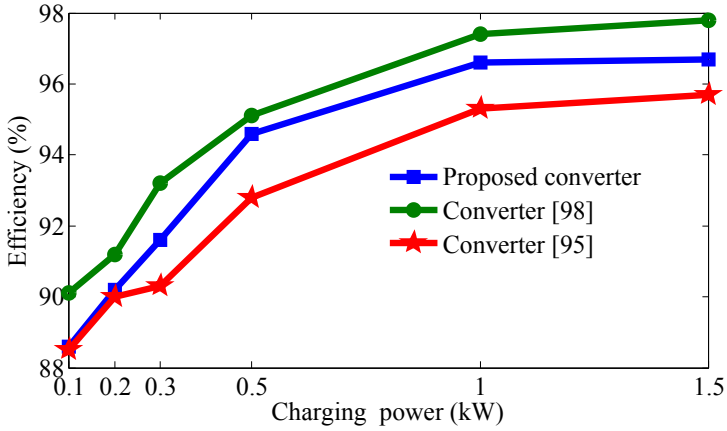

(c)

Fig. 2.8. Efficiency comparison, (a) plug-in charging mode, (b) propulsion mode, (c) regenerative braking mode

age and current stresses in propulsion and regenerative modes and one or two device(s) are in the main current path; therefore, this converter will have higher efficiency than proposed converter in each mode. However, the major limitation of this converter is, none of the modes has buck/boost operation.

From Table 2.5, the proposed converter has two additional passive components (one inductor and one intermediate capacitor C) compared to other existing integrated converters. The voltage across capacitor C follows battery voltage both in SEPIC and ZETA modes, the peak voltage across the capacitor $C = V_b + \Delta V_C$, where ΔV_C is voltage ripple of V_C then voltage rating of this capacitor is selected according to slightly higher than the battery voltage. Usually, the capacitance value of C is between 0.5-10 μF for 20 kHz switching frequency range [91, 104]; therefore, the size of this capacitor is smaller compared to the battery terminal capacitor C_b (designed based on twice of the grid frequency). Nevertheless, the additional increase of two passive components as well as higher losses in the proposed converter compared to existing converters [98, 99] result in increase in volume of the proposed converter. But converter [95] has a number of semiconductor devices (switches are twice of the proposed converter) and switches with driver circuit occupy a considerable floor area (Fig. 2.20) as well as higher losses; therefore, the overall size of the proposed converter may be lower or comparable to this converter. Moreover, compared to conventional single-stage converters that have buck/boost operations in each mode, the proposed converter has lower volume due to fewer number of passive and semiconductor components.

2.6.2 Components lifetime and reliability analysis

The lifetime of semiconductor switches are typically much higher than capacitor and battery. The capacitor connected to the high voltage dc-link is not utilized during plug-in charging, and the capacitor connected to the battery terminals is also cycled similar to the conventional OBCs (Fig. 2.7); therefore, the proposed converter will not pose any additional threat on the capacitor failure.

Switch S_2 or its body diode conducts in each mode as discussed in operation modes; therefore, extra cycling of S_2 may reduce its lifetime to some extent. In addition to this, failure of this switch affects other two modes, as a result, reliability of the proposed converter

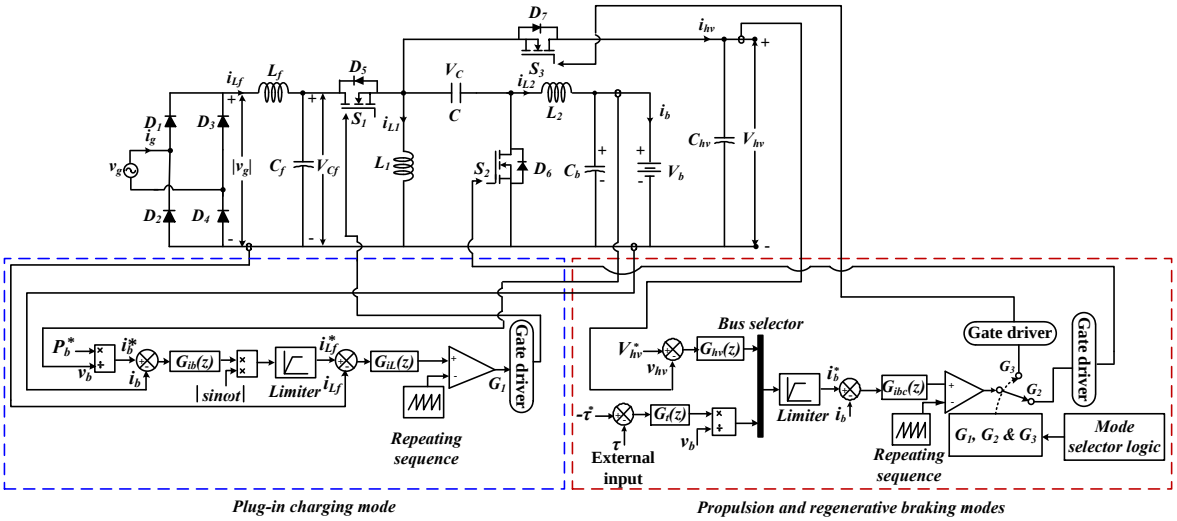

Fig. 2.9. Control algorithm of the proposed converter during different modes

is slightly lower than conventional OBCs. While switch S_1 conducts only in charging mode and charging power (usually lower than propulsion mode) will not pose any high thermal or electric stresses compared to dc/dc conversion stage; therefore, its chance of failure is lower than other two switches. Nevertheless, if switch S_1 fails it would not affect other modes of operation. Switch S_3 conducts in regenerative braking mode and its body diode in propulsion mode. Therefore, its failure chance is high compared to S_1 and low compared to S_2.

2.7 Control Strategy

The control structure during different modes of converter operation [98] is shown in Fig. 2.9. Each mode is implemented by mode selector logic, which requires external input such as; torque (τ), speed (ω), and charging power (P_g). Since this work is focused on power electronics converter parts of the electric vehicle; therefore, the mode selection is done manually.

During battery charging from the grid, the reference charging power is divided by instantaneous battery voltage to create a reference battery current as input to the outer proportional-integral (PI) controller $G_{ib}(z)$. The output of the outer PI controller is a reference dc signal, which is multiplied by a unit rectified sinusoidal wave to generate the reference input to the inner current PI controller $G_{iL}(z)$. This current controller works on this reference current so as to get power factor correction on the grid side.

The outer PI controller $G_{ib}(z)$ is expressed as

$$G_{ib}(z) = K_p + \frac{K_i T_s}{z-1} \tag{2.43}$$

where K_p is the proportional gain to adjust the control bandwidth and K_i is the integral gain to achieve zero steady state error.

The inner PI controller is given by the following equation as

$$G_{iL}(z) = K_{pc} + \frac{K_{ic} T_s}{z-1} \tag{2.44}$$

where K_{pc} is the proportional gain and K_{ic} is the integral gain. These two coefficients are tuned such that the bandwidth of the controller is kept between one sixth to one tenth of the switching frequency. Further, due to presence of low frequency component (100 Hz) in battery current, the bandwidth of $G_{ib}(z)$ controller is kept below 100 Hz to avoid the distortion in the reference signal for inner current loop.

In propulsion and regenerative braking modes, average current mode controller is used. Depending upon operating modes appropriate switch is turned ON. In propulsion mode, the dc-link voltage is regulated through two loop controller. The outer PI controller $G_{hv}(z)$ regulates the dc-link voltage by generating reference battery current for the inner current controller $G_{ibc}(z)$. In regenerative braking modes, the reference quantity is usually torque. Therefore, torque is converted into reference charging power and this reference power is divided by instantaneous battery voltage, to generate reference battery current, which is input to the current controller $G_{ibc}(z)$ for battery current tracking, as shown in Fig. 2.9.

2.8 Results and Discussion

2.8.1 Simulation results

The simulation of the proposed converter has been carried out in MATLAB/Simulink environment using two sets of parameters shown in Table 2.6. The first set is for nominal voltage and power, whereas the second set is for reduced voltage and power to bring parity between simulated and experimental results.

SET-1: This simulation study is carried out with the parameters values corresponding to SET-1.

Table 2.6. Simulation parameters

Parameters	**Values (SET-1/SET-2)**
Grid voltage (V_g)	*220/70.7 V*
dc-link voltage (V_{hv})	*400/60 V*
Line frequency (f_L)	*50/50 Hz*
Battery nominal voltage (V_b)	*300/36 V*
Nominal charging power (P_b)	*1 kW/210 W*
L_1/L_2	*2/2 mH*
Switching frequency (f_s)	*20/20 kHz*
C_{hv}/ C/C_b	*550/ 10/ 2200 μF* (SET-1 and SET-2)

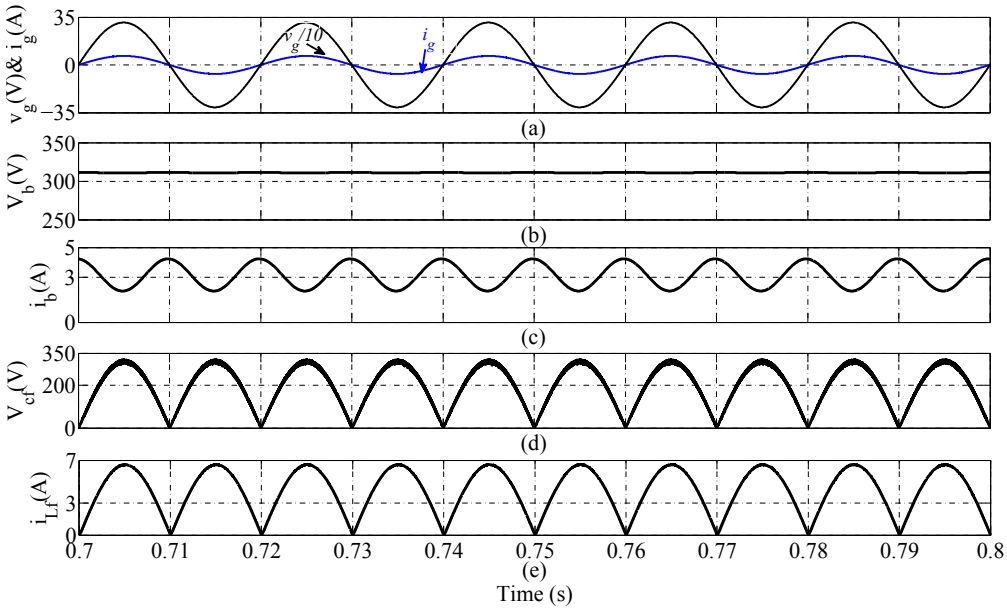

Fig. 2.10. Simulation waveforms during plug-in charging mode with 220 V_{RMS} of grid voltage, (a) grid voltage and current, (b) battery voltage, (c) battery current, (d) filter voltage (V_{cf}) (V), (e) filter inductor current (i_{Lf})

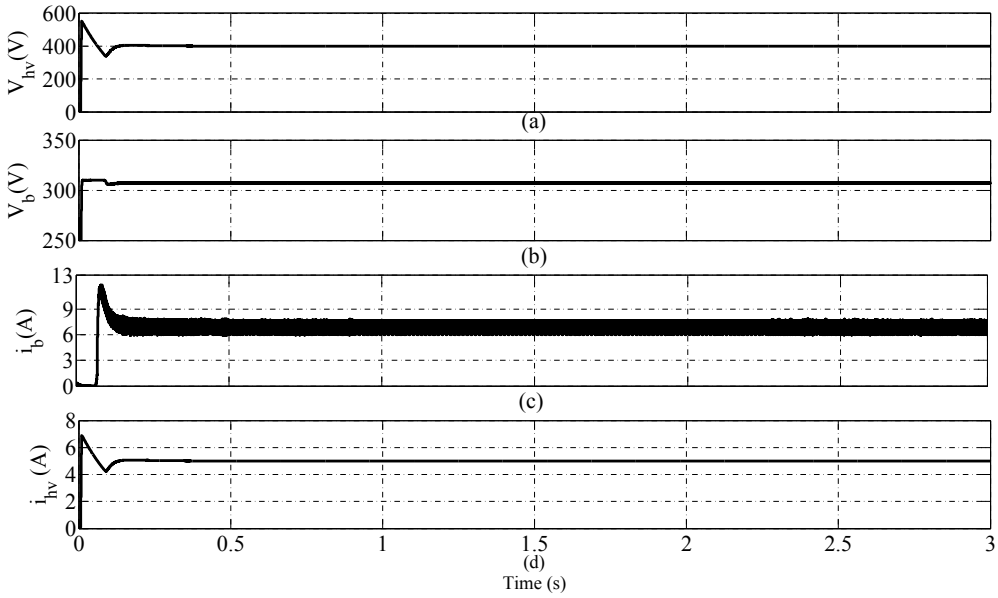

Fig. 2.11. Simulation waveforms of propulsion mode, (a) dc-link voltage, (b) battery voltage, (c) battery current, (d) dc-link current

In charging mode, the grid voltage is fixed at 220 V, charging power is 1 kW and the nominal battery voltage is 300 V with 20 % of SOC. Fig. 2.10 shows simulated waveforms of grid voltage (v_g), grid current (i_g), battery voltage (V_b), battery current (i_b) and grid side filter voltage and current (V_{cf} and i_{cf}). It is seen from Fig. 2.10 (a), the grid voltage and grid current are in the phase. The total harmonic distortion (THD)and power factor (PF) of the grid current computed using Fast Fourier Transform (FFT) tool of the MATLAB are 3.77% and 0.99, respectively. The battery voltage and current are also shown in Fig. 2.10 (b) and (c), respectively. From Fig. 2.10, it is seen that the battery current has a low frequency (100 Hz) oscillation, which is inherent in single-stage (single-phase) system. This oscillation of battery current depends on filter inductor connected in series with the battery. The value of inductance filter is chosen such that compromised between allowable low frequency battery ripple current and compactness of the charger. The grid side filter capacitor voltage and filter inductor current are also shown in Fig. 2.10(d) and (e), respectively.

The relevant waveforms of propulsion mode are shown in Fig. 2.11 with 400 V dc-link and 1 kW output load power. The dynamic performance of this mode is shown in Fig. 2.12 by step load variations. The load power is changed from 1 to 2 kW at t = 1.2 s and from 2 to

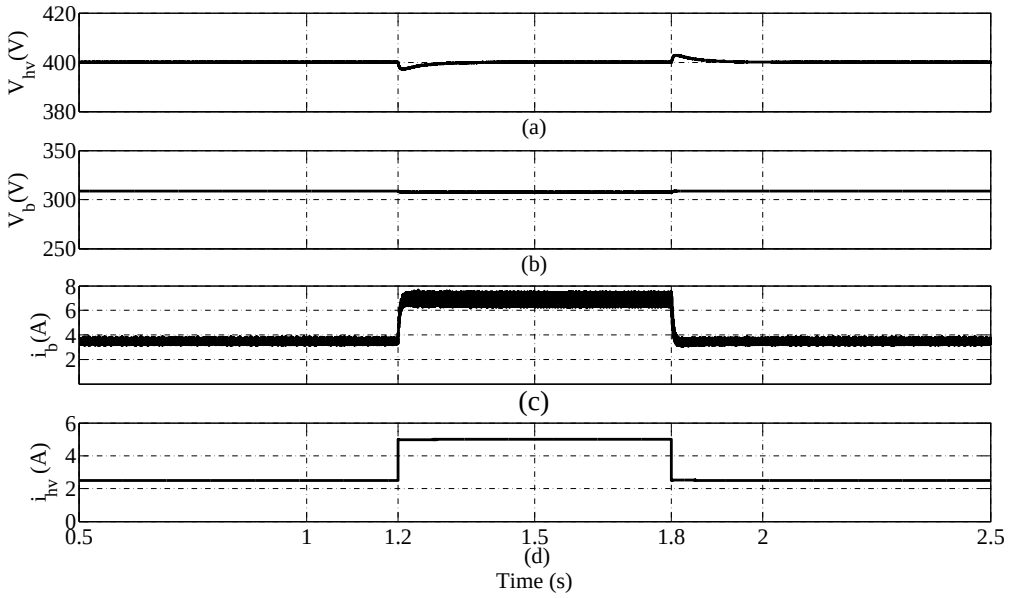

Fig. 2.12. Simulation waveforms of propulsion mode with step load variations, (a) dc-link voltage, (b) battery voltage, (c) battery current, (d) dc-link current

1 kW at t = 1.8 s. The control objective of this mode is to keep the dc-link voltage constant for satisfactory operation of the inverter-drive system. The dc-link voltage is well regulated at 400 V after the load changes, as shown in Fig. 2.12(a) which shows effectiveness of the controller performance. The battery voltage and current are shown in Fig. 2.12(b) and (c), respectively. The battery current is seen to be increasing from 3.45 A to 6.9 A at t = 1.2 s in Fig. 2.12(c). Similarly, when load is reduced from 2 to 1 kW at t = 1.8 s, the battery current comes down to 3.45 A from 6.9 A. As seen in Fig. 2.12(b), the battery voltage is nearly constant during this interval. The change in dc-link current is shown in Fig. 2.12(d) at the load power variations.

The simulation waveforms of regenerative mode are shown in Fig. 2.13. To verify this mode, the dc-link voltage is varied and battery is charged through a constant current. The dc-link voltage variations are between 290 V to 350 V, as shown in Fig.2.13(a). The battery voltage and current are shown in Fig. 2.13(b) and (c), respectively. Fig. 2.13(c), The battery current is kept constant at 3.5 A by controller irrespective of the dc-link voltage variations.

SET-2: In this set of simulation, the proposed converter is simulated at lower voltage and power levels which are used for experimental validation. The parameters used in this set are

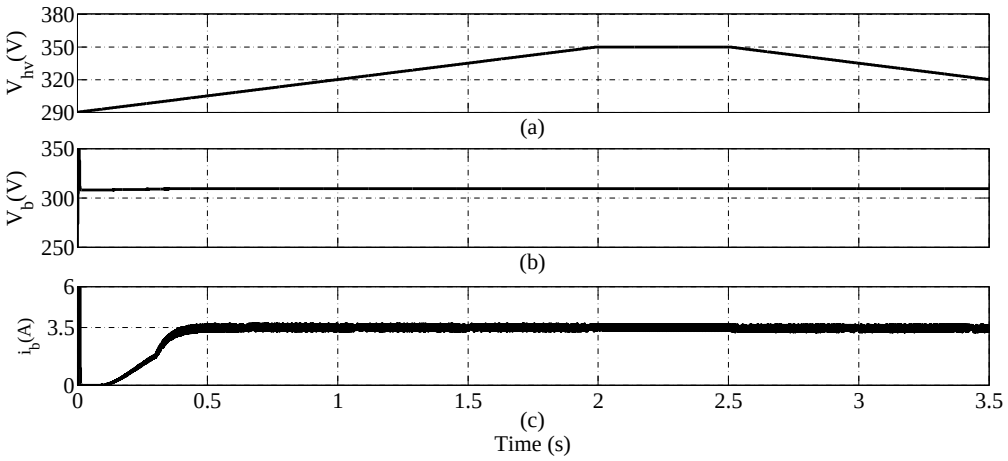

Fig. 2.13. Simulation of regenerative braking mode (a) dc-link voltage, (b) battery voltage, (c) battery current

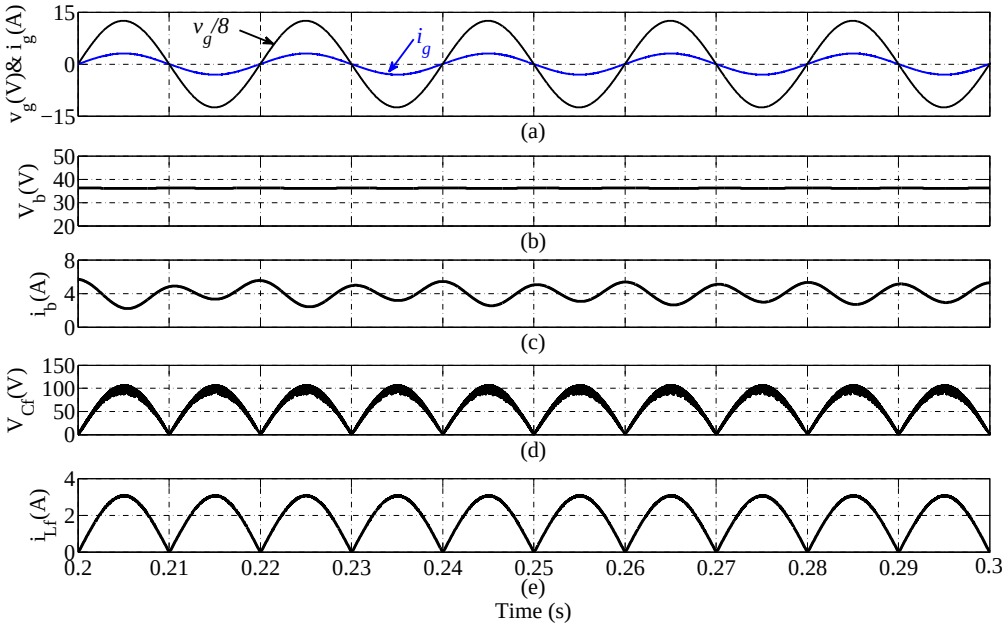

Fig. 2.14. Simulation waveforms of plug-in charging mode with 100 V (peak) grid voltage and 60 V battery voltage, (a) grid voltage and current, (b) battery voltage, (c) battery current, (d) filter voltage (V_{cf}), (e) filter inductor current (i_{Lf})

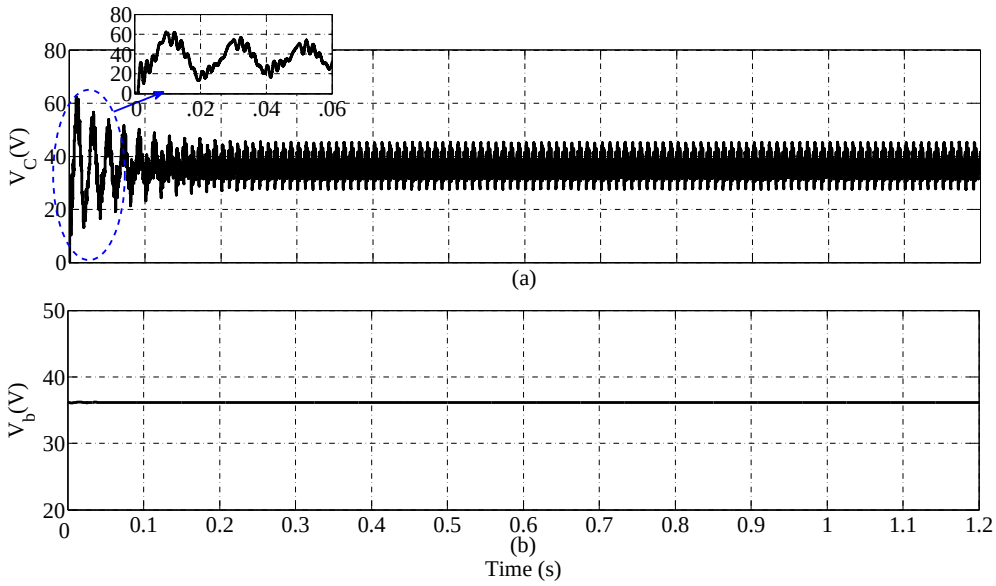

Fig. 2.15. Simulation aaveforms of (a) V_C, (b) V_b

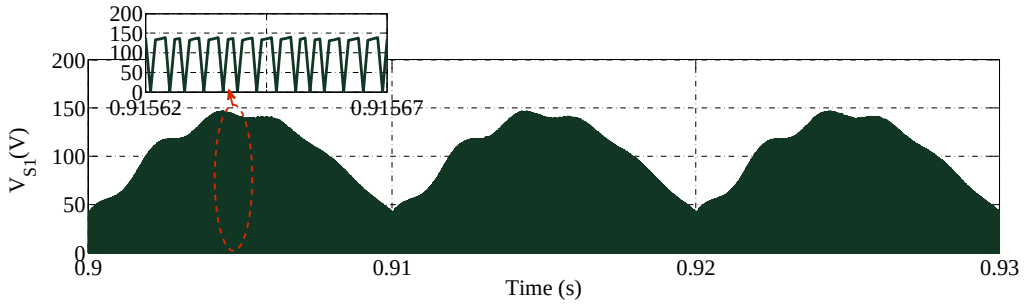

Fig. 2.16. Voltage waveform across switch S_1 in plug-in charging mode

given in Table 2.6.

In plug-in charging mode, the peak grid voltage is fixed at 100 V, charging power is 210 W and the nominal battery voltage is 36 V with 20% SOC. Fig. 2.14 shows simulated waveforms of this mode. It is seen from Fig. 2.14(a), the grid voltage and current are in the same phase with sinusoidal shape. The measured THD of the grid current and PF are around 3.53% and 0.999, respectively, which indicates the effectiveness of the converter operation at lower charging power, grid and battery voltages. The battery voltage and current are shown in Fig. 2.14 (b) and (c), respectively. The V_{cf} and i_{Lf} are also shown in Fig. 2.14(d) and (e), respectively. In Fig. 2.15(a), the voltage across capacitor C, i.e., V_C which follows the battery voltage (Fig. 2.15(b)), and ripple in the V_c depends on the battery voltage ripple and

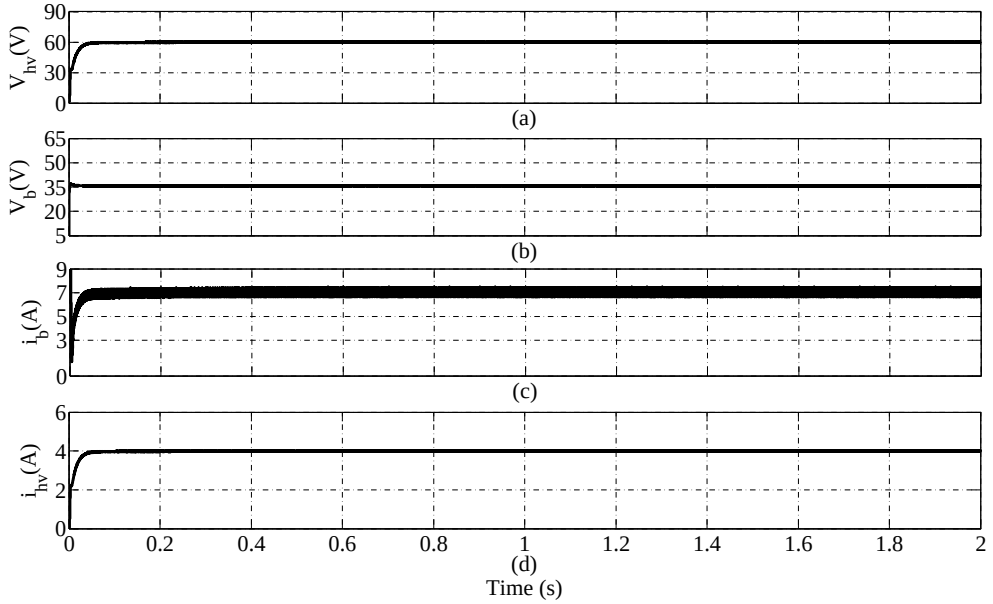

Fig. 2.17. Simulation waveforms during propulsion with 60 V battery, 100 V dc-link and 400 W load, (a) dc-link voltage, (b) battery voltage, (c) battery current, (d) dc-link current

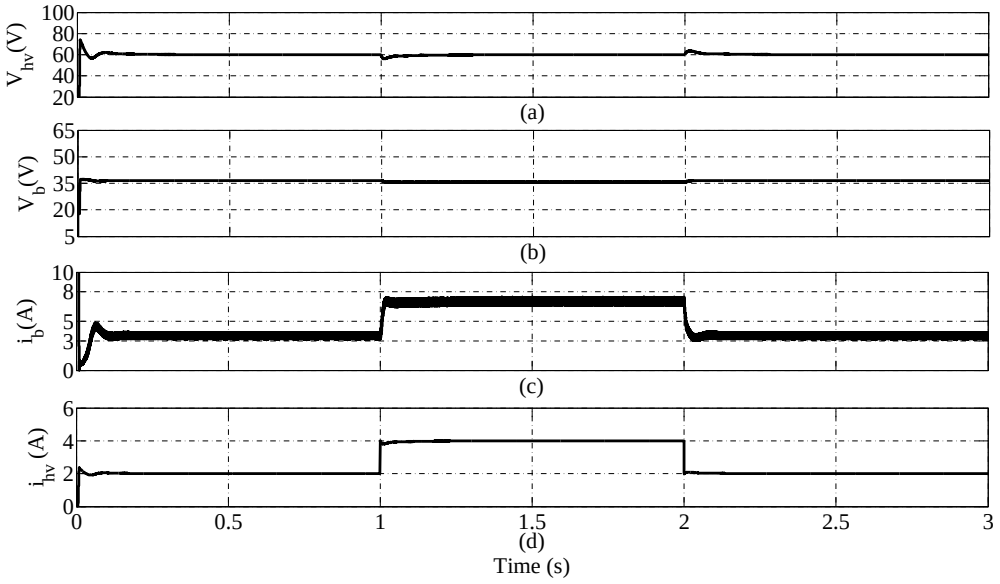

Fig. 2.18. The dynamic operation of propulsion mode with step load variations, (a) dc-link voltage, (b) battery voltage. (c) battery current, (d) dc-link current

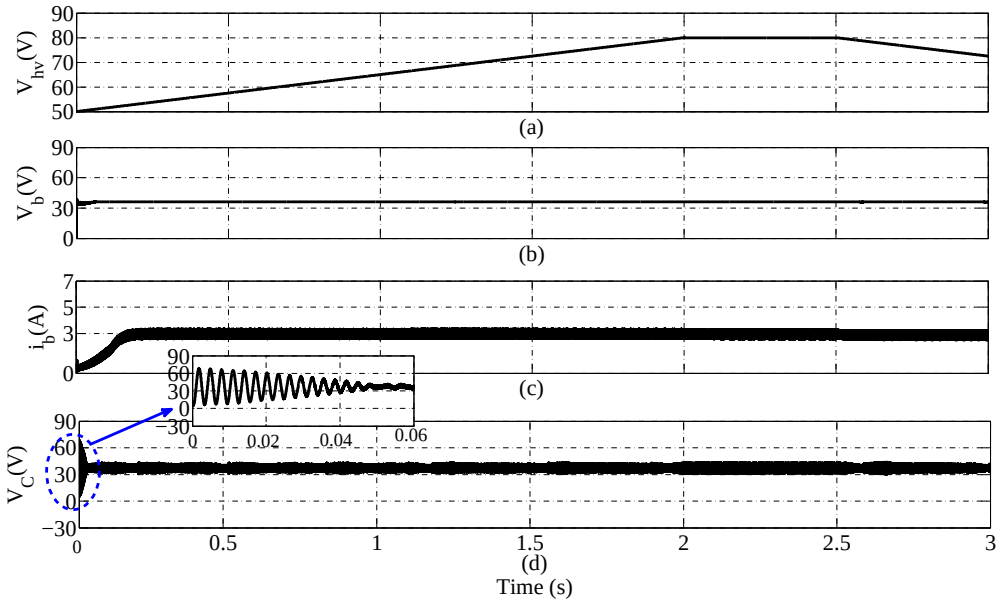

Fig. 2.19. Simulation waveforms of regenerative braking mode, (a) dc-link voltage, (b) battery voltage, (c) battery current, (d) capacitor voltage V_c

capacitance value of C. The voltage developed across switch S_1 is shown in Fig. 2.16 which is the sum of the battery and grid voltages.

Simulation of propulsion mode is done with 60 V dc-link voltage and 240 W load power, as shown in Fig. 2.17. Dynamic operation of the converter is verified by step load changes at t = 1 s from 120 to 240 W and 240 to 120 W at t = 2 s. From Fig. 2.18(a), the dc-link voltage is well regulated at reference value even after the load change which indicates controller is working effectively at the lower voltage and power ratings. The battery voltage, battery current and dc-link current are shown in Fig. 2.18 (b), (c) and (d), respectively. From Fig. 2.18(b), the battery current increases from 3.44 A to 6.89 A at t = 1 s. Similarly, when load is reduced from 240 to 120 W at t = 2 s, the battery current reduces to 3.44 A from 6.89 A. The dc-link current varies as 2-4-2 A at the load changes shown in Fig. 2.18(d).

The regenerative braking mode of this set is verified by linear variations in the dc-link voltage, as shown in Fig. 2.19. The dc-link voltage is linearly increased from 50 V, t = 0 s to 80 V, t = 2 s. It is held constant at 80 V between t = 2 s to t = 2.5 s, after t = 2.5 s, it is linearly reduced, as shown in Fig. 2.19(a), and the battery is charged with constant current of 3 A shown in Fig. 2.19(c). The voltage V_C follows the battery voltage, as shown in Fig.

Table 2.7. Experimental setup parameters

Parameters	Values
Grid voltage (v_g)	*42.42/70.7 V*
dc-link voltage (V_{hv})	*60 V*
Line frequency (f_L)	*50Hz*
Battery voltage (V_b)	*36 V*
Battery capacity	*26 Ah*
L_1/L_2	*2 mH*
C_{hv}/C_M/C_b	*550/10/2200 μF*

2.19(d).

2.8.2 Experimental results

The parameters and specifications of prototype model of the proposed converter are mentioned in Table 2.7. A field-programmable gate array (FPGA) based dSPACE-1104 controller is used for the development of the proposed converter. The isolation between controller and gate drivers of semiconductor switches is developed using the optocoupler TLP-250, which can be operated up to 25 kHz. For voltage protection of the switches, an RC snubber circuit is used along with driver circuit shown in Fig. 2.20. During plug-in charging mode, the grid voltage and output battery current are measured using voltage and current sensor, respectively. The dc-link voltage is also measured using voltage sensor. The grid current is measured through an ac current probe of FLUK power analyzer. A detailed explanation of experimental setup was discussed in Appendix A.

Figure 2.21 shows experimental waveforms during plug-in charging mode. During this mode when the battery is charged from the grid supply; the converter is operating in PFC. In Fig. 2.21, the grid current at CH1 has nearly sinusoidal shape and in phase with the grid voltage at CH2, which shows that the converter is operating under unity power factor condition. The battery current and battery voltage are shown at CH3 and CH4, respectively. The low frequency oscillation in the battery current is seen at CH3 of Fig. 2.21 which increases

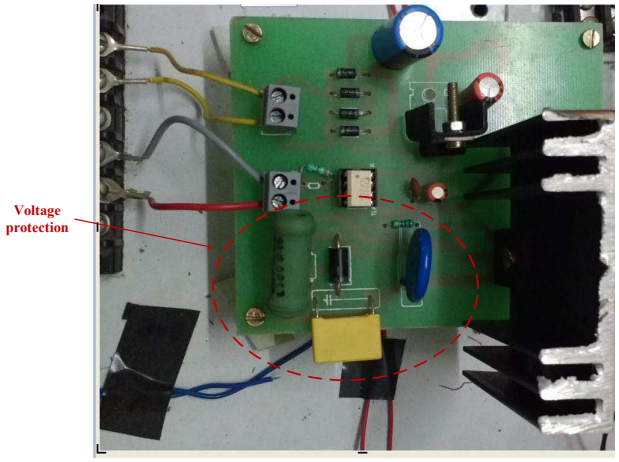

Fig. 2.20. Gate driver circuit of switch with voltage protection

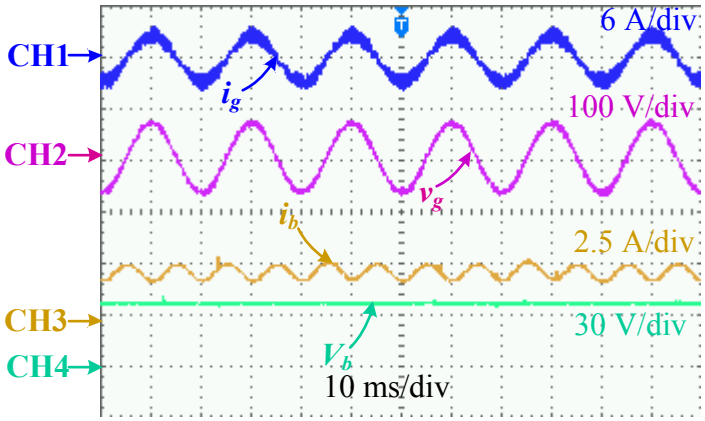

Fig. 2.21. Experimental waveforms of plug-in charging mode (CH1: grid current, CH2: grid voltage, CH3: battery current and CH4: battery voltage)

the reverse recovery losses of diode D_6; therefore, an inductive filter is connected at battery terminal to suppress this oscillation. The addition of this filter depends on manufacturer and battery capability to absorb low frequency ripple current without impairing its life. In PFC operation, it is mandatory to connect an LC filter after rectifier bridge diode to filter out discontinuous input current. The waveforms of filter capacitor voltage and filter inductor current are shown in Fig. 2.22. The voltage across coupling capacitor C is same as output voltage, i.e., battery voltage, which is shown in Fig. 2.23. From Fig. 2.24, the measured power factor is 0.99, and total harmonic distortion (THD) is 7.1%. The high PF operation of the proposed converter relieves the grid of reactive power burden and reduces the cost

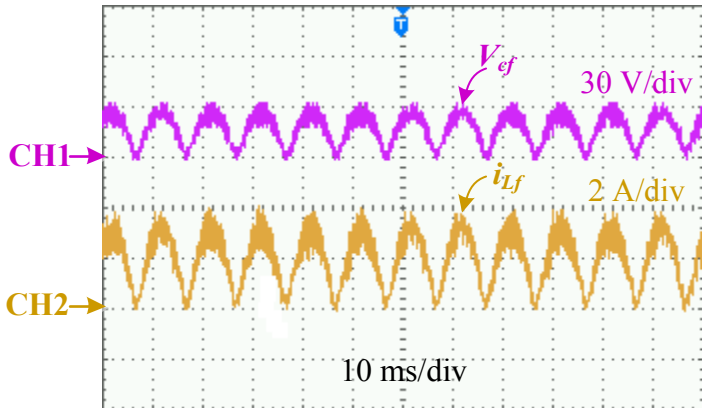

Fig. 2.22. Experimental waveforms of grid side filter voltage and current (CH1: V_{cf} and CH2: i_{Lf})

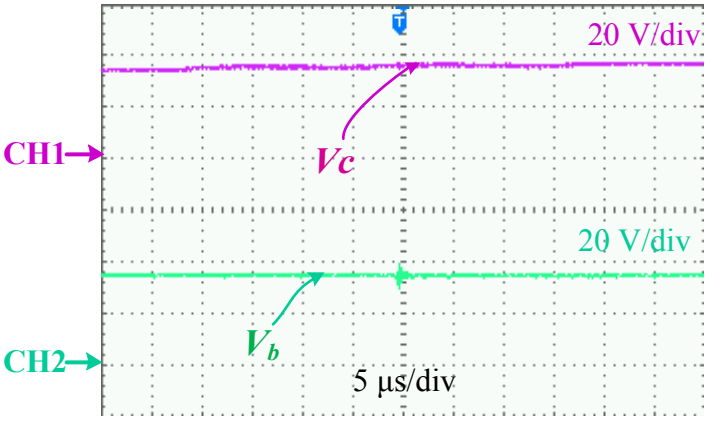

Fig. 2.23. Experimental waveforms of coupling capacitor and battery voltage (CH1: coupling capacitor voltage and CH2: battery voltage)

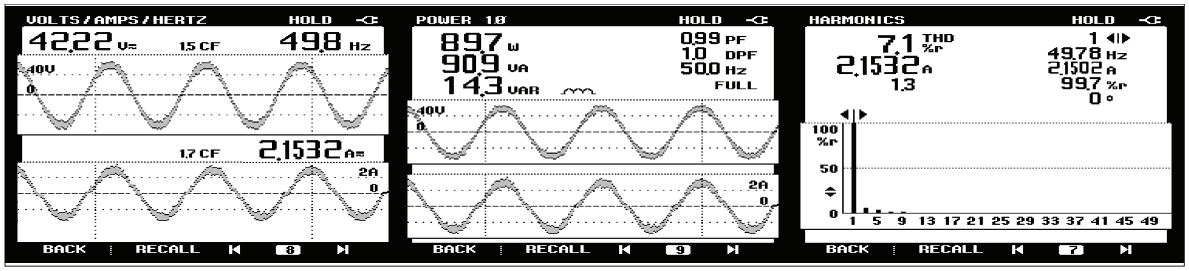

Fig. 2.24. Waveforms of grid voltage, grid current and Power quality parameters

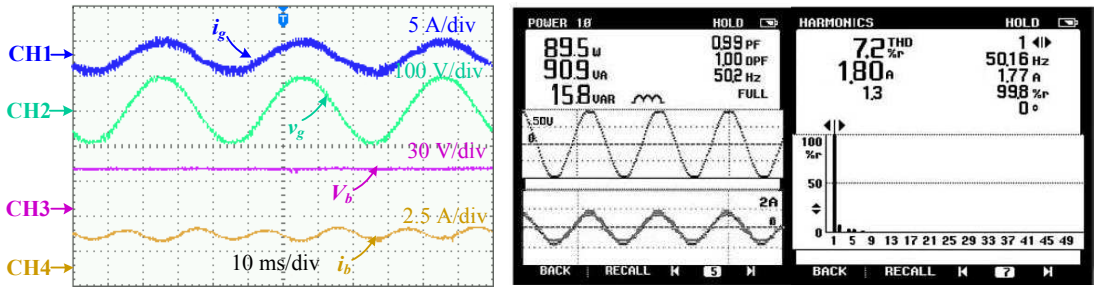

(a) (b)

Fig. 2.25. Experimental waveforms of plug-in charging mode (CH1: grid current, CH2: grid voltage, CH3: battery current and CH4: battery voltage, (b) power quality parameters

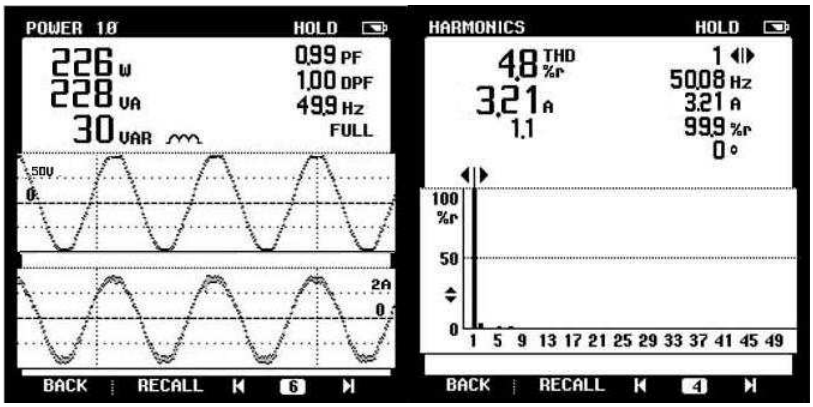

Fig. 2.26. Power quality parameters with 210 W charging power

of electricity. Furthermore, with 100 V (peak) grid voltage and 85 W charging power (Fig. 2.25(a)), the measured PF and THD of the grid current are 0.99 and 7.2%, respectively, as shown in Fig.2.25(b). The measured input power p_g is 89.5 W at 85 W charging power P_b; therefore, calculated efficiency is 94.9% . With 210 W charging power and 100 V (peak) grid voltage, the measured input power is 226 W (Fig. 2.26) and calculated efficiency is 92.9%, which is lower compared to 85 W charging power, it is due to fact that conduction losses in the switches and inductors significantly increase at higher power.

In propulsion mode, the battery voltage is either stepped up or stepped down depending on the battery SOC and dc-link voltage. Fig. 2.27 shows screenshot of oscilloscope with 125 W load and 60 V dc-link. The control objective of this mode is to keep the dc-link voltage

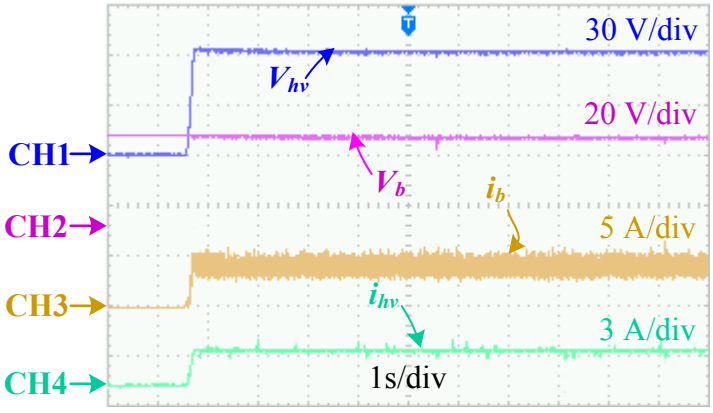

Fig. 2.27. Experimental waveforms during propulsion mode (CH1: dc-link voltage, CH2: battery voltage, CH3: battery current and CH4: dc-link current)

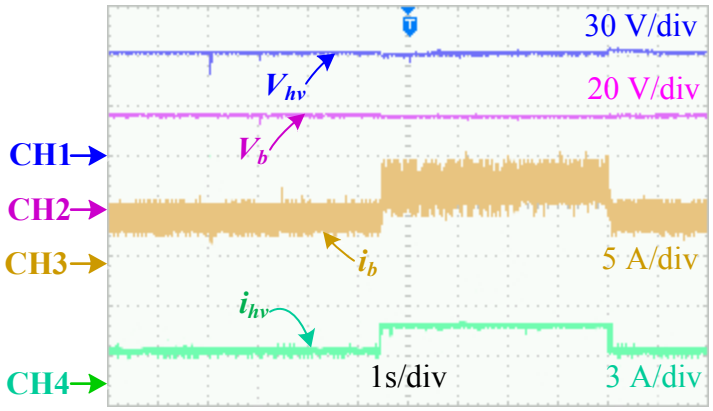

Fig. 2.28. The dynamic performance of the converter in propulsion mode (CH1: dc-link voltage, CH2: battery voltage, CH3: battery current and CH4: dc-link voltage)

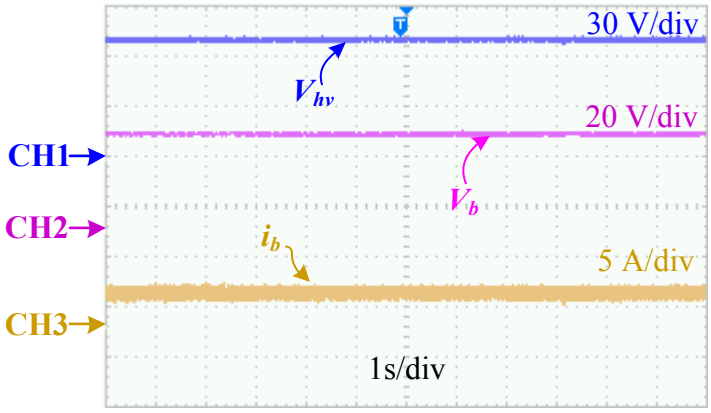

Fig. 2.29. Experimental waveforms during regenerative mode (CH1: dc-link current, CH2: battery voltage and CH3: battery current)

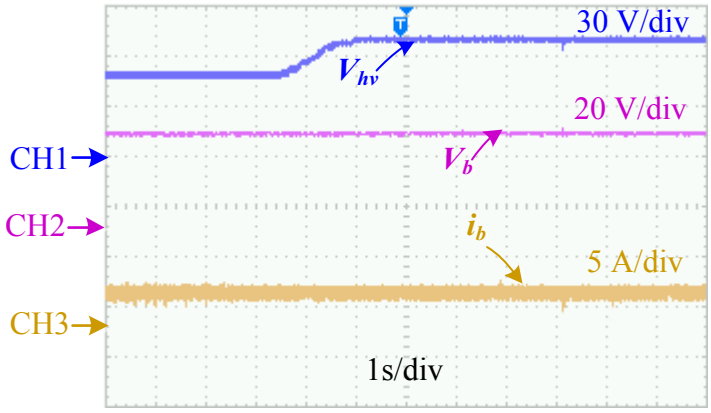

Fig. 2.30. Experimental waveforms of regenerative mode with dc-link voltage variations (CH1: dc-link voltage, CH2: battery voltage and CH3: battery current)

constant for smooth operation of inverter-drive system. The dynamic performances for this mode is tested with step load changes from 125 to 215 W and from 215 W to 125 W. The measured dc-link voltage is regulated at reference value even after the load change, which is shown in Fig. 2.28 at CH1. The corresponding change in the battery voltage, battery current and load current are shown in Fig. 2.28 at CH2, CH3 and CH4, respectively.

In regenerative mode, the battery is charged by converting the mechanical energy (stored in rotating parts) into electrical energy. The generated EMF across the machine terminals is rectified through the feedback diodes of the inverter to develop a dc link voltage proportional to rotor speed. In the present work, this mode is tested by rectifying ac voltage, which is

applied through an auto-transformer. The relevant waveforms of this mode are shown in Figs. 2.29 and 2.30. In Fig. 2.29, the dc-link voltage has been fixed at 70 V, and the battery is charged with 2.78 A current. In Fig. 2.30, the dc-link voltage is varied between 45 V to 70 V, and the battery current remains constant at 2.78 A through closed loop control scheme.

2.9 Conclusion

The integrated converter proposed in this Chapter operates as ZETA converter for plug-in charging and regenerative braking modes, while for propulsion mode it operates as SEPIC converter. Due to this, it exhibits buck/boost capabilities for each of these modes of operation without voltage inversion, which allows selection of a wide range of the battery voltages, efficient control of dc-link voltage and capture of the regenerative braking energy over a wide range of motor speed. In comparison to the existing single-stage converters with similar buck/boost capabilities in each mode, the proposed converter has fewer components. The functionality and performance of the proposed integrated converter have been verified through extensive simulation and hardware results. The performance of control algorithm is tested with step load variations in propulsion mode and dc-link voltage variations in regenerative braking mode. The detailed stress analysis and loss analysis of the proposed converter is investigated to select the power stage switches. The maximum theoretical efficiency of the converter in plug-in charging, propulsion and regenerative braking modes has been computed as 95.1%, 96.1% and 96.7%, respectively. The measured THDs in the experiment are found as 7.1% for 85 W charging power, 60 V(peak) grid voltage and 4.8% for 210 W charging power, 100 V (peak) grid voltage.

CHAPTER 3

MODIFIED ZETA BASED INTEGRATED CONVERTER

3.1 Introduction

The ZETA-SEPIC based integrated converter discussed in Chapter 2 has many advantages, but has limitation of high voltage/current stresses (sum of the input/output quantities (voltage/current)) on semiconductor devices. The voltage stress on semiconductors devices during propulsion and regenerative braking modes is the sum of dc-link voltage and battery voltage, which is higher to the voltage stress in plug-in charging mode (sum of grid voltage and battery voltage). Moreover, the power rating of propulsion mode is usually much higher than other two modes. Therefore, high stresses in propulsion mode is a downside for vehicle application. To overcome the limitation of ZETA-SEPIC based integrated converter, a modified ZETA based integrated converter has been proposed with reduced stresses in propulsion and regenerative modes. The proposed converter in this chapter is derived by modifying conventional ZETA converter with addition of a mechanical switch shown in Fig. 3.1. Also, the converter has higher efficiency in these two modes over existing integrated converters [95,98,99]. The higher efficiency in propulsion and regenerative braking modes leads to a longer run of vehicle per charging. The detailed analysis, voltage/current stresses and efficiency and loss calculation have been carried out for the proposed converter.

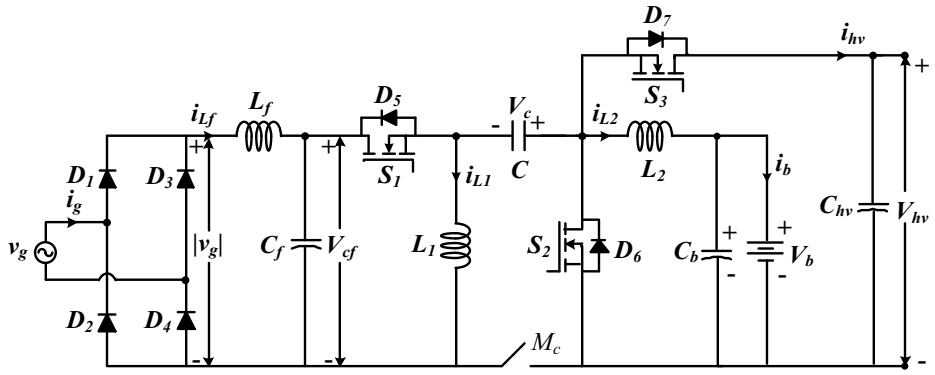

Fig. 3.1. Proposed modified ZETA based integrated converter

3.2 Operation of the Proposed Converter

The proposed integrated converter shown in Fig. 3.1 consists of three semiconductor switches, one mechanical ON-OFF switch, two inductors (excluding filter inductor), three capacitors (excluding filter capacitor) and one bridge rectifier. In the following Sections, the operation of converter in each mode is discussed in detailed manner.

3.2.1 Plug-in charging mode

The plug-in charging mode of vehicle is possible only when vehicle is not in motion and the charger plug is connected to single phase supply socket to charge the battery.

In this mode, converter operates as ZETA PFC converter and switch S_1 is gated through a PWM and mechanical ON-OFF switch M_c is always ON while switches S_2 and S_3 are OFF-state. When switch S_1 is turned ON, inductor L_1 stores energy through the path $|v_g|$-L_1-S_1-$|v_g|$ and inductor L_2 stores energy through the path $|v_g|$-S_1-*C*-L_2-V_b- $|v_g|$, as shown in Fig. 3.2(a). The current through both the inductors increases linearly, as shown in Fig. 3.2 (c). When switch S_1 is turned OFF, inductor L_1 charges the capacitor *C* through the body diode of S_2, and inductor L_2 supplies energy to the output stage (battery), as shown in Figure 3.2(b).

Let us assume that the duty ratio of the switch S_1 is d_1. The volt-seconds balance of inductor L_1 or L_2 in switching period T_s can be written as

$$V_{g,max}|sin(\omega t)| * d_1(t) = v_b * (1 - d_1(t)) * T_s \tag{3.1}$$

From (3.1), the voltage conversion ratio M_1 is expressed as

$$M_1 = \frac{V_b}{V_{g,max}\,|\sin \omega t|} = \frac{d_1(t)}{1 - d_1(t)} \tag{3.2}$$

3.2.2 Propulsion mode

In this mode, switch M_c, semiconductor switches S_1 and S_3 are OFF and switch S_2 is operated through a PWM signal. When S_2 is turned ON, inductor L_2 stores energy through the path V_b-L_2-S_2-V_b (blue solid line), as shown in Fig.3.3(a), and when S_2 is turned OFF, inductor L_2 transfers its stored energy to the dc-link capacitor through the diode D_7 (red dotted line). The operation of converter in this mode is same as the operation of conventional boost converter.

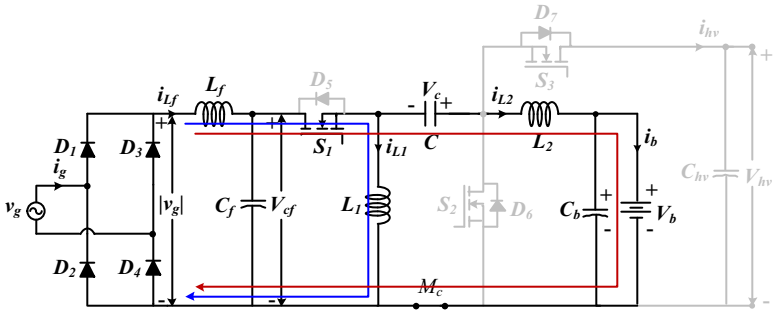

(a)

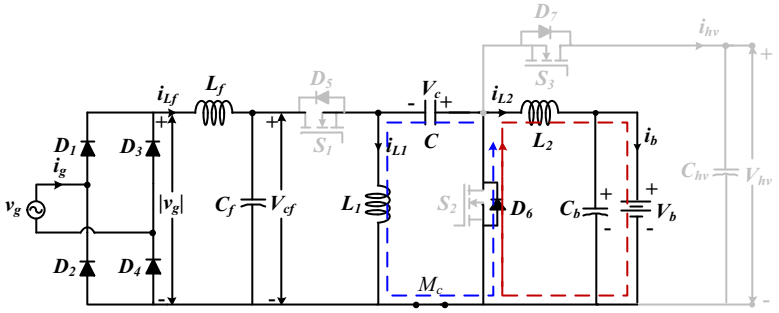

(b)

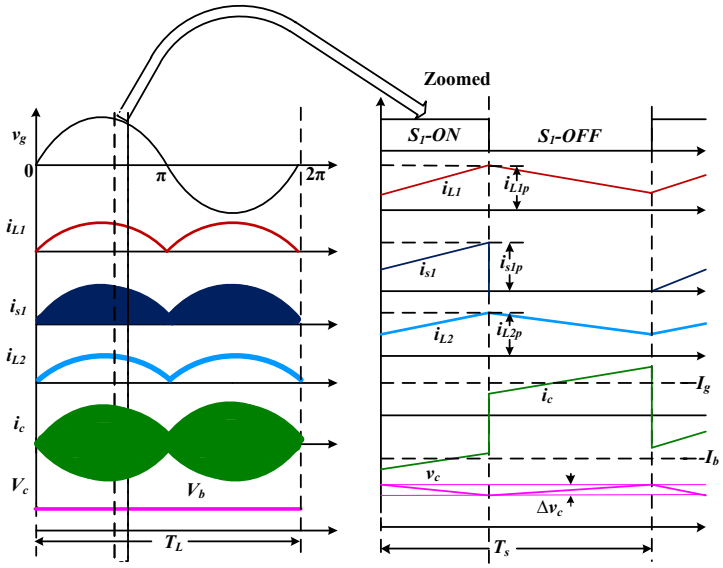

(c)

Fig. 3.2. Operation of the converter during plug-in charging mode, (a) switch S_1 is ON, (b) switch S_1 is OFF. (c) Waveforms over one line cycle and one switching cycle

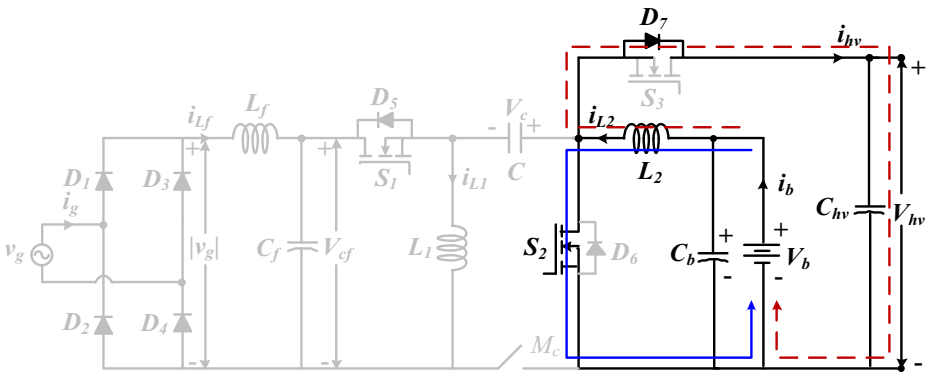

(a)

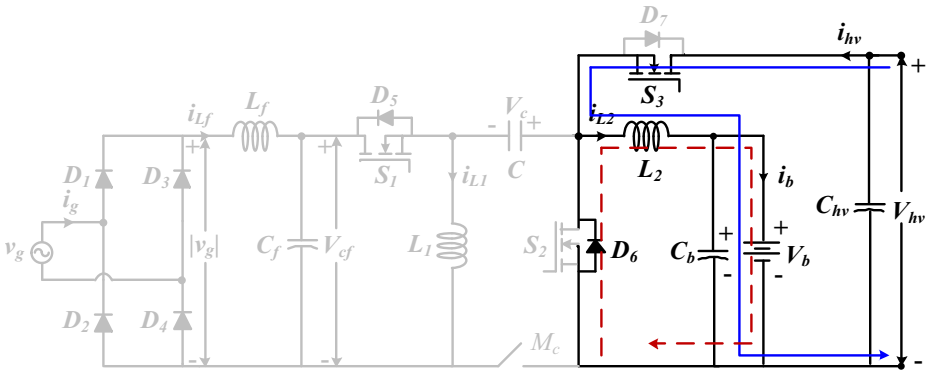

(b)

Fig. 3.3. Operation of converter during (a) propulsion mode, (b) regenerative braking mode

Let us assume that the duty ratio of the switch S_2 is d_2. The volt-second balance of inductor L_2 in switching period T_s can be written as

$$V_b * d_2 * T_s = (V_b - V_{hv}) * (1 - d_2) * T_s \tag{3.3}$$

The voltage conversion ratio M_2 from (3.3) is expressed as

$$M_2 = \frac{V_{hv}}{V_b} = \frac{1}{1 - d_2} \tag{3.4}$$

3.2.3 Regenerative braking mode

The operation of the converter in this mode is same as conventional buck-converter operation.

In regenerative braking mode, buck operation of converter is typically required when motor back EMF is higher than the battery voltage. The braking energy is then used to

Table 3.1. Peak voltage and current stresses on switches

Mode	S_1		S_2		S_3	
	Voltage	**Current**	**Voltage**	**Current**	**Voltage**	**Current**
Plug-in charging	$[v_g(\omega t)_{\omega t=\pi/2} + V_b]$	$[i_g(\omega t)_{\omega t=\pi/2} + I_b]$	$[v_g(\omega t)_{\omega t=\pi/2} + V_b]$	$[v_g(\omega t)_{\omega t=\pi/2} + V_b]$	$[v_g(\omega t)_{\omega t=\pi/2} + V_b]$	NC
Propulsion	[NIL]	NC	$[V_{hv}]$	$[\langle i_{L2prop}\rangle_{Ts} + \frac{\triangle i_{L2prop}}{2}]$	$[V_{hv}]$	$[\langle i_{L2prop}\rangle_{Ts} + \frac{\triangle i_{L2prop}}{2}]$
Regenerative braking	[NIL]	NC	$[V_{hv}]$	$[\ \langle i_{L2rege}\rangle_{Ts} + \frac{\triangle i_{L2rege}}{2}]$	$[V_{hv}]$	$[\ \langle i_{L2rege}\rangle_{Ts} + \frac{\triangle i_{L2rege}}{2}]$

where NC = Not conducting, NIL = 0 voltage, i_{L2prop} and i_{L2rege} are inductor L_2 current in propulsion and regenerative braking modes.

Table 3.2. RMS and average current stresses on switches and diodes

Device	Plug-in charging		Propulsion		Regenerative braking	
	RMS	**Average**	**RMS**	**Average**	**RMS**	**Average**
S_1	$I_{g,RMS}\sqrt{1+\alpha\frac{8}{3\pi}}$	$I_{g,RMS}\frac{2\sqrt{2}}{\pi}$	NC			
S_2	NC		$\sqrt{I_b^2 d_2 + \frac{d_2^3 V_b}{12 f_s^2 L_2^2}}$	$d_2 I_b$	NC	
S_3			NC		$\sqrt{I_b^2 d_3 + \frac{d_3(1-d_3)^2 V_b^2}{12 f_s^2 L_2^2}}$	$d_3 I_b$
M_c	$I_{g,RMS}\sqrt{\alpha\frac{8}{3\pi}}$	0	NC			
D_5			NC			
D_6	$I_b\sqrt{\frac{3}{2}+\frac{16}{3\pi}\alpha}$	$\frac{I_{g,RMS}2\sqrt{2}}{\pi}\alpha$	NC		$\sqrt{I_b^2(1-d_3) + \frac{(1-d_3)^3 V_b^2}{12 f_s^2 L_2^2}}$	$I_b(1-d_3)$
D_7	NC		$\sqrt{I_b^2(1-d_2) + \frac{d_2(1-d_2)V_b^2}{12 f_s^2 L_2^2}}$	$I_b(1-d_2)$	NC	
L_f, L_1	$I_{g,RMS}$	$I_{g,RMS}\frac{2\sqrt{2}}{\pi}$	NC			
L_2	$I_{g,RMS}\alpha\sqrt{\frac{3}{2}}$	$\frac{I_{g,RMS}}{2}\alpha$	$\frac{2}{\sqrt{3}}I_b$	I_b	$\frac{2}{\sqrt{3}}I_b$	I_b

where NC = Not conducting.

charge the battery. Switch M_c is permanently OFF and switch S_3 is PWM gated and the remaining semiconductor switches are OFF. When switch S_3 turned ON, inductor L_2 stores energy through the path indicated by blue solid line in Fig. 3.3(b). When S_3 is turned OFF L_2 transfers its stored energy to the output stage via the path shown by a dotted red line in Fig. 3.3(b).

Let us assume that duty ratio of the switch S_3 is d_3. The volt-second balance of inductor L_2 in switching period T_s is given as

$$(V_{hv} - V_b) * d_3 * T_s = V_b * (1 - d_3) * T_s \tag{3.5}$$

The voltage conversion ratio M_3 from (3.5) is expressed as

$$M_3 = \frac{V_b}{V_{hv}} = d_3 \tag{3.6}$$

3.3 Selection of Components

3.3.1 Selection of switching devices

Due to bidirectional operation in the dc/dc stages some of the switches/diodes are shared between ac/dc and dc/dc stages. The voltage and current stresses on switches/ diodes may be different in each mode due to different power and voltage rating of these mode. Hence, the selection of voltage/current rating of a particular switch is decided by the peak voltage/current developed in switch or its body diode during any mode. Table 3.1 shows the peak voltage and current stresses of switches in each mode. From this Table, switch rating is selected as follows:

The peak voltage rating of S_1 is given as: ($v_g(\omega t)_{\omega t=\pi/2}$ +V_b), and the peak current rating of S_1 is $i_g(\omega t)_{\omega t=\pi/2}$ +I_b. The peak voltage rating of S_2 is decided as max (V_{hv}, $v_g(\omega t)_{\omega t=\pi/2}$ +V_b) and peak voltage rating of switch S_3 is chosen as V_{hv}. While current rating of S_2 and S_3 are chosen by propulsion mode power rating.

3.3.2 Selection of passive components

Except inductor L_2, selection of passive components is same as the ZETA-SEPIC based integrated converter. Therefore, this Section only deals selection of inductor L_2.

Inductor L_2 participates in all mode of converter operation. Therefore, the CCM condition of the converter for each mode can be ensured by selecting the inductor value for each of these modes with allowable current ripple. The maximum of these computed values is picked up as the value of inductor L_2.

The value of L_2 for CCM operation in plug-in charging mode is given as [91]

$$L_{2_{plug-in}} = \frac{V_b\,(1-d_2)}{\Delta i_b f_s} = \frac{V_b d_2}{\Delta i_g f_s} = \frac{V_b}{\Delta i_g f_s}\left(\frac{V_b}{V_{g,\max}+V_b}\right) \tag{3.7}$$

where Δi_g is the grid ripple current.

The values of L_2 for CCM operation in propulsion and regenerative braking modes are

given by following equation as [105, 106]

$$L_{2_{prop}} = \frac{V_b d_2}{\Delta i_b f_s} \tag{3.8}$$

$$L_{2_{reg}} = \frac{V_b(1-d_3)}{\Delta i_b f_s} \tag{3.9}$$

where Δi_b is the battery ripple current.

The final value of L_2 is selected as

$$L_2 = max(L_{2_{plug-in}}, L_{2_{pop}}, L_{2_{reg}}) \tag{3.10}$$

3.4 Loss Analysis

In this Section, a loss analysis of the proposed converter is investigated in each mode. The conduction, switching and reverse recovery losses for 1200 V/100 A switch in each mode are analytically calculated using manufacturers data-sheet and loss expressions given in Chapter 2 Section 2.5.2). To find the efficiency of the converter, the passive components losses are also calculated in this Section.

Total losses of semiconductor and mechanical switches P_S is given as

$$P_S = P_{S,cond} + P_{sw} + P_D + P_{M_c} \tag{3.11}$$

where $P_{S,cond}$, P_{sw}, P_D and P_{M_c} are switch conduction loss, switching loss, diode conduction loss and conduction loss in switch M_c, respectively. The above expression (3.11) is used for loss calculation in ac/dc stage (plug-in charging mode). To use (3.11) for loss calculation in dc/dc stage (propulsion and regenerative braking modes), P_{M_c} component will be discarded.

Then total passive components losses P_P for ac/dc and dc/dc conversion stages is given as

$$P_P = P_{Lf} + P_{L1} + P_{L2} + P_c \tag{3.12}$$

where P_{Lf}, P_{L1}, P_{L2} and P_c are the ohmic loss of the L_f, L_1, L_2 and C, respectively. The above expression (3.12) is used for ac/dc stage. To use (3.12) for dc/dc stage, only inductor L_2 loss, i.e., P_{L2} is considered.

Table 3.3. A loss breakdown of the system in ac/dc and dc/dc stages with 400 V dc-link and 300 V battery

Mode	$\mathbf{P_{S,cond}}$ [W]	$\mathbf{P_{sw}}$ [W]	$\mathbf{P_D}$ [W]	P_{M_c} [W]	$\mathbf{P_{Lf}}$ [W]	$\mathbf{P_{L1}}$ [W]	$\mathbf{P_{L2}}$ [W]	$\mathbf{P_c}$ [W]
Plug-in charging (ac/dc stage) [240 V, 3.2 kW]	28.05	27.45	60.93	8.38	10.6	19.55	17.8	0.74
Propulsion (dc/dc stage) [10 kW]	41.75	35.49	72.5	– –	– –	—-	122.22	—-
Regenerative braking (dc/dc stage) [1 kW]	6.83	2	6.87	– –	– –	– –	5.1	– –

Table 3.4. Total losses of the proposed converter in ac/dc and dc stages with $V_b = 300$ V and $V_{hv} = 400$ V

				Total semiconductors losses, $\mathbf{P_S}$ [W]			Total passive components losses, $\mathbf{P_p}$ [W]		
$\mathbf{P_{ch}}$[kW]	$\mathbf{P_{prop}}$ [kW]	$\mathbf{P_{reg}}$ [kW]	$\mathbf{V_{grid}}$	Plug-in charging (ac/dc stage)	Propulsion (dc/dc stage)	Regenerative braking (dc/dc stage)	plug-in charging (ac/dc stage)	Propulsion (dc/dc stage)	Regenerative braking (dc/dc stage)
1.8	10	0.5	120	119.49	149.74	13.9	45	122.22	1.1
3.2	10	0.5	240	125.31	149.74	13.9	48	122.22	1.1
1.8	15	1	120	119.49	245	15.7	45	275	4.4
6.6	15	1	240	288.646	245	15.7	190.1	275	4.4
1.8	20	1.5	120	119.49	301.6	21.75	45	488.88	6.6
6.6	20	1.5	240	288.646	301.6	21.75	190.1	488.88	6.6

Using loss equations given in Section 2.5.2, the loss calculation of each components in each mode at rated power has been given in Table 3.3.

Further, Table 3.4 shows P_S and P_p in each mode for various ac/dc and dc/dc power levels where P_{ch}, P_{prop} and P_{reg} denote power rating of plug-in charging, propulsion and regenerative braking modes, respectively. It is seen from Table 3.4, the P_S in ac/dc stage with grid voltage of 240 V is between 3.9-4.3% of the rated power (3.2 and 6.6 kW) for mentioned switching device. While with 120 V grid voltage, the P_S in ac/dc stage is 6.6% of the rated power (1.8 kW). The P_S in dc/dc stage is between 1.4-1.8% of the rated power (10, 15 and 20 kW) which is lower than ac/dc stage. It is due to high stresses in semiconductor devices leading to higher switching and conduction losses as well as switch M_c and rectifier diodes losses. The P_P in ac/dc stage is between 2.5-2.8% of the rated power. The P_p in dc/dc stage varies between 0.22-2.5% of the rated power which is lower than ac/dc stage. It is because

Table 3.5. Comparison of the proposed converter with conventional single-stage converters

Charger topologies	Voltage Polarity	Switch	Diode	Inductor	Battery voltage range
Boost PFC converter	+	3	5	2	$V_{gridpeak}$-V_{bmax}
Bridgeless boost PFC converter	+	4	2	2	$V_{gridpeak}$-V_{bmax}
Inverting buck/boost PFC converter	-	3	5	2	0-V_{bmax}
Cuk PFC converter	-	3	5	3	0-V_{bmax}
SEPIC PFC converter	+	3	5	3	0-V_{bmax}
Integrated converter [98]	+	4	4	1	$V_{gridpeak}$-V_{bmax}
Integrated converter [99]	+	5	1	1	$V_{gridpeak}$-V_{bmax}
Integrated converter [95]	+	6	9	1	0-V_{bmax}
Proposed integrated converter	+	3	4	2	0-V_{bmax}

only one magnetic component i.e. L_2 is present in the current path. Moreover, the lower losses in the dc/dc stage will enable the vehicle to cover longer distance for the given battery charge.

3.5 Comparison with Single-Stage Chargers

The conventional single-stage battery charger topologies are namely the boost PFC converter, bridgeless boost PFC converter, inverting buck/boost PFC converter, SEPIC PFC converter, and Cuk PFC converter. In order to have a fair comparison of the proposed converter with these single-stage chargers, the dc/dc converter connected between the battery and dc-link, is assumed to be a two-quadrant bidirectional converter. The boost PFC converter can only charge the battery when battery voltage is more than the peak grid voltage ($V_b > V_{g,max}$). The problems of inverting buck/boost and Cuk converter have been discussed in Chapter 2 (Section 2.6). However Cuk and SEPIC PFC based converter topologies have an additional inductor compared to the proposed integrated converter (excluding filter inductor because it may present in other converters). In addition to these conventional chargers, other existing integrated chargers are also included in this comparative analysis. It is observed from Table 3.5 that the proposed converter has fewer components compared to the converters which has wide voltage conversion ratio (buck/boost operation) in plug-in charging mode, also the proposed converter has lower voltage/current stresses in propulsion and regenerative braking similar to other conventional / integrated converters. The efficiency curves of the proposed

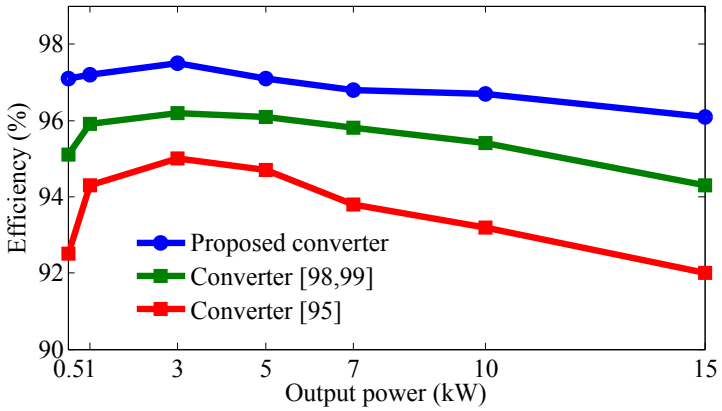

(a)

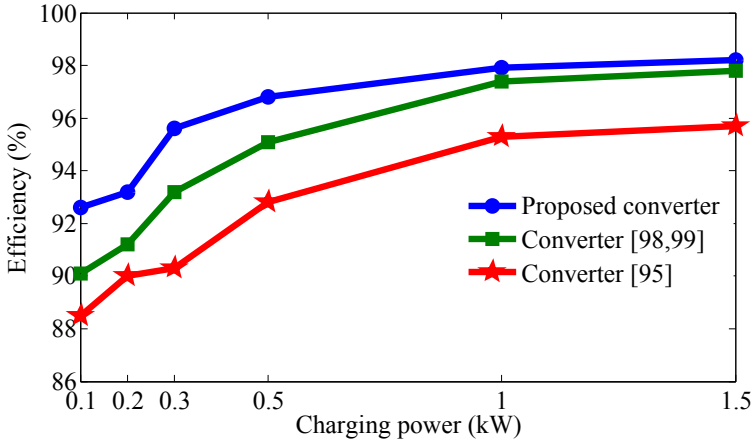

(b)

Fig. 3.4. Efficiency comparison, (a) propulsion mode, (b) regenerative braking mode

converter and existing integrated converters are shown in Fig. 3.4. The proposed converter has higher efficiency in propulsion and regenerative braking modes than the integrated converters [95,98,99], because in these converters three or four semiconductor devices are in the current path, while in the proposed converter only one semiconductor device is in the current path.

3.6 Simulation and Experimental Results

The simulation of the proposed converter is performed in MATLAB/Simulink environment with parameters of the converter listed in Table 3.6. The simulation and experimentatal studies are conducted for plug-in charging, propulsion and regenerative braking modes are discussed separately.

Table 3.6. Simulation parameters

Parameters	**Values**
Grid voltage (v_g)	220/42.42 V
Charging power (P_b)	1kW/100 W
dc-link voltage (V_{hv})	*400/ 60 V*
Line frequency (f_L)	*50 Hz*
Nominal battery voltage (V_b)	*300/36 V*
L_1/L_2	*3 mH*
C_{hv}/C_M/C_b	*550/10/2200μF*

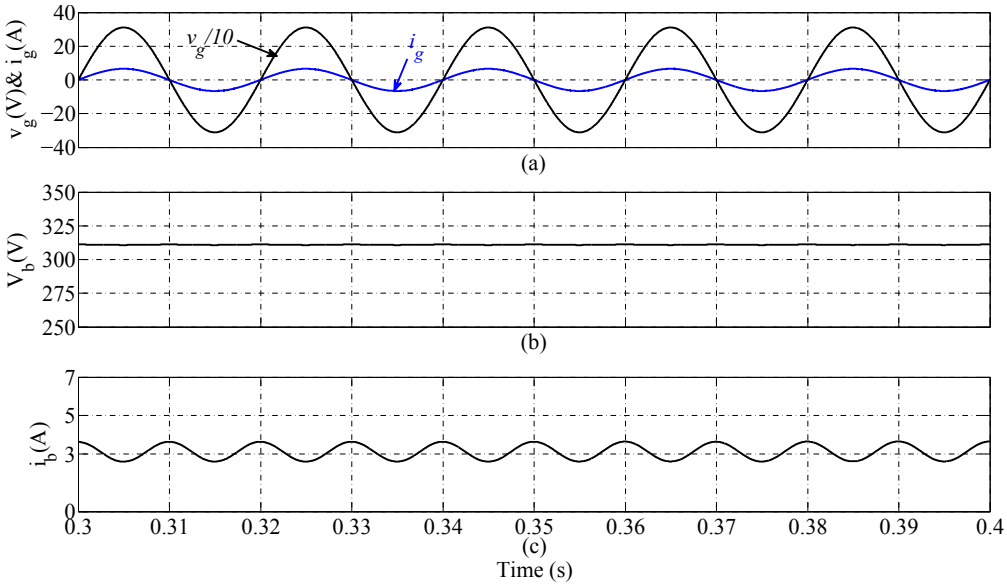

Fig. 3.5. Simulation waveforms of plug-in charging mode (a) grid voltage and grid current, (b) battery voltage, (c) battery current

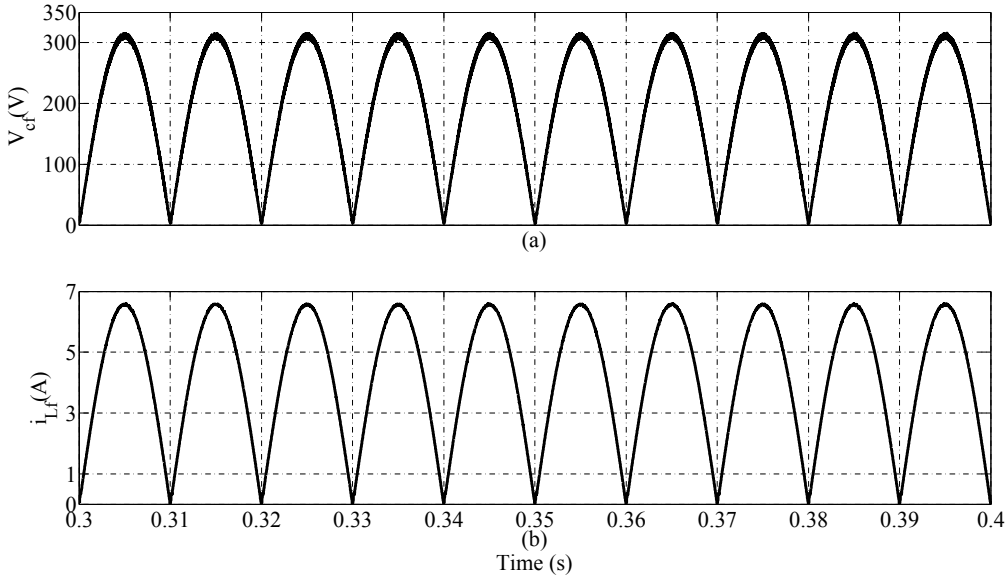

Fig. 3.6. Simulation waveforms of plug-in charging mode, (a) voltage across C_f, (b) current through L_f

The simulation waveforms during grid plug-in charging mode are shown in Figs. 3.5 and 3.6. In Fig. 3.5, the grid voltage (v_g) and the grid current (i_g) are in phase with sinusoidal shape, which shows converter is operating in near unity PF condition. The measured RMS grid current is 4.85 A at 220 V. The calculated power at grid side is 1.067 kW hence, efficiency of the converter is 94.7% for 1 kW load. Fig. 3.5(b) shows the battery voltage (V_b) which is close to 307 V with 20% SOC and the measured average battery current (i_b) is found to be 3.25 A, which is shown in Fig. 3.5(c). The voltage across filter capacitor (C_f) and current through filter inductor (L_f) are shown in Fig. 3.6(a) and (b), respectively. The peak voltage across C_f is 311 V, which is same as the peak grid voltage and the peak current through L_f is 6.7 A.

In propulsion mode, the battery voltage is stepped up to desired dc link voltage for satisfactory operation of motor-drive system. The simulation waveforms of dc-link voltage, battery voltage, dc-link current and voltage across switch (S_2) with 2 kW load are shown in Fig. 3.7(a), (b), (c) and (d), respectively. In this mode, switch S_2 is operated with PWM signal for boosting the battery voltage to desired dc-link voltage. The voltage across S_2 is equal to the dc-link voltage, as shown in Fig. 3.7(d). Fig. 3.8 shows simulation results of propulsion mode with step load changes. At t = 1.2 s load is decreased from 2 kW to 1 kW

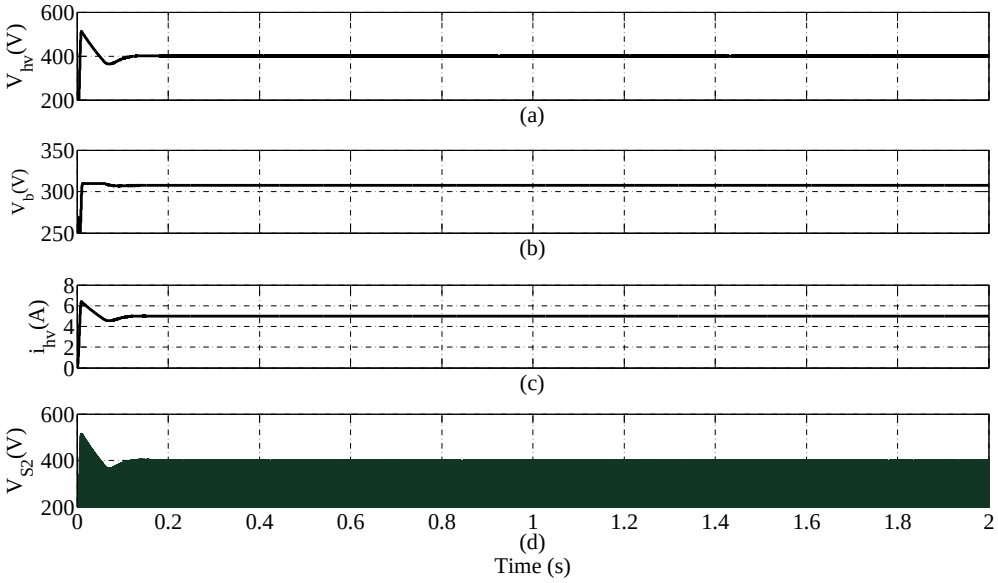

Fig. 3.7. Simulation waveforms of propulsion mode, (a) dc-link voltage, (b) battery voltage, (c) battery current, (d) voltage across S_2

and again increased to 2 kW at t = 2 s, the closed-loop controller regulates the dc-link voltage at 400 V, as shown in Fig. 3.8 (a). The corresponding change in the battery voltage, battery current and dc-link current are shown in Fig. 3.8(b), (c) and (d), respectively. The battery voltage is approximately constant even after load changes, as shown in Fig. 3.8(b). From Fig. 3.8, the measured battery and load currents at 2 kW are 6.8 A and 5 A respectively and hence the calculated efficiency of the converter at 2 kW is 95.8%.

Fig. 3.9 shows simulation waveforms during regenerative mode. The regenerative braking action is tested by linearly increasing the dc-link voltage from 350 V, t = 0 s to 390 V, t = 1 s and from t = 1-1.5 s, the dc-link voltage is kept constant at 390 V. From t = 1.5 s, the dc-link voltage linearly decreases to 370 V, as shown in Fig. 3.9(a). The battery current is regulated at 4 A irrespective of the dc-link voltage variations, as shown in Fig. 3.9(c) and the battery voltage is around 308 V, as shown in Fig. 3.9(b).

The converter efficiency curve for plug-in charging mode is shown in Fig. 3.10. It is seen from this curve, the efficiency at 0.5 kW (lower charging power) is 93% and increases to 94.6% at 3.2 kW then again decreases at higher charging power levels. The efficiency of this mode is relatively lower compared to propulsion and regenerative braking modes. Reason for

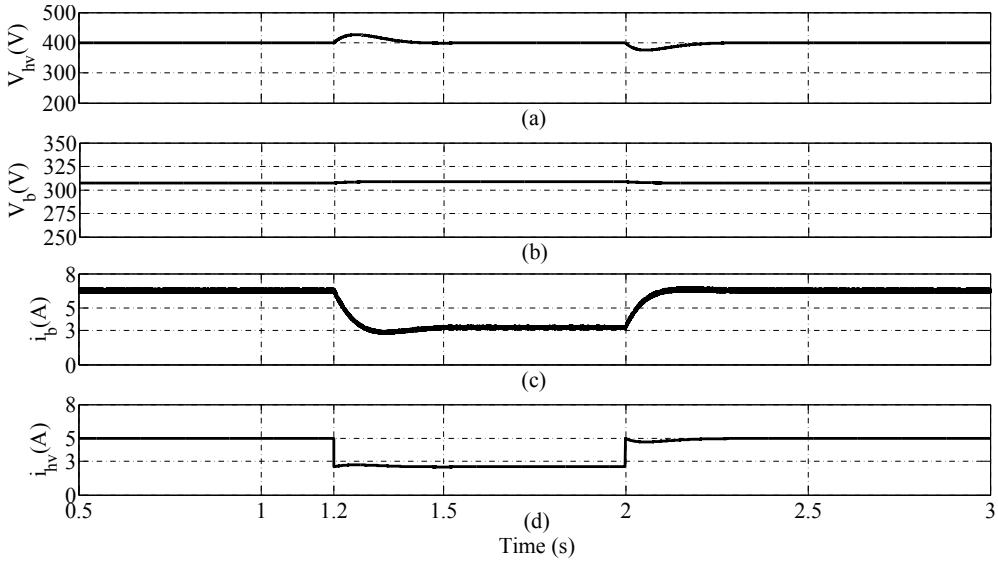

Fig. 3.8. Simulation waveforms of propulsion mode, (a) dc-link voltage, (b) battery voltage, (c) battery current, (d) dc-link current

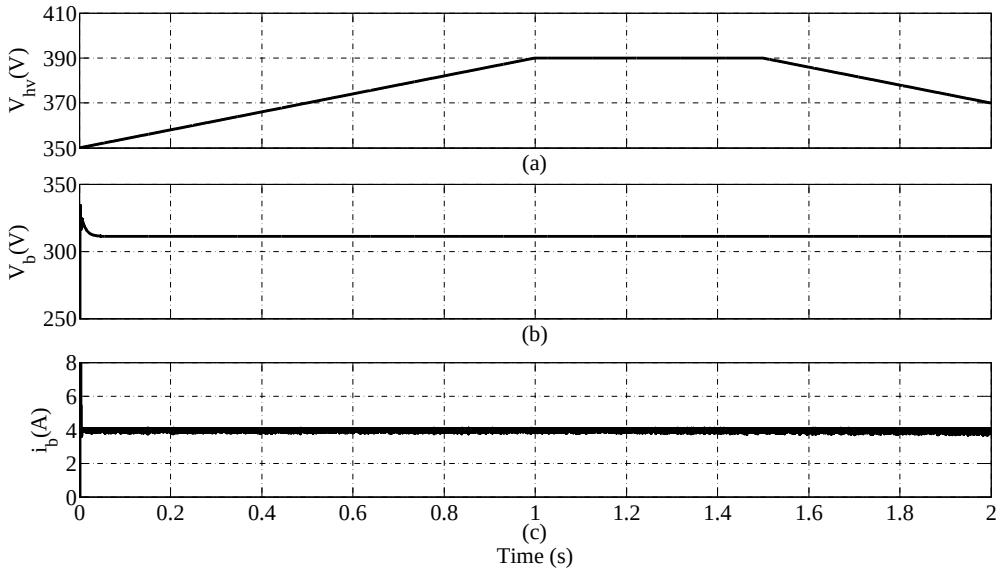

Fig. 3.9. Simulation waveforms of regenerative mode, (a) dc-link voltage, (b) battery voltage, (c) battery current

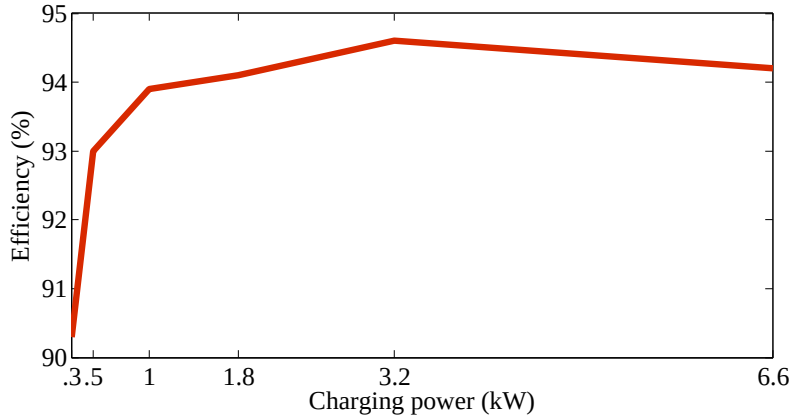

Fig. 3.10. Efficiency of the proposed converter in charging mode

lower efficiency in this mode has been analyzed in Section 3.4.

The proposed converter is also simulated at lower voltage and power levels to provide parity between simulation and experimental results. The simulation parameters at lower rating have been given in Table 3.6. Figs. 3.11 and 3.12 show waveforms of plug-in charging mode with 100 W charging power. 3.13 shows simulation waveforms of propulsion mode with step load changes as 100-70-100 W. Fig. 3.14 shows simulation waveforms of regenerative braking mode where the dc-link voltage is linearly increased from 50 V to 90 V and then kept constant at 90 V shown in Fig. 3.14(a). The battery is charged with 3 A of current, as shown in Fig.3.14(c).

A laboratory prototype has been developed for testing and validation of the proposed converter with 36 V battery and 60 V dc-link. The circuit parameters for experimental verification are listed in Table 3.7.

Fig. 3.15 shows waveforms for plug-in charging mode with 100 W charging power. In this Fig., the grid current at CH1 has sinusoidal shape as well as in phase with the grid voltage at CH2, which shows converter is operating at high power factor. The measured grid current is 2.52 A. Therefore, calculated power at grid side is 107 W and the efficiency of the converter is 93.4%. The recorded battery current and voltage are shown at CH3 and CH4, respectively. A low frequency oscillation in the battery current is seen at CH3 in Fig. 3.15 (a), the filter inductor at battery terminal suppresses the oscillation of the battery current.

Fig. 3.16 shows the waveforms of oscilloscope during propulsion mode with 60 V dc-

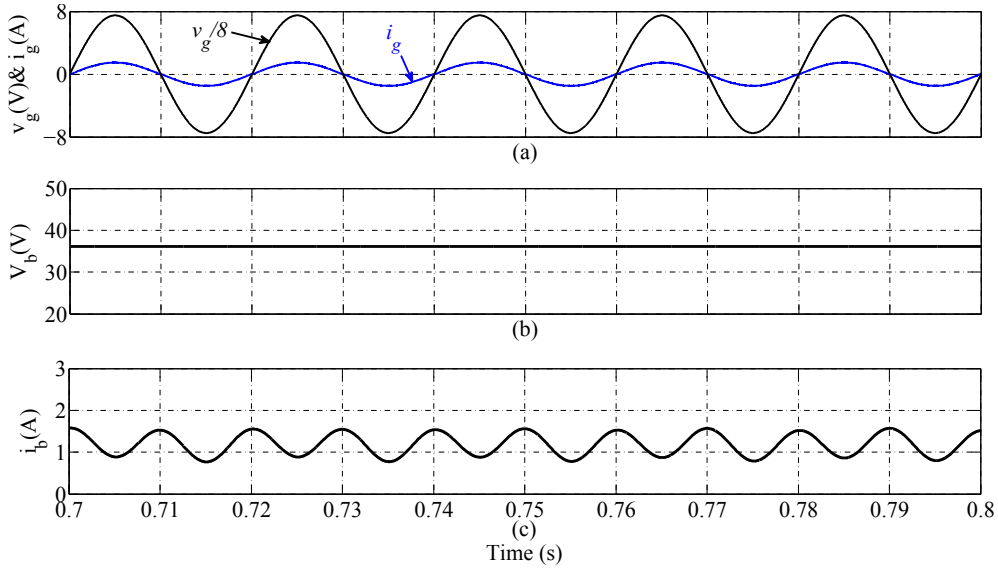

Fig. 3.11. Simulation waveforms of plug-in charging mode, (a) grid voltage and grid current, (b) battery voltage, (c) battery current

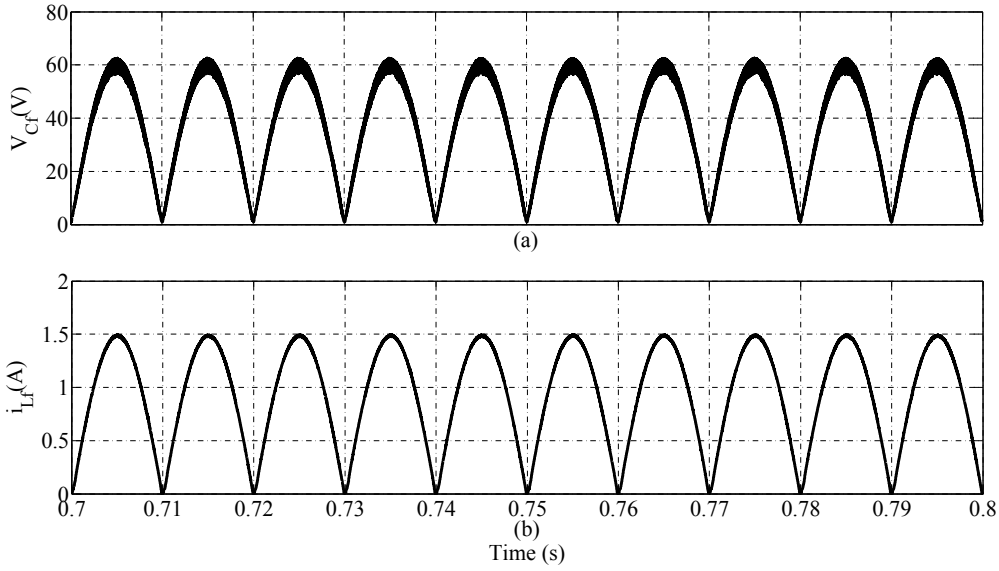

Fig. 3.12. Simulation waveforms of plug-in charging mode, (a) voltage across C_f, (b) current through L_f

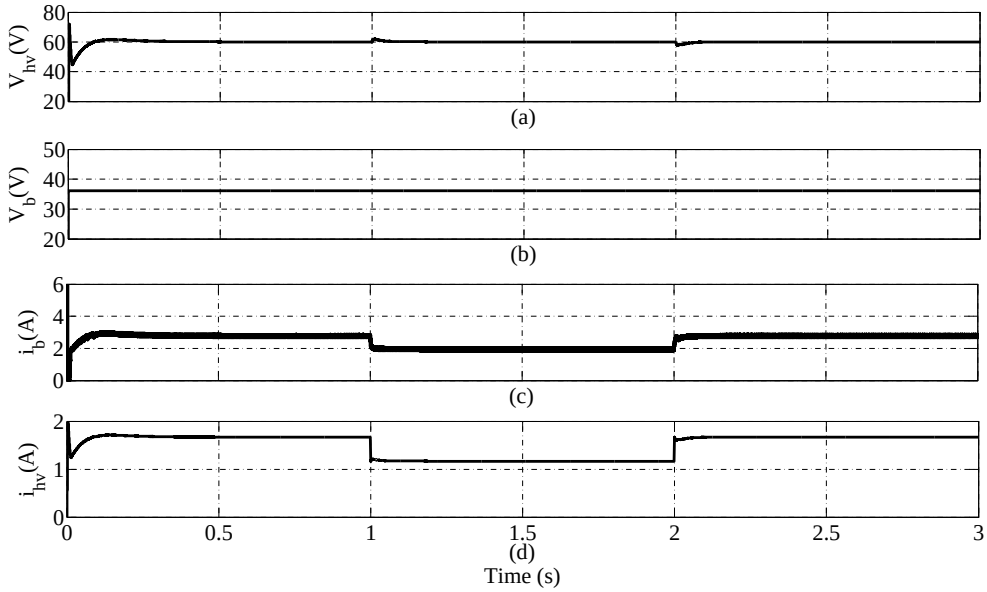

Fig. 3.13. Simulation waveforms of propulsion mode at lower voltage and power levels

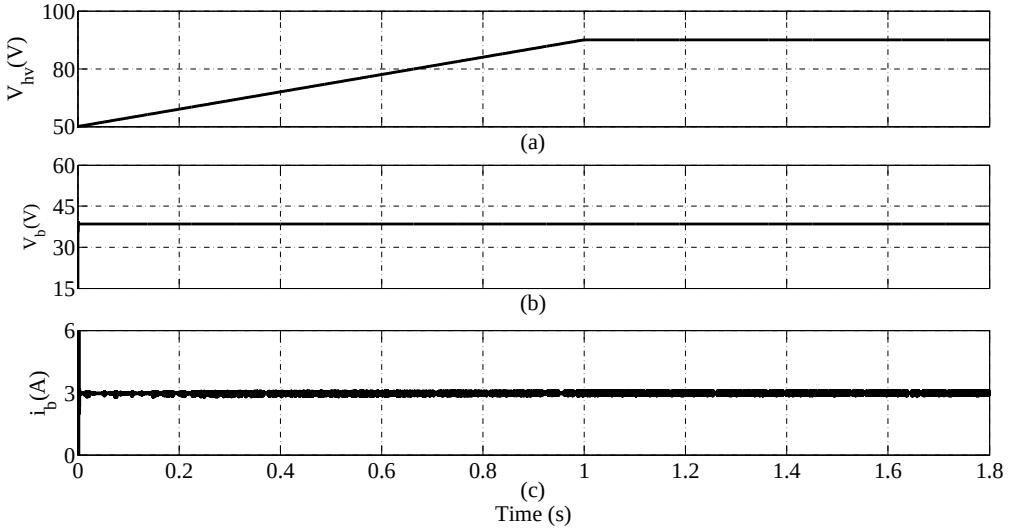

Fig. 3.14. Simulation waveforms of regenerative braking mode at lower voltage and power levels

Table 3.7. Experimental parameters

Parameters	Values
Grid voltage (v_g)	42.42 V
Charging power (P_b)	100 W
dc-link voltage (V_{hv})	*60 V*
Line frequency (f_L)	*50 Hz*
Nominal battery voltage (V_b)	*36 V*
Battery capacity	*26 Ah*
L_1/L_2	*3 mH*
$C_{hv}/C_M/\ C_b$	*550/10/2200 μF*

link and 100 W load where CH1, CH2 and CH3 denote battery current, dc-link voltage and battery voltage, respectively. The dynamic performance of this mode is tested with step load changes as 100-70-100 W and the closed-loop controller closely regulates the dc-link voltage at 60 V. The corresponding change in the battery current with the load is seen at CH1 in Fig. 3.17. The measured battery current with 100 W load is 2.89 A hence, calculated power at battery side is around 104.04 W; therefore, experimental efficiency at 100 W is 96.1%.

In the prototype model, regenerative braking mode is implemented by manually varying the dc-link voltage with the help of auto-transformer and bridge rectifier. The change in

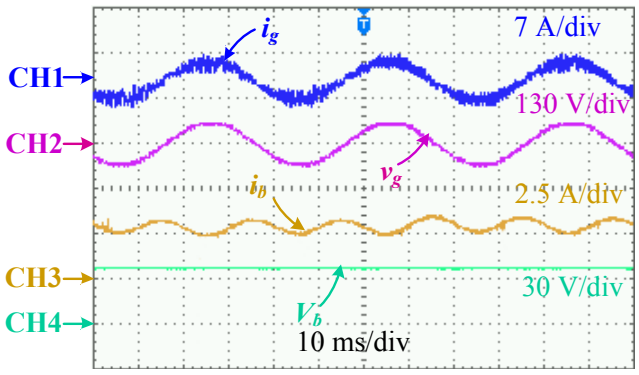

Fig. 3.15. Experimental results of plug-in charging mode (CH1: grid current, CH2: grid voltage, CH3: battery voltage and CH4: battery current)

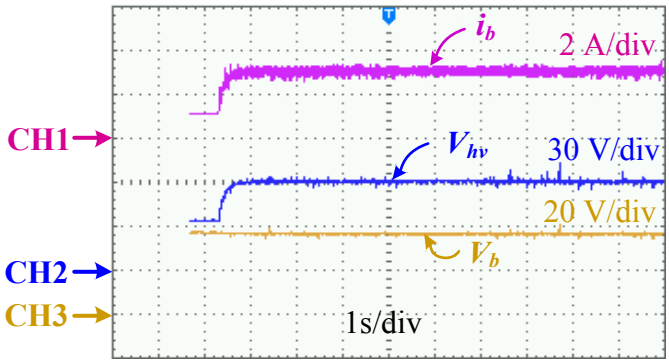

Fig. 3.16. Experimental results of propulsion mode with 100 W load (CH1: Battery current, CH2: dc-link voltage and CH3: battery voltage)

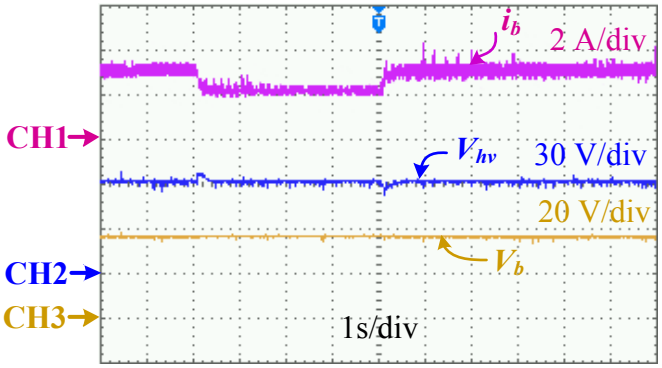

Fig. 3.17. Experimental waveforms of propulsion mode with step load change (CH1: Battery current, CH2: dc-link voltage and CH3: battery voltage)

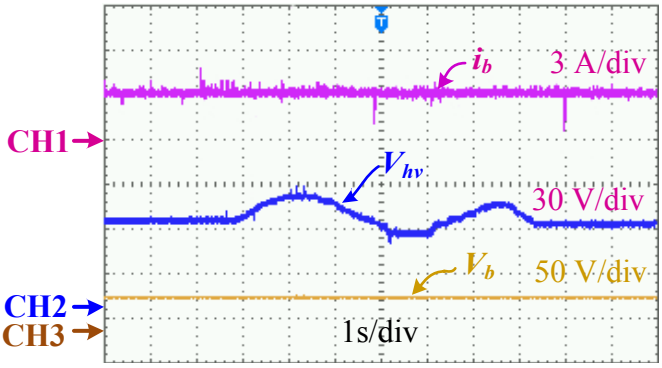

Fig. 3.18. Dynamic response of converter in regenerative mode (CH1: battery current, CH2: dc-link voltage and CH3: battery voltage)

the dc-link voltage represents speed variation of the motor during regeneration process. The motive here is to charge the battery through the braking energy. As the dc-link voltage is varied between 57-84 V, as shown in Fig. 3.18 at CH2, the reference charging current remains constant at 3 A as shown at CH1. The battery voltage is 36 V, as shown at CH3 in Fig. 3.18.

3.7 Conclusion

The proposed integrated converter in this Chapter operates as conventional ZETA converter with power factor correction for plug-in charging mode. While in propulsion and regenerative braking modes it operates as conventional boost and buck dc/dc converters, respectively. Also, there is no reversal of voltage polarity in any mode of converter operation. The voltage/current stresses analysis in ac/dc and dc/dc stages have been developed for selection of switches. Further, a loss analysis of the converter in ac/dc and dc/dc stages have been given to calculate the efficiency in each mode. The peak efficiency of plug-in charging mode is 94.6 %, and in propulsion and regenerative braking, are 97.2% and 98.1%, respectively. The operational capabilities and performance of the proposed integrated converter have been verified with simulation as well as experimental results. The performance of control algorithms in propulsion and regenerative braking modes are tested with step change of load and the dc-link voltage variations, respectively.

CHAPTER 4

SEPIC BASED INTEGRATED CONVERTER

4.1 Introduction

This chapter focuses on a new power electronic converter for PEVs which is capable of operation for all three modes. The proposed structure is derived from conventional SEPIC converter which operates as SEPIC PFC during plug-in charging mode, and as conventional boost and buck converter in propulsion and regenerative braking modes, respectively. Due to SEPIC operation in plug-in charging mode, the battery can be charged from the universal input voltage. Moreover, a nonlinear carrier control (NLCC) method is used in this converter for PFC, which eliminates voltage sensor requirement for CCM operation. The consequent reduction of feedback circuit enhances its compactness and makes it more suitable for OBC. Compared to ZETA derived integrated converters discussed in Chapters 2 and 3, this SEPIC based converter does not require a large passive filter on the grid side for PFC. Further, a rigorous stress and a loss analysis of the converter have been investigated for selection of semiconductor devices and to show the feasibility of the proposed converter.

4.2 Conventional SEPIC Converter

Fig. 4.1 shows conventional SEPIC converter for PFC operation. Similar to conventional ZETA PFC converter in Section 2.2 (Chapter 2), conventional SEPIC PFC converter can operate only in plug-in charging mode of PEVs. To operate conventional SEPIC in other modes of vehicle operation, some additional switches need to be employed, which is shown in Fig. 4.2.

4.3 Operation of the Proposed Integrated Converter

The proposed converter has two semiconductor switches, two mechanical switches (M_1 and M_2), one bridge diode rectifier, two inductors and three capacitors. Operating states of switches and diodes in each mode are shown in Table 4.1.

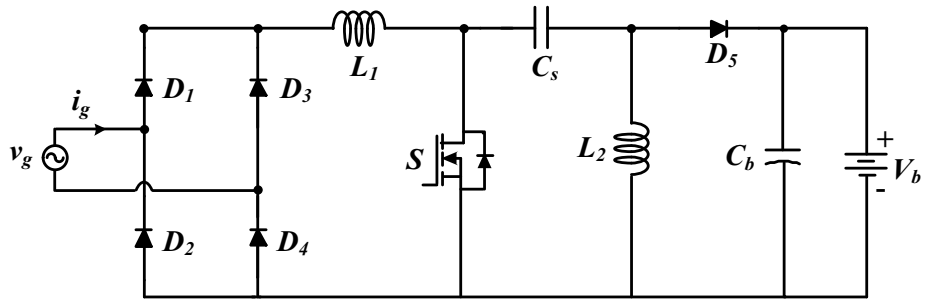

Fig. 4.1. Conventional SEPIC converter for PFC

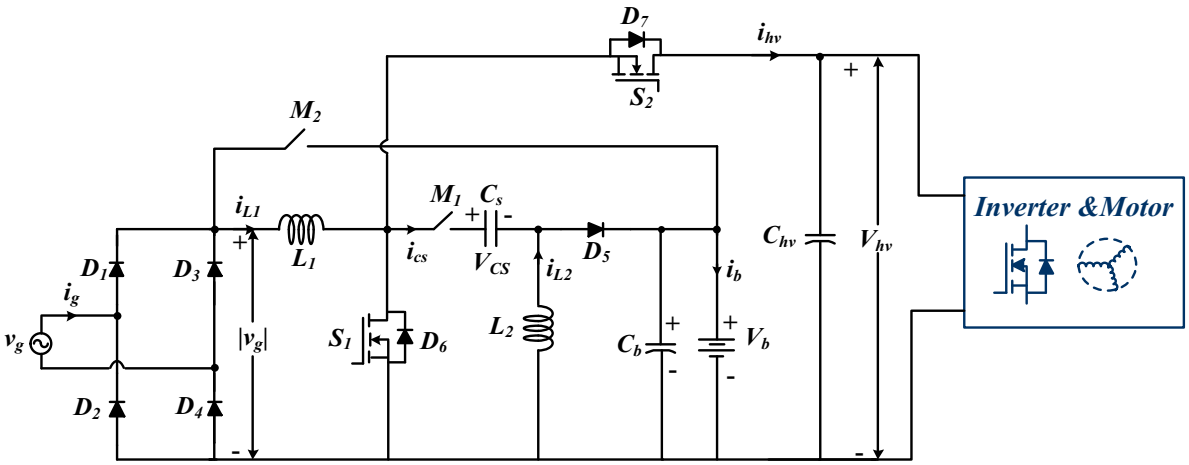

Fig. 4.2. Proposed power electronic interface with reduced feedback part

Table 4.1. States of the switching devices in each mode

Mode of operation	**Fig.**	**S_1**	**S_2**	**M_1**	**M_2**	**D_5**	**D_6**	**D_7**
Plug-in charging	Fig. 4.3(a)	PWM	OFF	ON	OFF	OFF	OFF	OFF
	Fig.4.3(b)	OFF	OFF	ON	OFF	ON	OFF	OFF
Propulsion	Fig. 4.4(a)	PWM	OFF	OFF	ON	OFF	OFF	OFF
	Fig. 4.4(b)	OFF	OFF	OFF	ON	OFF	OFF	ON
Regenerative braking	Fig. 4.5(a)	OFF	PWM	OFF	ON	OFF	OFF	OFF
	Fig. 4.5(b)	OFF	OFF	OFF	ON	OFF	ON	OFF

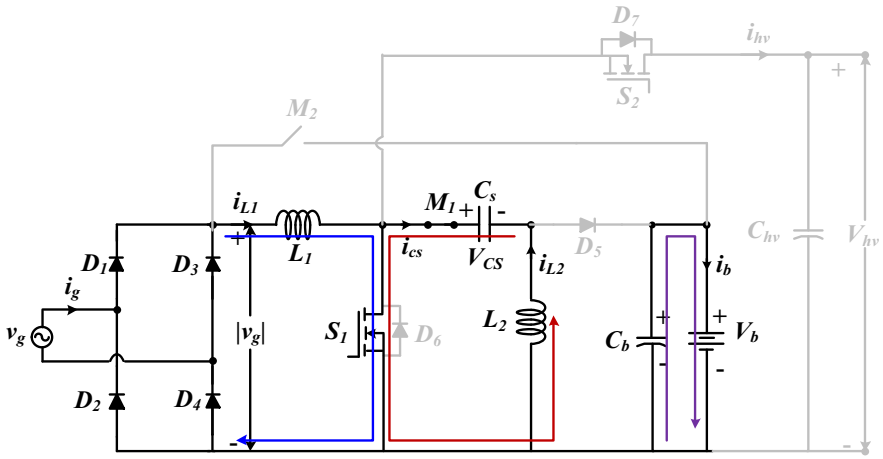

(a)

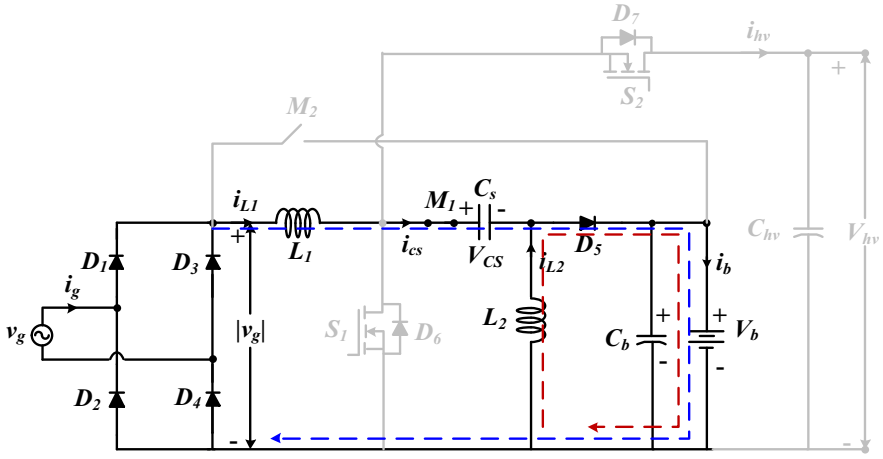

(b)

Fig. 4.3. Operation of the converter during plug-in charging mode, (a) S_1 is ON, (b) S_1 is OFF

4.3.1 Plug-in charging mode

In this mode, switches S_2 and M_2 are OFF, switch S_1 is PWM gated and switch M_1 is always ON. When switch S_1 is turned ON, inductor L_1 stores energy through the path $|v_g|$-L_1-S_1-$|v_g|$ while inductor L_2 is charged by capacitor C_s through path L_2-C_s-S_1-L_2, meanwhile, capacitor C_b provides energy to the battery, as shown in Fig. 4.3(a). When S_1 is turned OFF, inductor L_1 charges the capacitor C_s through the path $|v_g|$-L_1-C_s-D_5-v_b-$|v_g|$ and inductor L_2 supplies energy to the output stage, i.e., capacitor C_b and battery, as shown in Fig. 4.3(b). Moreover, capacitor C_{hv} is immediately charged to peak grid voltage($V_{g,max}$) through the

diode D_7 and then this diode remains OFF throughout the operation this mode.

Let us assume that the duty ratio of the switch S_1 is d_1. The volt-second balance of inductor L_1 and L_2 in switching period T_s is written as

$$v_g(t) * d_1(t) * T_s = V_b * (1 - d_1) * T_s \tag{4.1}$$

the above equation gives the voltage conversion ratio M_1 as

$$M_1 = \frac{V_b}{V_{g,max} \left|\sin \omega t\right|} = \frac{d_1(t)}{1 - d_1(t)} \tag{4.2}$$

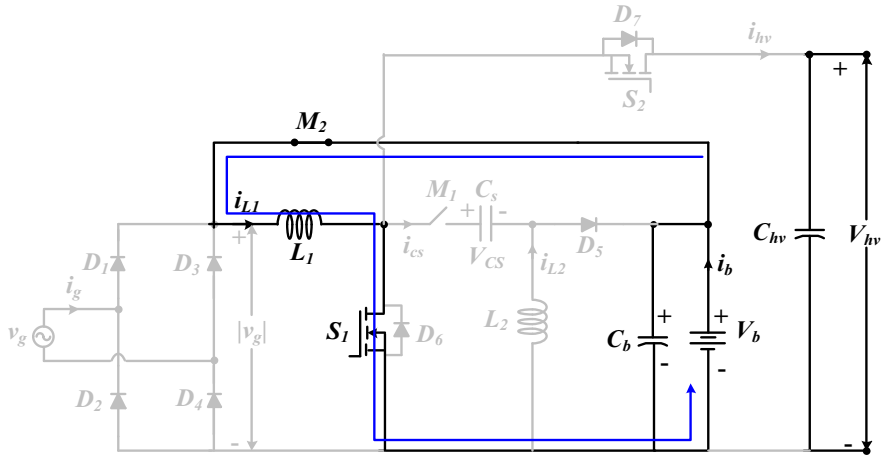

(a)

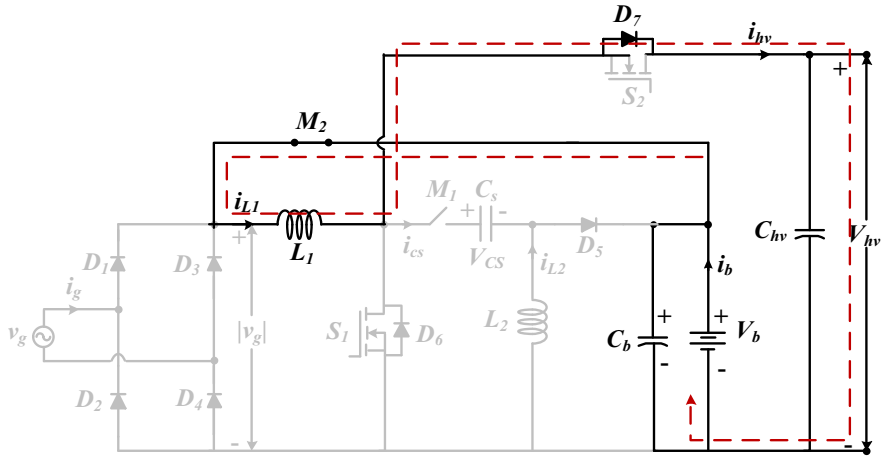

(b)

Fig. 4.4. Operation of the converter during propulsion mode, (a) S_2 and M_2 are always ON and S_1 is PWM turned ON, (b) S_1 is OFF

4.3.2 Propulsion mode

In this mode, switch M_2 is always ON, switches S_2 and M_1 are OFF and switch S_1 is operated with PWM signal. When switch S_1 is tuned ON inductor L_1 stores energy through the path, as shown in Fig. 4.4(a) and when S_1 is turned OFF, inductor L_1 releases its stored energy to the dc-link capacitor C_{hv} through the diode D_7 as shown in Fig. 4.4(b). Let us assume the duty ratio of switch S_1 in the propulsion mode is d_2. The volt-second balance of inductor L_1 in switching period T_s gives the voltage conversion ratio M_2 as

$$V_b * d_2 * T_s = (V_b - V_{hv}) * (1 - d_2) * T_s \tag{4.3}$$

$$M_2 = \frac{V_{hv}}{V_b} = \frac{1}{1 - d_2} \tag{4.4}$$

4.3.3 Regenerative braking mode

In this mode, the battery is charged by the electrical energy captured from conversion of mechanical energy stored in rotating parts of vehicle; therefore, this mode not only develops braking torque to stop the vehicle but also helps in efficient use of braking energy, leading to longer run of vehicle.

Switches S_1 and M_1 are always OFF during this mode, switch S_2 is operated through PWM signal and switch M_2 is kept in ON condition. By turning ON of S_2, inductor L_1 stores energy through the path shown in Fig. 4.5(a) and when S_2 is OFF, L_1 transfers its stored energy to the battery through the path shown in Fig. 4.5(b). The volt-second balance of inductor L_1 in switching period T_s gives the voltage conversion ratio M_3 as

$$(V_{hv} - V_b) * d_3 * T_s = V_b * (1 - d_3) * T_s \tag{4.5}$$

$$M_3 = \frac{V_b}{V_{hv}} = d_3 \tag{4.6}$$

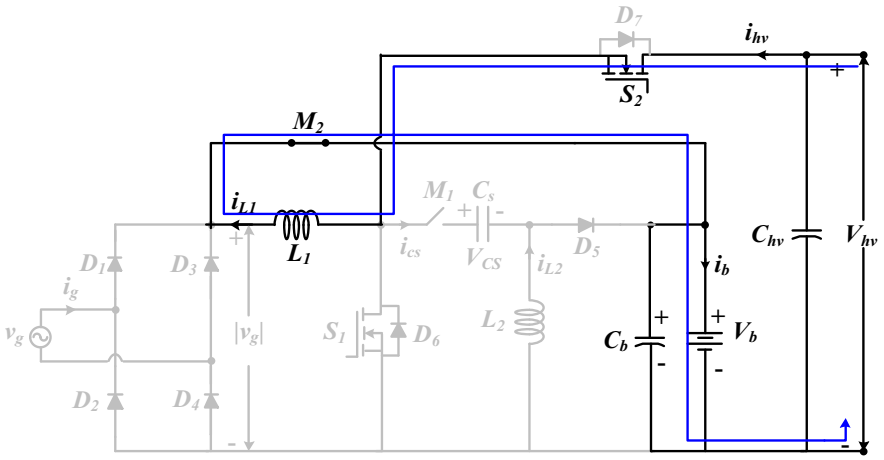

(a)

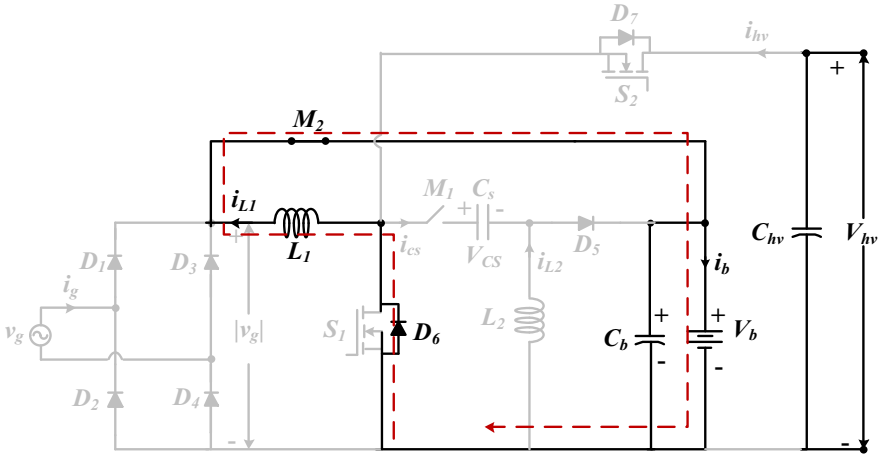

(b)

Fig. 4.5. Operation of the converter during regenerative braking mode, (a) M_2 is always ON and S_1 is PWM tuned ON, (b) S_2 is OFF

4.4 Components Selection and Loss Analysis

4.4.1 Components selection

Due to bidirectional operation of the proposed converter in dc/dc conversion stage, some of the switches and passive components are utilized for more than one mode; therefore, rating of a particular switch is selected based on maximum voltage/current stresses on the switch or its body diode during these modes of operation. It is assumed that voltage stress on body diode is the same as the switch voltage stress. Table 4.2 shows the peak voltage/current stresses on

Table 4.2. Peak voltage and current stresses on switching devices in each mode

Device	Plug-in charging		Propulsion		Regenerative braking	
	Voltage	Current	Voltage	Current	Voltage	Current
S_1	$[V_{g,max} + V_b]$	$[i_{g,max} + \langle i_{L2,grid}\rangle_{Ts} + \frac{\triangle i_{L2,grid}}{2}]$	V_b	$[\langle i_{L1,prop}\rangle_{Ts} + \frac{\triangle i_{L1,prop}}{2}]$	V_{hv}	NC
S_2	$2V_{g,max}$	NC	V_{hv}	NC	V_{hv}	$[\langle i_{L1,rege}\rangle_{Ts} + \frac{\triangle i_{L1,rege}}{2}]$
D_5	$[V_{g,max} + V_b]$	$[i_{g,max} + \langle i_{L2,grid}\rangle_{Ts} + \frac{\triangle i_{L2,grid}}{2}]$	V_b	NC	V_b	NC
M_1	NIL	$i_{g,max}$ max$(1, \frac{V_{g,max}}{V_b})$	V_b	NC	V_{hv}	NC
M_2	$\lvert V_{g,max} - V_b\rvert$	NC	NIL	$[\langle i_{L1,prop}\rangle_{Ts} + \frac{\triangle i_{L1,prop}}{2}]$	NIL	$[\langle i_{L1,rege}\rangle_{Ts} + \frac{\triangle i_{L1,rege}}{2}]$

where NC = Not conducting, NIL = 0 V, $i_{L1,prop}$ = inductor L_1 current in propulsion mode, $i_{L1,rege}$ = inductor L_1 current in regenerative braking mode, $i_{L2,grid}$ = inductor L_2 current in plug-in charging mode.

the switches and diode in each mode. From this Table switch ratings are selected as follows:

The switch S_1 conducts in plug-in charging and propulsion modes but peak voltage/current stresses on the switch S_1 in plug-in charging mode are sum of the input/output quantities (voltage/current). While in propulsion mode, peak voltage/current stresses are either input or output quantity (usually lower than plug-in charging mode); therefore, rating of S_1 is chosen based on plug-in charging mode. Similar to switch S_1, the rating of diode D_5 is also selected based on plug-in charging mode. Even though the switch S_2 operates only in regenerative braking mode but peak voltage developed across this switch is 2 $V_{g,max}$ in plug-in charging and V_{hv} in regenerative braking mode; thus, the voltage rating of S_2 is given as max (2 $V_{g,max}$ and V_{hv}), while the current rating of S_2 is decided by propulsion mode because body diode (D_7) of S_2 conducts in this mode, since the power level of propulsion mode is usually higher than other two modes. The peak voltage rating of switches M_1 and M_2 are $|V_{g,max}$-$V_b|$ and V_{hv}, respectively. The current rating of M_1 is decided on the basis of plug-in charging mode which is given as $i_{g,max}$*max $(1, \frac{V_{g,max}}{V_b})$. The current rating of M_2 is given as max $(\langle i_{L1,prop}\rangle_{Ts} + \frac{\triangle i_{L1,prop}}{2}, \langle i_{L1,rege}\rangle_{Ts} + \frac{\triangle i_{L1,rege}}{2})$.

4.4.2 Selection of passive components

In this Section, passive components design is discussed for CCM operation of the converter.

4.4.2.1 Selection of inductors L_1 and L_2

Since inductance L_1 is functional in all modes; the final selection of L_1 is based on its computation for each mode, and then determining largest of these values.

a) **Plug-in charging mode:**

The battery voltage V_b is given from (4.2) as

$$V_b = \frac{d_1(t)}{(1-d_1(t))}|v_g(t)| \tag{4.7}$$

where $d(t)$ is instantaneous duty ratio and $\mid v_g(t) \mid$=$V_{g,max} \mid sin(\omega t) \mid$ hence, duty ratio $d(t)$ is obtained as

$$d_1(t) = \frac{V_b}{V_b + \mid v_g(t) \mid} = \frac{V_b}{V_b + V_{g,max} \mid sin(\omega t) \mid} \tag{4.8}$$

The minimum value of inductor L_1 for allowable ripple current (η) is written as [92, 106, 107]

$$L_{1plug-in} = \frac{v_g(t)d_1(t)}{\eta i_g(t) f_s} = (\frac{V_g^2}{P_g})\frac{d(t)}{\eta f_s} = \frac{1}{\eta f_s}\left(\frac{V_g^2}{P_g}\right)\frac{V_b}{V_b + \mid V_g \mid} \tag{4.9}$$

b) **Propulsion mode:**

The minimum value of L_1 in propulsion mode for allowable ripple current (η') is given as [105–107]

$$L_{1prop} = \frac{V_b d_2}{\eta' f_s} \tag{4.10}$$

where d_2 is given in (4.4).

c) **Regenerative braking mode:**

The minimum value of L_1 in regenerative braking mode for allowable ripple current (η'') is given as [105, 106]

$$L_{1reg} = \frac{V_b(1-d_3)}{\eta'' f_s} \tag{4.11}$$

The final value of inductance L_1 is selected as

$$L_1 = max(L_{1plug-in}, L_{1pop}, L_{1reg}) \tag{4.12}$$

Inductor L_2 is utilized only in plug-in charging mode; therefore, selection of inductance value of L_2 should satisfy maximum allowable ripple η. Thus, the critical value of inductor is given as [105]

$$L_2 = \frac{V_b(1-d(t))}{\eta i_{L_2}(t) f_s} = \left(\frac{V_g^2}{P_g}\right)\frac{V_b}{\eta V_{g,max} f_s}\left(\frac{V_b}{V_b + V_{g,max}}\right) \tag{4.13}$$

4.4.2.2 Selection of capacitor C_s

The value of coupling capacitor,C_s to operate in CCM with allowable ripple voltage of k% is given as [92]

$$C_{ccm} = \frac{V_b d(t)}{k V_{cs}(t) f_s R_L} \tag{4.14}$$

by substituting $V_{cs}(t)$ = $|v_g(t)|$ and equivalent load resistance as $R_L = V_b^2/P_b$, and $d(t)$ in (4.14) and then rearranging terms gives

$$\begin{aligned} C_{ccm} &= \frac{V_b}{k|(v_g(t)|f_s\frac{V_b^2}{P_b}} \left(\frac{V_b(t)}{\mid v_g(t) \mid + V_b}\right) \\ &= \frac{P_b}{k f_s |(v_g(t)|(v_g(t) + V_b)} \end{aligned} \tag{4.15}$$

the maximum value of coupling capacitor is calculated at maximum ripple voltage of C, which occurs at maximum value of grid and battery voltages.

4.4.2.3 Selection of capacitor C_b

The value of capacitor C_b is given by as [92]

$$C_b = \frac{I_b}{2\omega \Delta V_b} = \frac{\frac{P_b}{V_b}}{2\omega\delta V_b} = \frac{P_b}{2\omega\delta V_b^2} \tag{4.16}$$

where δ is the tolerable ripple voltage in the battery capacitor C_b.

4.4.3 Loss analysis

In this Section, loss analysis of the proposed converter is investigated for each mode. A 1200 V/100 A switch is selected for this loss study. The current (RMS and average) expressions (Table 4.3) and data-sheet of switch are used for calculating semiconductor and passive components losses.

The conduction loss in a MOSFET switch, which is determined by on-state resistance is given as

$$P_{S,cond} = I_{s,rms}^2 * R_s(on) \tag{4.17}$$

On other hand, the conduction loss in an IGBT switch is determined by average current and voltage drop in saturation state and calculated as:

$$P_{S,cond} = \langle i_s \rangle_{Ts} * V_{CE_{sat}} \tag{4.18}$$

Table 4.3. RMS and average current stresses on switching devices and passive components in each mode.

Device	Plug-in charging		Propulsion		Regenerative braking	
	RMS	**Average**	**RMS**	**Average**	**RMS**	**Average**
S_1	$I_{g,RMS}\sqrt{1+\alpha\frac{8}{3\pi}}$	$I_{g,RMS}\frac{2\sqrt{2}}{\pi}$	$\sqrt{I_b^2 d_2 + \frac{d_2^3 V_b}{12 f_s^2 L_2^2}}$	$d_2 I_b$	NC	
S_2	NC		NC		$\sqrt{I_b^2 d_3 + \frac{d_3(1-d_3)^2 V_b^2}{12 f_s^2 L_2^2}}$	$d_3 I_{hv}$
D_5	$I_b\sqrt{\frac{3}{2}+\frac{16}{3\pi}\alpha}$	$\frac{I_{g,RMS}2\sqrt{2}}{\pi}\alpha$	NC		NC	
D_6	NC		NC		$\sqrt{I_b^2(1-d_3) + \frac{(1-d_3)^3 V_b^2}{12 f_s^2 L_2^2}}$	$I_b(1-d_3)$
D_7	NC		$\sqrt{I_b^2(1-d_2) + \frac{d_2(1-d_2)V_b^2}{12 f_s^2 L_2^2}}$	$I_b(1-d_2)$	NC	
M_1, C_s	$I_{g,RMS}\sqrt{\alpha\frac{8}{3\pi}}$	0	NC		NC	
M_2	NC		$\frac{2}{\sqrt{3}}I_b$	I_b	$\frac{2}{\sqrt{3}}I_b$	I_b
L_1	$I_{g,RMS}$	$I_{g,RMS}\frac{2\sqrt{2}}{\pi}$	$\frac{2}{\sqrt{3}}I_b$	I_b	$\frac{2}{\sqrt{3}}I_b$	I_b
L_2	$I_{g,RMS}\alpha\sqrt{\frac{3}{2}}$	$\frac{I_{g,RMS}}{2}\alpha$	NC			

where NC = Not conducting, $\alpha = \frac{V_{g,\max}}{V_b}$, I_{hv} = average dc-link current, I_b = average battery current and $I_{g,RMS}$ = grid RMS current.

Switching loss occurs due to the simultaneous presence of significant drain-source voltage in MOSFET (or collector emitter voltage in IGBT) and drain (or collector) current during each transient from turn OFF-state to turn ON- state, and from turn ON-state to turn OFF-state. The switching power loss can be approximately calculated as

$$P_{sw} = \frac{1}{2}\left(V_{s,\max} * I_{s,\max}\right) * (t_r + t_f) * f_s \tag{4.19}$$

where $V_{s,max}$ and $I_{s,max}$ are peak values of voltage and current and t_r, t_f are the rising and falling time of the switch. Power loss of diode is the sum of diode conduction loss (product of average current (I_F) and knee voltage (V_F)) and revers recovery loss, which is modeled as

$$P_D = V_F * I_F + P_{Qrr} \tag{4.20}$$

where P_{Qrr} is the reverse recovery loss of a diode. It can be neglected for fast recovery diode and lower switching frequency. The ohmic loss in mechanical switch is determined as

$$P_{M,cond} = I_{M,rms}^2 * r_M \tag{4.21}$$

Table 4.4. Parameters for loss calculation

Parameters	**Values**
Switch rating	1200 V/100 A
$V_{CE(sat)}$	2.45 V
Rise time (t_r)	65 ns
Fall time (t_f)	80 ns
Resistance of M_1 and M_2	0.05 Ω
Forward voltage of Body diode/Rectifier diode (V_{FD})	2.55/1.5 V
Resistance of L_1/L_2	110 mΩ

Table 4.5. Total losses of the proposed converter and conventional converters in ac/dc and dc/dc stages with V_b = 300 V and V_{hv} = 400 V

P_{ch}[kW]	P_{prop} [kW]	P_{reg}[kW]	V_{grid} [V]	Total losses in plug-in charging mode [W] (ac/dc stage)			Total losses in propulsion mode [W] (dc/dc stage)			Total losses in regenerative braking mode [W] (dc/dc stage)		
				Conventional SEPIC	Proposed SEPIC	Efficiency drop (%)	Conventional boost	Proposed boost	Efficiency drop (%)	Conventional buck	Proposed buck	Efficiency drop (%)
1.8	10	0.5	120	140.93	146.33	0.3	271.96	327.75	0.55	13.9	13.95	0.01
3.2	15	1	240	156.55	164.86	0.25	520	645	0.833	15.7	16.25	0.055
6.6	20	1.5	240	419.74	455	0.53	790.41	1011.88	1.1	21.75	22.5	0.055

The total semiconductors and mechanical switch losses P_S in any mode is modeled as

$$P_S = P_{S,cond} + P_{sw} + P_D + P_{M,cond} \tag{4.22}$$

The passive components that come in main current path are L_1, L_2 and capacitor C_s, then inductor copper loss is modeled as

$$P_L = I_{L,rms}^2 * r \tag{4.23}$$

where r is the resistance of inductors L_1 and L_2.

The ohmic loss in equivalent series resistance r_c of the capacitor C_s is expressed as

$$P_c = I_{c,rms}^2 * r_c \tag{4.24}$$

Table 4.6. Comparative study of the proposed integrated converter with single-stage converters

Charger topologies	Mode of operation			Number of components				
	Plug-in charging	Propulsion	Regenerative braking	Switch	Diode	Inductor	Capacitor	Sensor (voltage and current)
Boost PFC converter	Boost	Buck/boost	Buck/boost	5	5	2	2	5
Inverting Buck/boost PFC Converter	Buck/boost	Buck/boost	Buck/boost	5	5	2	2	5
SEPIC PFC converter	Buck/boost	Buck/boost	Buck/boost	5	5	3	3	5
CuK PFC converter	Buck/boost	Buck/boost	Buck/boost	5	5	3	3	5
Integrated converter [95]	Buck/boost	Buck/boost	Buck/boost	6	9	1	2	4
Integrated converter [98]	Boost	Buck/boost	Buck /boost	4	4	1	2	4
Integrated converter [99]	Boost	Boost	Buck	5	1	1	2	4
Proposed integrated converter	Buck/boost	Boost	Buck	2	5	2	3	4

Then total passive component losses P_P is written as

$$P_P = P_L(or P_{L1} + P_{L2}) + P_c \tag{4.25}$$

where P_{L1} and P_{L2} are the copper loss of L_1 and L_2, respectively.

The total losses (P_S+P_P) of the proposed converter and their conventional counterparts in each mode are given in Table 4.5 where P_{ch}, P_{prop} and P_{reg} denote power rating of plug-in charing, propulsion and regenerative braking modes, respectively.

In ac/dc stage, the proposed converter has an additional switch M_1 compared to conventional SEPIC converter. Due to that there is a slight efficiency drop (due to low resistance of M_1) in the proposed converter which varies between 0.25-0.53% for 1.8-6.6 kW charging power. In dc/dc stage of the proposed converter, switch M_2 is additional component in the current path compared to their conventional counterparts. In regenerative braking mode for power level in the range of 0.5-1.5 kW, efficiency drop is not significant (0.01-0.055%) due to negligible losses in M_2. Therefore, In propulsion mode for the power level in the range of 10-20 kW, the efficiency drop of the proposed converter is between 0.55-1.1%. Addition of mechanical switches do not contribute significant efficiency drop in each mode. Therefore,

the proposed converter has approximately same efficiency in each mode as compared to their conventional counterparts.

4.5 Comparative Analysis

The proposed converter is compared with conventional single-stage converters as well as with existing integrated converters. The proposed converter has the fewer number of components compared to all conventional converters, namely: boost, inverting buck/boost, SEPIC and Cuk PFC converters. It is also compared with existing integrated converters, as shown in Table 4.6. The integrated converter [95] requires an input passive filter for PFC in plug-in charging mode. In addition to this, presence of the large number of semiconductor devices in [95] it has lower efficiency in each mode compared to the proposed converter, as shown in Fig. 4.6. The converter [98] has higher efficiency in plug-in charging mode compared to the proposed converter due to its boost operation, as shown in Fig. 4.6(a). The integrated converter [99] has bridgeless nature in plug-in charging mode; therefore, this converter has the highest efficiency compared to the proposed converter as well as integrated converters. In dc/dc stage (propulsion and regenerative braking), the proposed converter has two devices (one semiconductor device one mechanical switch) in the current path while converters [98, 99] have two semiconductor devices; losses in mechanical switch is negligible compared to losses in semiconductor device. Therefore, efficiency of the proposed converter in dc/dc stage is higher in comparison with converters [98, 99], as shown in Fig. 4.6(b) and (c). The higher efficiency in the dc/dc stage leads to a longer run of vehicle.

4.6 Control Strategy

A generalized block diagram of the controller used for the proposed converter is shown in Fig. 4.7. Since the integrated converter has three operation modes and in each mode of operation different control strategies are adopted. Firstly, the mode selector logic decides the mode of operation, the reference quantity is determined for that mode. The prior knowledge of the reference quantity is necessary because input reference can be dc bus voltage, charging power or torque according to the mode of operation. Once operation mode and reference quantity are set, the concerned controller becomes active and ensures that controlled variable follows the reference value.

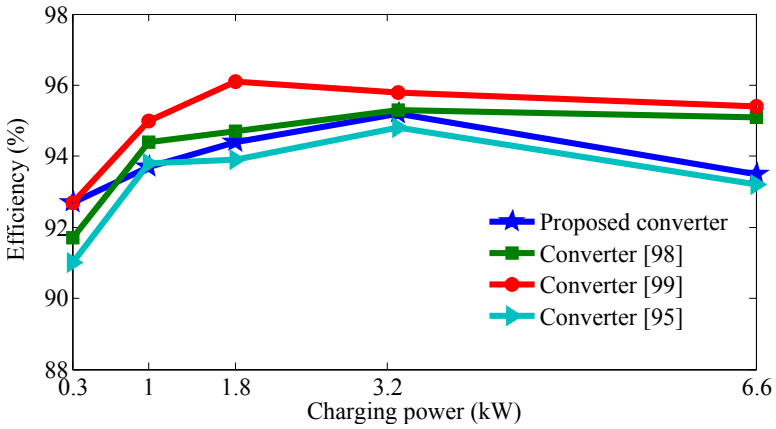

(a)

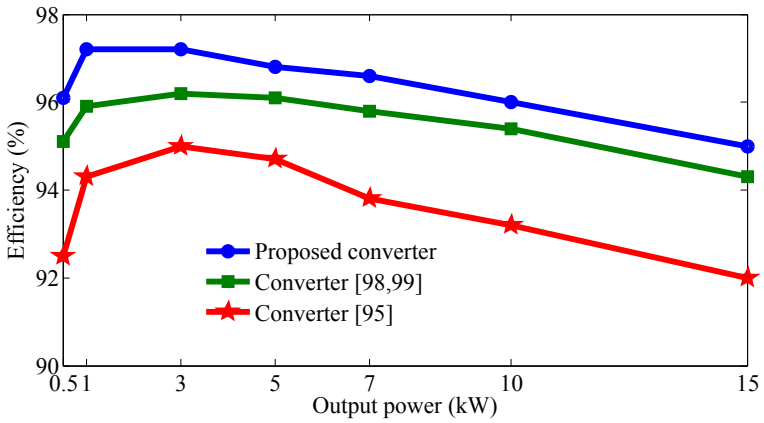

(b)

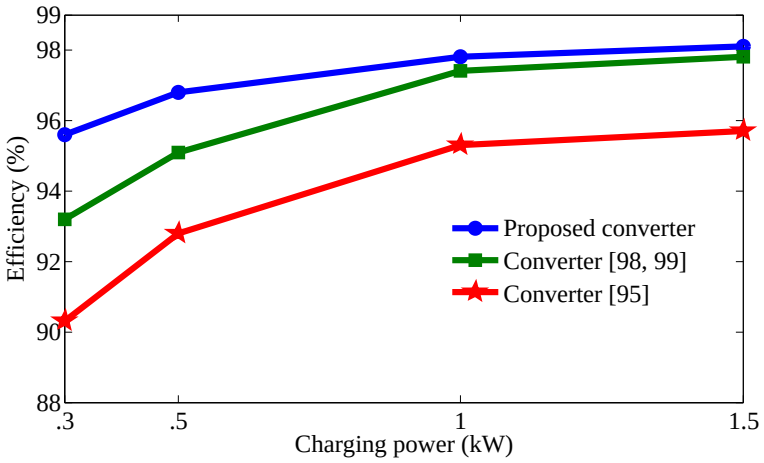

(c)

Fig. 4.6. Efficiency comparison, (a) plug-in charging mode, (b) propulsion mode, (c) regenerative braking mode

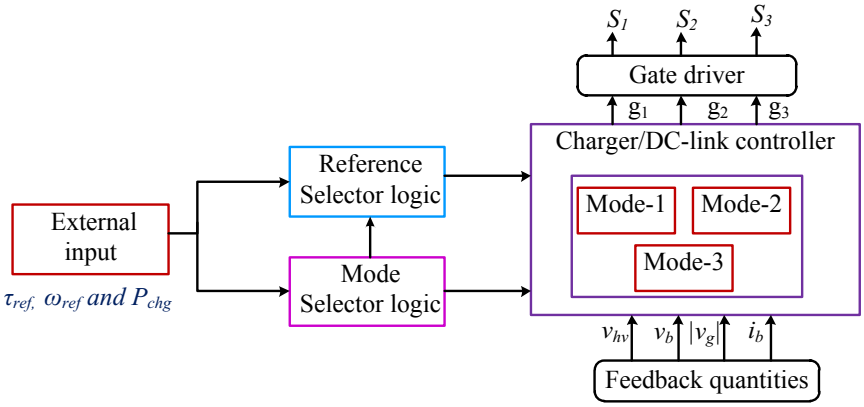

Fig. 4.7. General control diagram of the proposed integrated converter

4.6.1 PFC using nonlinear carrier control method

In previous research, various closed-loop control techniques have been proposed to actively shape input current waveform for high power factor (PF), including average current mode control [108], current programmed control [109], sliding-mode control [110], input voltage feed-forward, predictive control [111] and critical conduction mode control [112]. Usually, these control techniques require both voltage and current sensing circuits to perform PFC in CCM. The proposed converter uses a nonlinear carrier control (NLCC) method for PFC to reduce the feedback circuitry [113–115]. This control technique requires only one current sensor for PFC operation in CCM. The reduction of feedback circuitry reduces the volume of the charging system and enhances the compactness of the converter. In addition to this, cost of the charger is also reduced.

The basic concept behind the NLCC for PFC operation in CCM to generate a voltage signal proportional to the integral of switch current (current through S_1) to be compared with the reference voltage signal v_c to generate required duty signal as shown in Fig. 4.8(b). The switch is turned ON at the beginning of switching period. Meanwhile, integral of i_{s1} is calculated using operational amplifier based integrator which converts it into voltage signal v_i which is then multiplied by a negative unit signal to nullify the inversion of v_i due to operational amplifier. When -v_i becomes equal to v_c, the switch is turned OFF. Further, it is desirable to control the integral of this current, for two reasons: (1) integral of the waveforms improves noise immunity, and (2) the integral of the waveform is directly related to its average

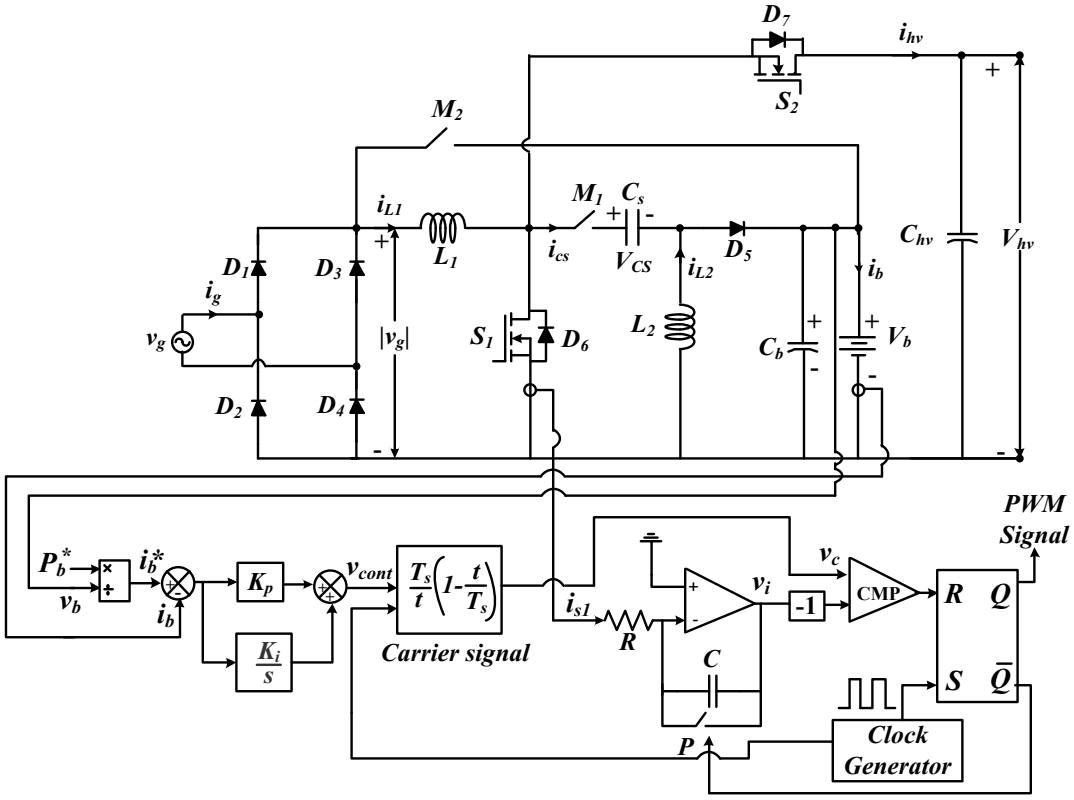

(a)

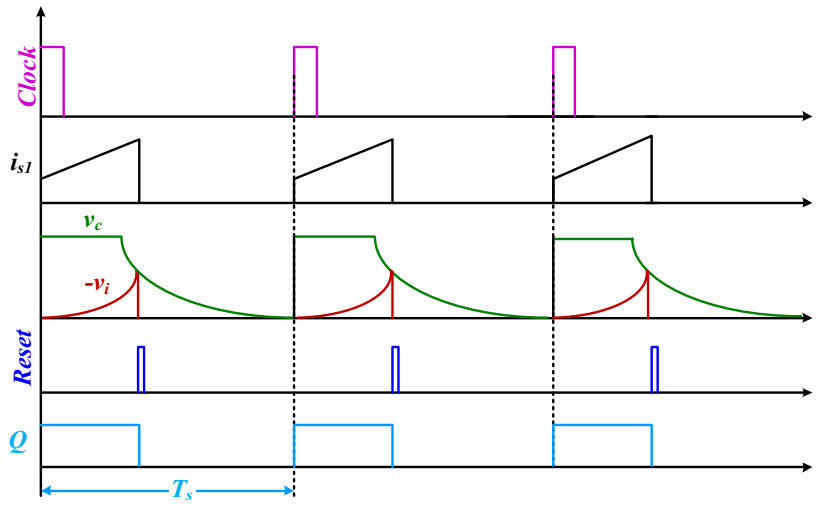

(b)

Fig. 4.8. (a) Control strategy of plug-in charging mode and (b) its operation waveforms

value,

$$v_i(t) = -\frac{1}{RC}\int_0^{d_1T_s} i_{s1}(\tau)d\tau \qquad 0 < t < d_1T_s \tag{4.26}$$

The integrator voltage $v_i(t)$ must be reset to zero at the end of each switching period, and the integration process begins afresh at the beginning of next switching cycle. When the switch is turned-"off", the voltage $v_i(d_1T_s)$ which is proportional to the average switch current, is given as:

$$v_i(d_1T_s) = -\frac{\langle i_{s1}\rangle_{T_s}}{RCf_s} \qquad 0 < t < T_s \tag{4.27}$$

To control the average switch current, it is desirable to obtain the average grid current by emulating it as input resistance current, given as follows :

$$\langle i_g(t)\rangle_{T_s} = \frac{\langle v_g(t)\rangle_{T_s}}{R_e\left(v_{cont}\right)} \tag{4.28}$$

Further to avoid sensing of $v_g(t)$ and $i_g(t)$, these quantities are computed from sensed feedback variables V_b and i_{s1}, which can be written as:

$$\langle i_{s1}(t)\rangle_{T_s} = d_1(t)\langle i_g(t) + i_b(t)\rangle_{T_s} \tag{4.29}$$

which yields

$$\langle i_{s1}\rangle_{T_s} = \langle i_g(t)\rangle_{T_s} \tag{4.30}$$

and

$$\langle v_g(t)\rangle = \frac{1 - d_1(t)}{d_1(t)}V_b \tag{4.31}$$

Using (4.28), (4.29) and (4.30), we get:

$$\langle i_{s1}(t)\rangle_{T_s} = \frac{\left[1 - d_1(t)\right]V_b}{d_1(t)R_e(v_{cont})} \tag{4.32}$$

By replacing $d_1(t)$ with t/T_s, the average current of switch can be controlled with control voltage through nonlinear carrier waveform as follows:

$$v_c(t) = v_{cont}(t)\frac{T_s}{t}\left(1 - \frac{t}{T_s}\right) \qquad 0 < t < T_s \tag{4.33}$$

This nonlinear reference voltage is valid between $0 < t < T_s$ and should be set to zero at the end of the switching period, such that $v_c(t + T_s) = v_c(t)$, as shown in Fig. 4.8(a). From Fig. 4.8(a), the outer closed-loop controls the charging power and sets the amplitude for NLC waveform. The reference waveform given by (4.33) is compared with the integral of switch current to generate PWM signal to be applied to switch S_1 through its gate driver circuit.

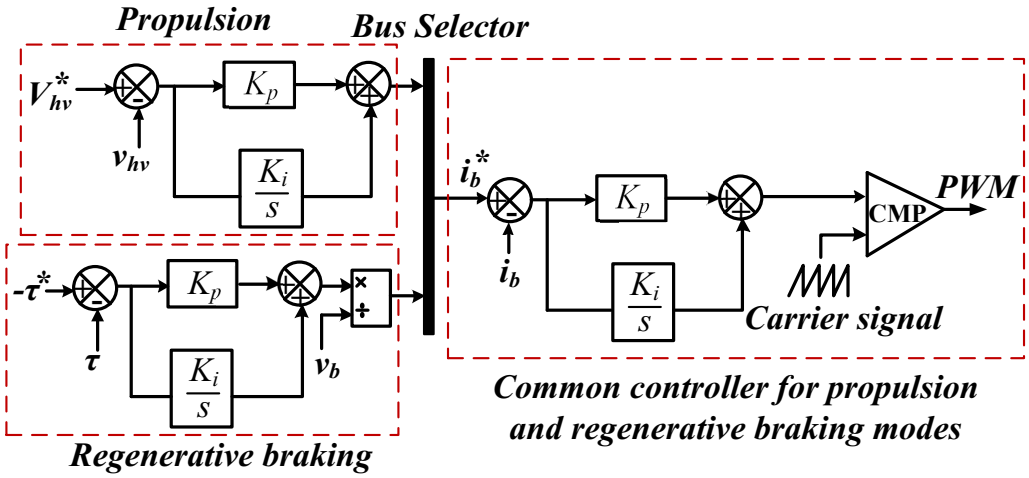

Fig. 4.9. Control block diagram of the converter in propulsion and regenerative braking modes

4.6.2 Propulsion and regenerative braking modes

The controller details for propulsion and regenerative braking modes is shown in Fig. 4.9. In both modes, two loop controllers are used to generate PWM pulses for respective switches. The inner proportional integral (PI) controller is common for both modes. The control target of propulsion mode is to keep the dc-link voltage at a desired value for smooth operation of inverter fed motor drive. The reference dc-link voltage is compared with the measured dc-link voltage and error is fed to the outer PI controller which generate a reference battery current for inner PI controller. The output of inner PI controller compared with triangular wave and generates PWM pulse for switch S_1.

In regenerative braking mode usually, the input reference quantity is torque or speed which is set manually by the operator. The error between reference and measured quantities is fed to outer PI controller to reference charging power (P_b) which is divided by instantaneous battery voltage (V_b) to generate a reference battery current for common PI controller. The parameters of these controllers have been tuned by trial and error method.

Table 4.7. Simulation parameters

Parameters	Values
Grid voltage (V_g)	*220/70.7 V*
dc-link voltage (V_{hv})	*400/60 V*
Nominal charging power (P_b)	*1.5 kW/120 W*
Line frequency (f_L)	*50Hz*
Nominal battery voltage (V_b)	*300/38 V*
L_1/L_2	*2 mH*
C_{hv}/C_M/C_b	*330/1/2200μF*

4.7 Results and Discussion

4.7.1 Simulation results

The different modes of operation of the proposed converter has been simulated in MATLAB/Simulink environment with sampling time of 1 μs. The list of parameters used in simulation is given in Table 4.7.

During Plug-in charging mode, the proposed converter operates as SEPIC converter and battery draws power from the grid. This mode is also known as PFC mode because converter operates in UPF condition to reduce the burden on supply system. From Fig. 4.10(a), grid voltage (v_g) and grid current (i_g) have desired wave-shape as well as in phase with each other which shows the effectiveness of the closed loop operation. The measured RMS grid current is 7.2 A at 220 V grid voltage with 1.5 kW charging power, the calculated power at grid side is 1.584 kW. Hence, the efficiency of the converter is found as 94.6%. Further, in SEPIC converter, the voltage across intermediate capacitor C_s is same as rectified grid voltage, i.e., $|v_g|$ shown in Fig. 4.10(b) and denoted as V_{cs}. The battery current has low frequency (100 Hz) oscillation (Fig. 4.10(d)) which is inherent in single-stage charging system. The amplitude of low frequency oscillation can be controlled by introducing an inductor filter in series with the battery. Its size is determined on the based on allowable low frequency ripple current and overall charger size. The battery voltage is around 308 V with 20% SOC as shown in

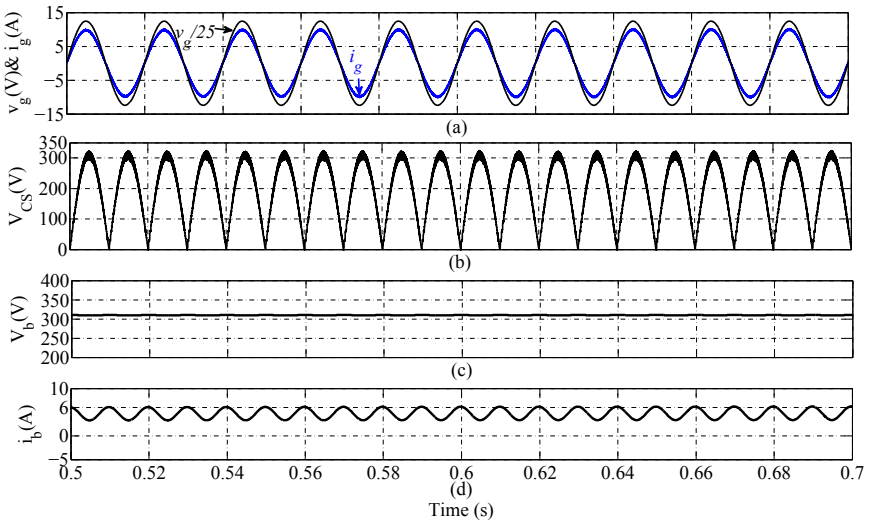

Fig. 4.10. Simulation waveforms of plug-in charging mode with 220 V grid voltage, (a) grid voltage and current, (b) voltage across capacitor C_s, (c) battery voltage, (d) battery current

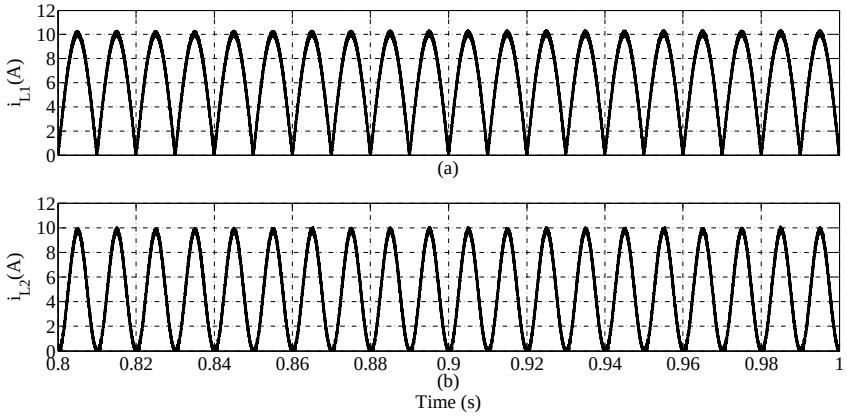

Fig. 4.11. Simulation waveforms of inductor currents, (a) current through L_1, (b) current through L_2

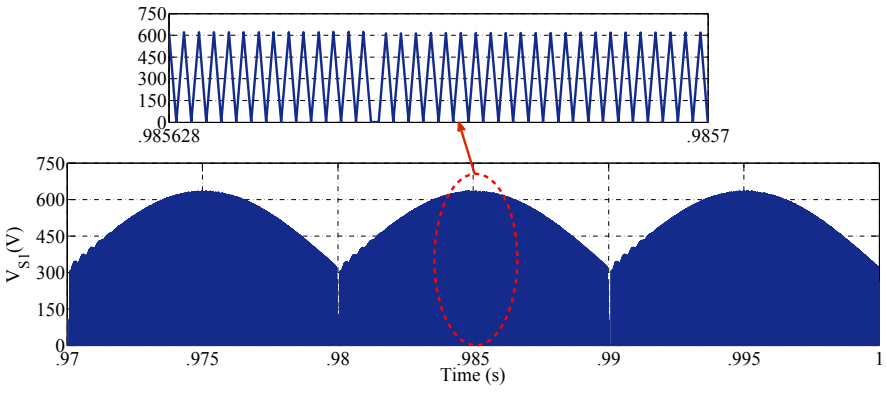

Fig. 4.12. Simulation waveforms of switch voltage (S_1)

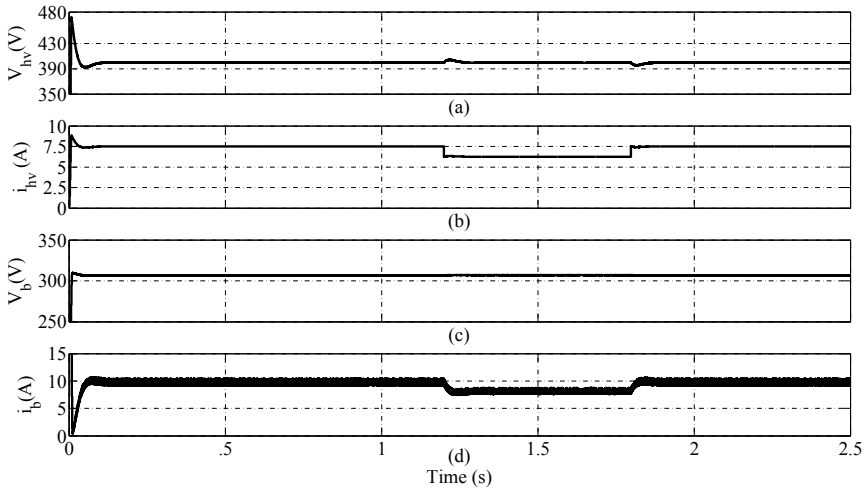

Fig. 4.13. Simulation waveforms of propulsion mode with dynamic operation

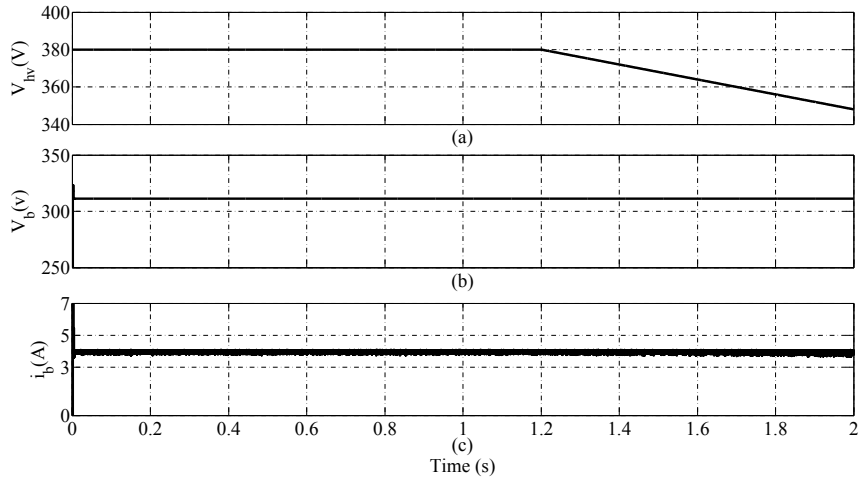

Fig. 4.14. Simulation waveforms of regenerative braking with dc-link voltage variation

Fig. 4.10(c). The inductor current waveforms i_{L1} and i_{L2} are shown in Fig. 4.11 (a) and (b), respectively. Current waveforms of L_1 and L_2 are similar to the rectified sinusoidal shape but magnitude of current through L_1 and L_2 depends on input voltage/power and output voltage/power, respectively. The peak voltages of input and output side are close to each other; therefore, peak current through L_1 and L_2 are approximately same. The peak voltage across switch S_1 is around 620 V (sum of input and output voltages), as shown in Fig. 4.12. The propulsion mode is characterized as battery discharging mode. The relevant waveforms of the converter during this mode are shown in Fig. 4.13. For stable operation of the inverter-drive system, it is necessary to keep the dc-link voltage constant. To examine the performance

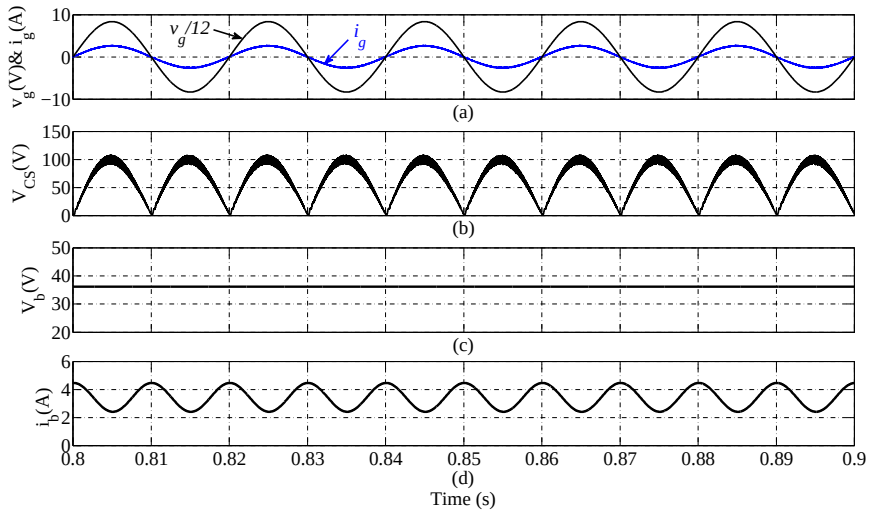

Fig. 4.15. Simulation waveforms of plug-in charging mode with 100 V (peak grid voltage), (a) grid voltage and current, (b) voltage across intermediate capacitor C_s, (c) battery voltage, (d) battery current

of closed loop operation of this mode, the step load changes from 3-2.5 kW at t = 1.2 s and 2.5-3 kW at t = 1.8 s have been applied and the dc-link voltage is regulated at 400 V, as shown in Fig. 4.13(a) which indicates the effectiveness of the controllers under dynamic conditions. From Fig. 4.13(b), the dc-link current is seen to vary between 6.5 to 7.5 A during the step change in load. The average battery current is 8.41 A and 10.1 A for the load 3 kW and 2.5 kW respectively, as shown in Fig. 4.13(d). The calculated battery side power for 2.5 kW and 3 kW load are 2.587 kW and 3.1108 kW hence, the efficiency for 2.5 kW and 3 kW are 96.6% and 96.4%, respectively.

The waveforms during regenerative braking operation are shown in Fig. 4.14. Unlike plug-in charging, in this mode, the battery is charged with braking energy of the motor and usually, converter operates in buck mode to capture braking energy. The dc-link voltage varies due to variation of motor speed and consequent generated electromotive force (EMF), which is proportional to the speed of motor. The developed voltage across motor terminals is rectified by inverter body diodes which appears as dc-link voltage across capacitor C_{hv}. The dc-link voltage is kept 380 V for t= 0-1.2 s then reduced to 345 V, as shown in 4.14(a). The battery voltage and the battery current are shown in Fig. 4.14(b) and (c), respectively. The battery is charged with constant current of 4 A, which is shown in Fig. 4.14(c).

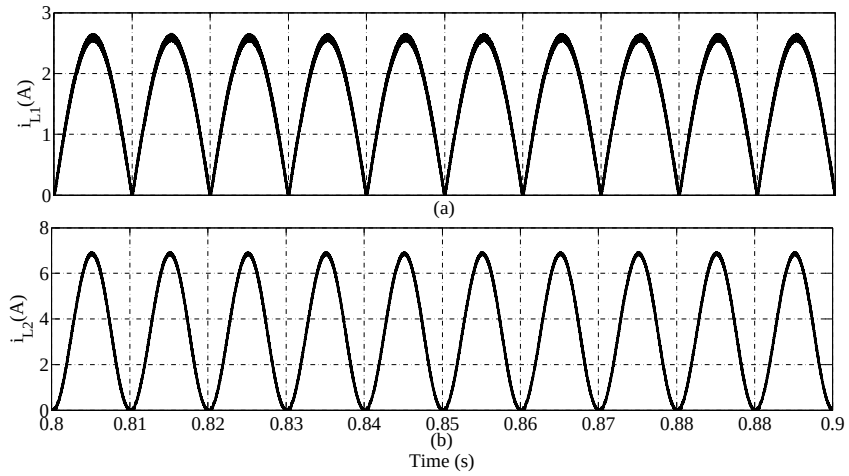

Fig. 4.16. Simulation waveforms of inductor currents in plug-in charging mode, (a) current through L_1, (b) current through L_2

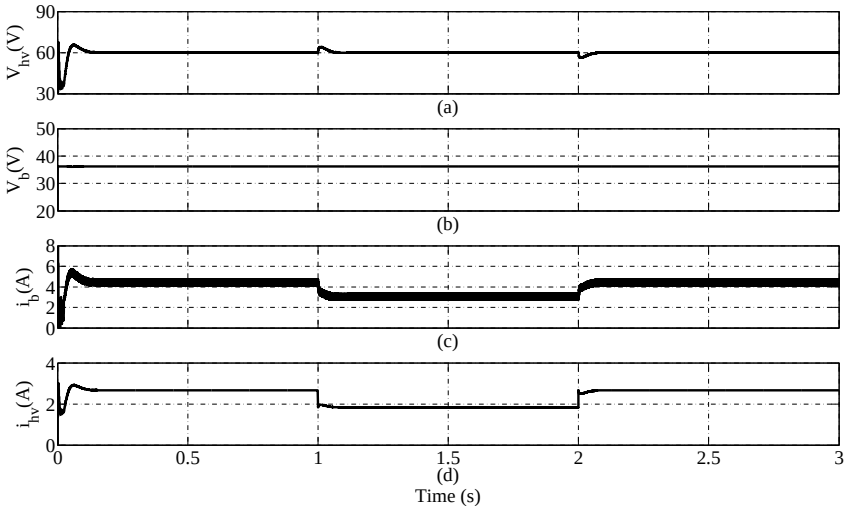

Fig. 4.17. Dynamic performance of propulsion mode with 60 V dc-link, (a) dc-link voltage, (b) dc-link current, (b) battery voltage, (d) battery current

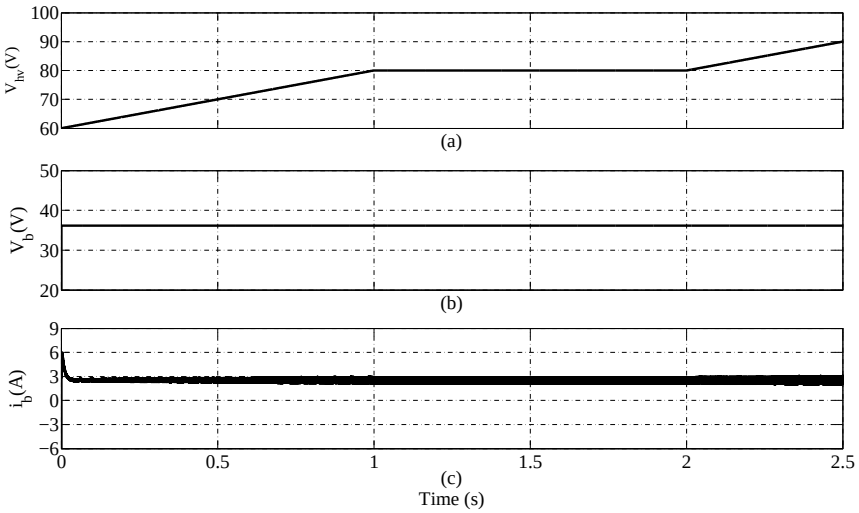

Fig. 4.18. Simulation waveforms in regenerative braking mode with varying dc-link voltage, (a) dc-link voltage, (b) battery voltage, (c) battery current

Furthermore, a scaled down simulation is also performed to provide parity between simulation and experimental results using 36 V battery (initial SOC = 20%), 100 V grid (peak) and 60 V dc-link with same passive components values.

Figs. 4.15 and 4.16 show simulated waveforms of plug-in charging mode using 120 W power. It is seen from Fig. 4.15(a), the grid voltage and current are in same phase with sinusoidal shape. The measured THD in the grid current and PF at grid side using FFT tool of MATLAB/Simulink are 2.93% and 0.990, respectively. The measured RMS value of i_g is 1.8 A and calculated power at grid side is 127.26 W; thus, efficiency is determined as 94.3% at 120 W charging power. Moreover, voltage across intermediate capacitor C_s, battery voltage and battery current are also shown in Fig. 4.15(b), (c) and (d), respectively. The voltage developed across capacitor C_S is same as the rectified grid voltage ($|v_g|$), as shown in Fig. 4.15(b). Current through inductors L_1 and L_2 is shown in Fig. 4.16.

The simulated waveforms of propulsion mode are shown in Fig. 4.17 with load changes from 160-110 W and 110-160 W at t = 1 s and 2 s, respectively. The dc-link voltage is regulated at 60 V with load changes.

The regenerative braking mode is tested by varying the dc-link voltage from 60 V to 90 V, as shown in Fig. 4.18. The dc-link voltage is linearly increased from 60 V, t = 0 s to 80 V, t = 1 s and kept constant at 80 V between t = 1 to 2 s thereafter, the dc-link voltage increases

Table 4.8. Experimental circuit parameters

Parameters	Values
Grid voltage (v_g)	*70.7 V*
dc-link voltage (V_{hv})	*80 V*
Line frequency (f_L)	*50Hz*
Battery voltage (V_b)	*36 V*
Battery capacity	*26 Ah*
L_1/L_2	*3 mH*
C_{hv}/C_M/ C_b	*330/1/2200 μF*

till 90 V, t = 2.5 s. The battery is charged with 3 A current, irrespective of the dc-link voltage variation.

4.7.2 Experimental results

The experimental waveforms of plug-in charging mode are shown in Figs.4.19 and 4.20. In this mode, the grid voltage and charging power, P_b are taken as 70.7 V and 120 W, respectively. Fig. 4.19(a), the v_g (CH1) and i_g (CH2) have sinusoidal shape and in phase with each other which indicates converter is operating under high PF condition. The measured RMS value of grid current is 1.83 A; therefore, calculated input power is 129.3 W at 120 W charging power then converter efficiency is found as 92.7%. The battery voltage and current are shown at CH3 and CH4, respectively. The battery current has oscillating nature similar to simulated result, which is an indication for agreement between simulation and hardware results. The power quality parameters are shown in Fig. 4.19(b). The waveforms of voltage across series capacitor C_s and current through inductor L_1 are shown in Fig. 4.20 at CH1 and CH2, respectively. The voltage across C_s, i.e., V_{CS} follows the rectified grid voltage $|v_g|$. Fig.4.21 shows waveforms of control signals. The current through switch S_1 is shown at CH1 in Fig. 4.21 and integral of this current generates a parabolic signal, v_i then it is inverted by multiplying with negative unit signal as -v_i which is compared with nonlinear reference carrier signal, v_c. Whenever, v_c is greater than -v_i, it generates PWM pulses for S_1. The v_c is clamped at a constant value to prevent it from approaching an infinite value at the beginning

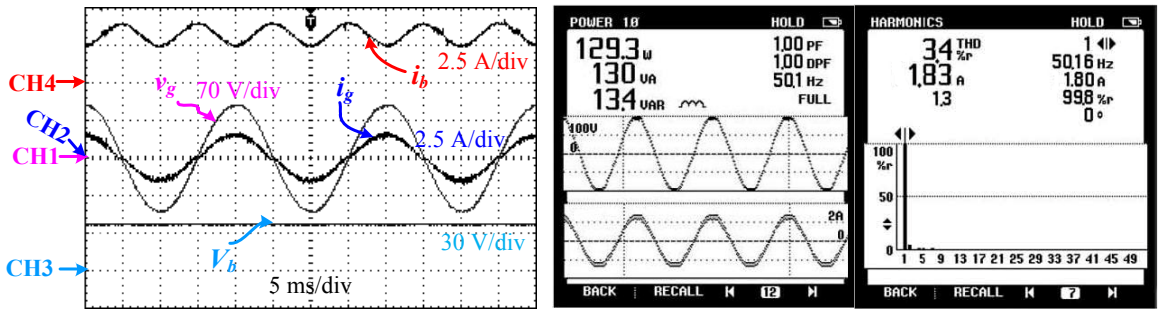

(a) (b)

Fig. 4.19. (a) Experimental waveforms during plug-in charging mode (CH1: grid voltage, CH2: grid current, CH3: battery voltage and CH4: battery current), (b) Power quality parameters

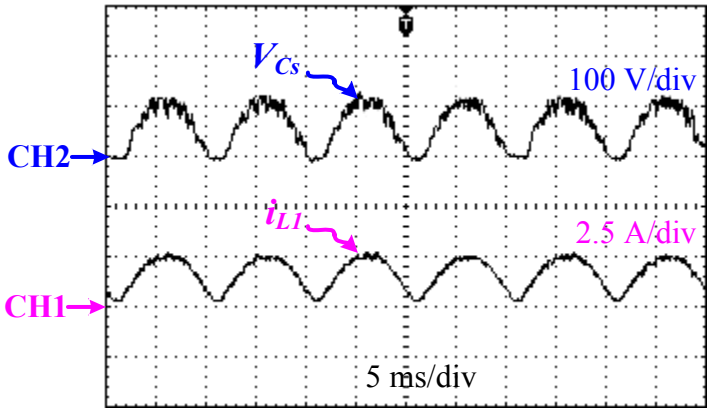

Fig. 4.20. Experimental Waveforms of voltage across capacitor C_s and current through inductor L_1 (CH1: V_{cs} and CH2: i_{L1})

of switching period.

In propulsion mode, the battery feeds power to the load through the inverter by boosting the battery voltage to the dc-link voltage level. For satisfactory operation of the vehicle system, the dc-link voltage is kept constant through the closed loop control system. Fig. 4.22(a) shows waveforms of this mode with 80 V dc-link and 160 W load where CH1, CH2, CH3 and CH4 denotes dc-link voltage, battery voltage, dc-link current and battery current, respectively. The effectiveness of the controller is tested with step load variations from 160-110 W and from 110-160 W meanwhile, the dc-link voltage is well regulated at 80 V, as shown in Fig. 4.22. The measured battery current at 160 W power is around 4.7 A; therefore,

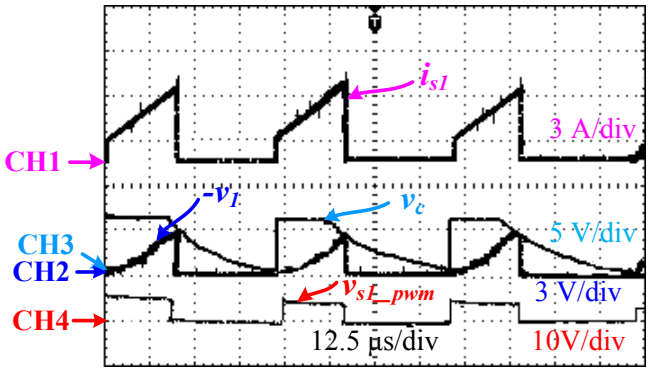

Fig. 4.21. Control signal waveforms

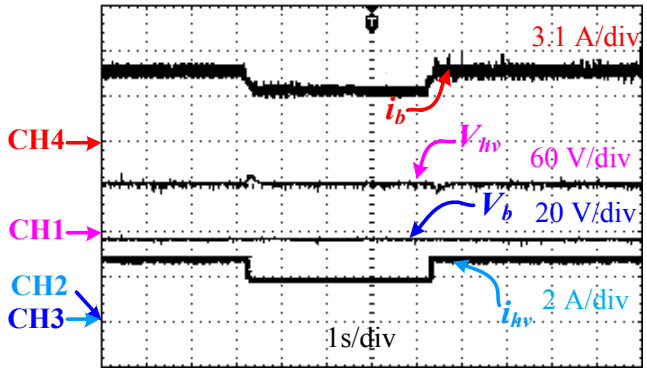

Fig. 4.22. Experimental waveforms of propulsion with step load change (CH1: dc-link voltage, CH2: battery current, CH3: dc-link current and CH4: battery current)

the battery side power is calculated as 169.2 W and hence, efficiency of the converter in this mode is found as 94.5%.

In regenerative braking mode, braking energy of the motor is used to charge the battery which leads to a long run of vehicle per charging. In hardware, this mode is implemented by manually varying the dc-link voltage with help of auto-transformer and a bridge rectifier. The battery is charged through 3 A of current irrespective of the dc-link voltage variation whereas battery side voltage is constant at 36 V. The output load is constant by regulating the battery current, the battery voltage is regulated as well. In constant load applications either voltage or current regulation is same as power regulation; therefore, the dc-link current i_{hv} increases when the dc-link voltage decreases and vice-versa, as shown in Fig. 4.23.

The experimental efficiency curves of the proposed converter in each mode are drawn through Fluk Power Analyzer shown in Fig. 4.24. The efficiency of the converter in plug-

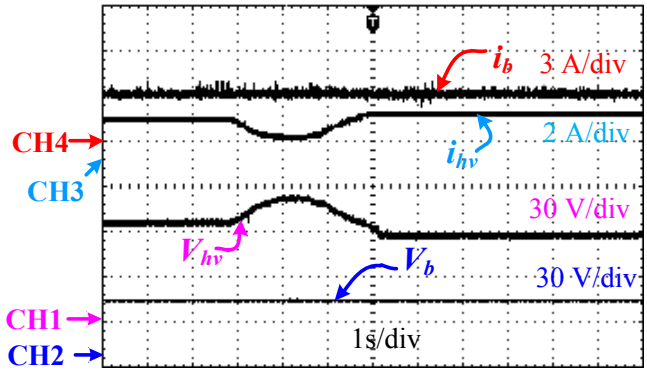

Fig. 4.23. Experimental waveforms of regenerative braking mode (CH1: dc-link voltage , CH2: battery voltage, CH3: dc-link current and CH4: battery current)

in charging mode varies between 90-94% for 80-220 W charging power. The efficiency of the converter in propulsion and regenerative braking modes are between 92.5-95.7% which is higher around 1.5% compared to plug-in charging efficiency, it is because in plug-in charging mode high stresses on semiconductor devices (higher losses) and losses of rectifier diodes result in lower efficiency.

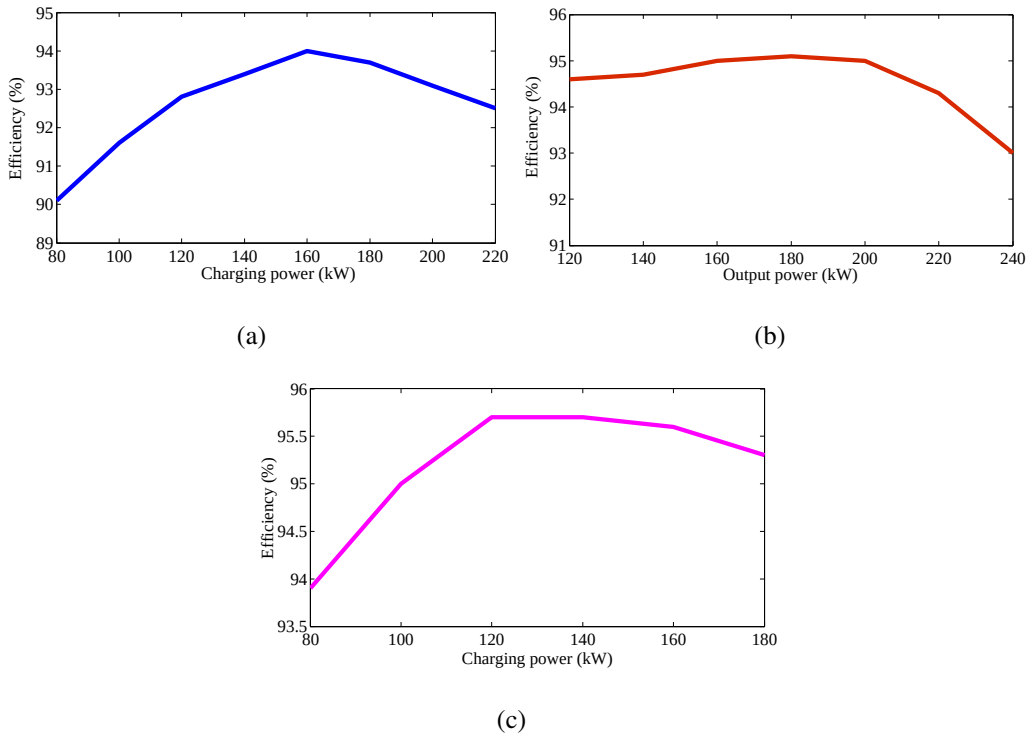

Fig. 4.24. Experimental efficiency, (a) plug-in charging mode, (b) propulsion mode, (c) regenerative braking mode

4.8 Conclusion

In this chapter, a new power electronic interface has been proposed with reduced feedback circuity. In plug-in charging mode, a nonlinear carrier based control strategy has been used for PFC in CCM which requires only current feedback to correct the power factor. Reduction of feedback element increases the compactness of converter and makes more suitable for OBC applications. Moreover, with this control scheme both high power factor (PF)[0.99] and low THD (below 5%) are obtained in the experimental and simulation results. A loss analysis of the proposed converter for ac/dc and dc/dc stages has been investigated and compared to their conventional counterparts to examine the amount of additional losses and drop in efficiency. The experimental results are found to be in agreement with simulation results, which validates the effectiveness of the proposed converter.

CHAPTER 5

INTEGRATED CONVERTER WITH REDUCED CONDUCTION LOSSES

5.1 Introduction

In the integrated converter topologies discussed in previous chapters, the focus has been laid on reduction of components, buck/boost operation in each mode and device voltage/current stresses. In a quest for further improvement, this chapter focuses on a new integrated converter which is derived from conventional two-switch buck/boost (TSBuB) converter (Fig.5.1), as shown in Fig. 5.2(a). The proposed converter has the peak efficiency improvement of 2-2.5% in propulsion boost and regenerative braking buck modes over existing integrated converter [98]. The proposed converter has two inductors and the size of second inductor is approximately reduced by more than 25% compared to single inductor converter [98]. The operation of converter and design procedure of passive components are discussed for each mode. Moreover, a loss comparison of the proposed converter with integrated converter [98] has been investigated in propulsion boost and regenerative buck modes. Simulation and experimental results are presented to validate the proposed converter.

5.2 Conventional Two-Switch Buck/Boost Converter

A conventional two-switch buck/boost (TSBuB) converter [101] is shown in Fig. 5.1. As compared to single-switch buck/boost converter (SEPIC, Cuk, ZETA, etc.), the TSBuB con-

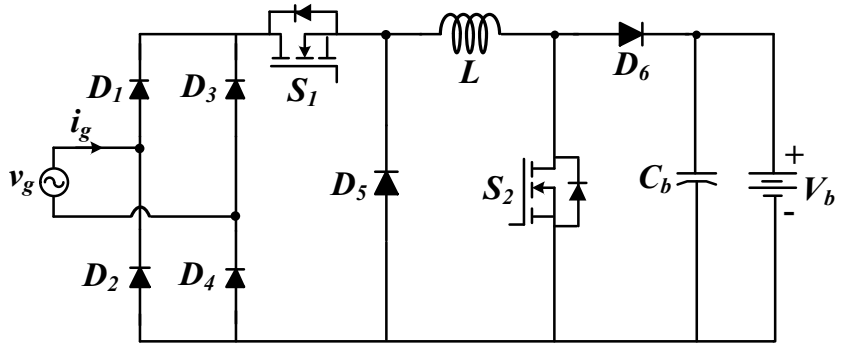

Fig. 5.1. Conventional two-switch buck/boost (TSBuB) converter.

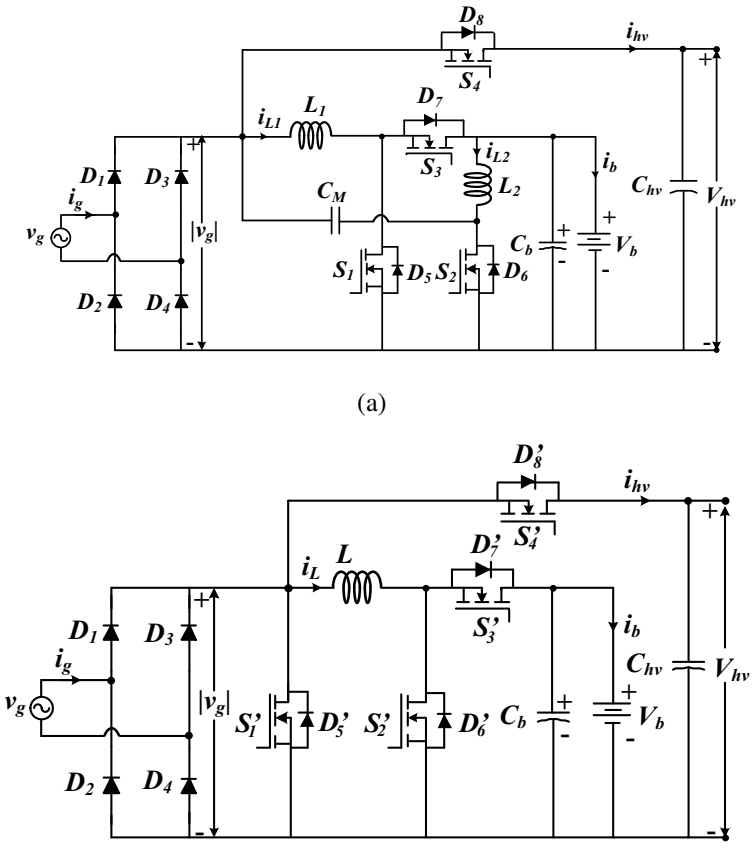

Fig. 5.2. (a) Proposed integrated converter, (b) Integrated converter [98]

verter has low stress on semiconductor devices, which makes it more suitable for high power applications with improved efficiency. The proposed integrated converter (Fig. 5.2(a)) is compared with integrated converter shown in Fig. 5.2(b) because this converter is closest to the proposed converter in terms of number of components and stress in semiconductor devices.

5.3 Operation of the Proposed Integrated Converter

The proposed integrated converter has three modes of operation: plug-in charging, propulsion (discharging of the battery), and regenerative operation (charging of the battery through braking energy). In the following Sections, the operation of the proposed integrated converter has been discussed in detailed manner. The states of switches for each mode are given in Table 5.1 .

Table 5.1. The states of switches of the proposed converter in each mode

Operation mode	Fig.	S_1	S_2	S_3	S_4
Plug-in charging	5.3	PWM	OFF	OFF	OFF
Propulsion boost	5.4(a)	OFF	PWM	ON	OFF
Propulsion buck	5.4(b)	OFF	OFF	PWM	OFF
Regenerative braking boost	5.5(a)	PWM	OFF	OFF	ON
Regenerative braking buck	5.5(b)	OFF	OFF	OFF	PWM

5.3.1 Plug-in charging mode

In this mode, when switch S_1 is turned ON, inductor L_1 stores energy through the path $|v_g|$-L_1-S_1-$|v_g|$, as shown in Fig. 5.3, meanwhile capacitor connected parallel to the battery supplies energy to the battery. When S_1 is turned OFF, current through L_1 follows the path $|v_g|$-L_1-D_7-V_b-$|v_g|$, and inductor L_1 transfers its stored energy to the battery. While L_2 and C_M form low-frequency filter between input and output, and voltage across C_M is the difference of the rectified grid voltage and the battery voltage, i.e., $|v_g| - V_b$. Let us assume that the duty ratio of the switch S_1 is d_1. The volt-second balance equation of inductor L_1 in switching period T_s can be written as:

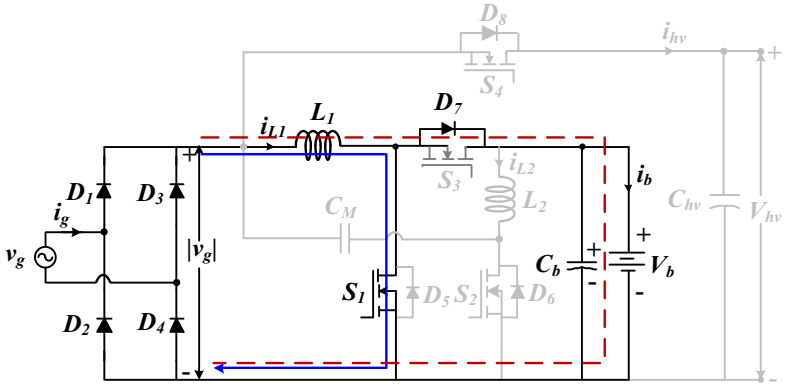

Fig. 5.3. Operation of the proposed integrated converter during plug-in charging mode

$$(V_{g,max}\,|\sin\omega t|) * d_1(t)T_s = (V_b - V_{g,max}\,|\sin\omega t|) * (1 - d_1(t))T_s \tag{5.1}$$

Using (5.1), the voltage conversion ratio M_1 can be expressed as

$$M_1 = \frac{V_b}{V_{g,max} \mid sin\omega t \mid} = \frac{1}{1 - d_1(t)} \tag{5.2}$$

5.3.2 Propulsion mode

In propulsion mode, power is transfered from the battery to the dc-link capacitor, either by boost or buck operation depending on battery SOC and the dc-link voltage.

5.3.2.1 Boost operation

In this mode, switch S_2 is gated through PWM signal, switch S_3 is always ON, and switches S_1 and S_4 are in OFF-state. When S_2 is turned ON, both inductors L_1 and L_2 store energy through the V_b- L_1-S_2-C_M-S_3-V_b and V_b-L_2-S_2-V_b, respectively, as shown in Fig. 5.4(a). When S_2 is turned OFF, both inductors L_1 and L_2 transfer their stored energy to the dc-link capacitor through the path V_b-L_1-S_3-D_8-V_{hv}-V_b and V_b- L_2- C_M-D_8-V_{hv}-V_b, respectively. The average voltage across C_M is found as zero, and due to that volt-second balance of both inductors is same as the voltage second balance of the inductor in conventional boost converter. Let us assume the duty ratio of the switch S_2 is d_2 then the volt-second balance though inductor in a switching period T_s can be written as

$$V_b * d_2 T_s = (V_{hv} - V_b) * (1 - d_2) T_s \tag{5.3}$$

Using (5.3), the voltage conversion ratio M_2 is expressed as

$$M_2 = \frac{V_{hv}}{V_b} = \frac{1}{1 - d_2} \tag{5.4}$$

The battery current i_b is the sum of the currents through inductors L_1 and L_2, which is expressed as

$$i_b = i_{L1} + i_{L2} \tag{5.5}$$

The average currents of L_1 and S_3 are equal to average output current, I_{hv} then I_{L_2} is given as

$$I_{L2} = I_b - I_{hv} \tag{5.6}$$

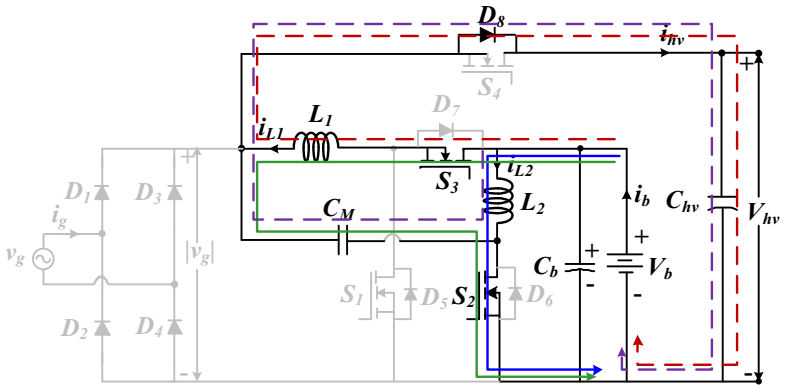

(a)

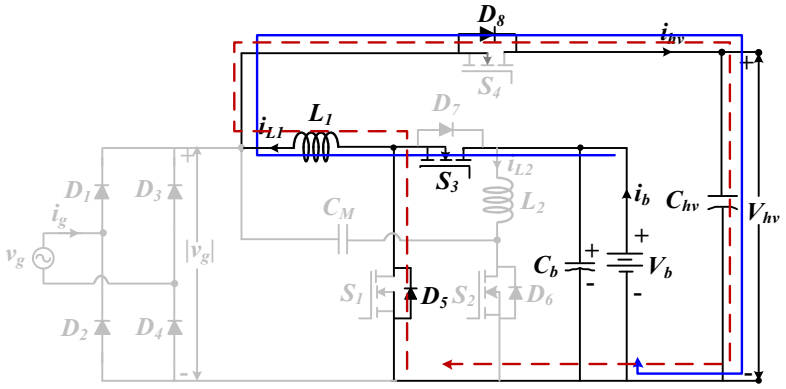

(b)

Fig. 5.4. Operation of the proposed integrated converter during propulsion mode, (a) Boost mode, (b) buck mode

5.3.2.2 Buck operation

The propulsion buck mode is initiated by PWM gating of S_3. When switch S_3 is turned ON, inductor L_1 stores energy through the path, V_b-S_3-L_1-D_8-V_{hv}-V_b, as shown in Fig. 5.4(b). When S_3 is turned OFF inductor L_1 transfers its energy to the dc-link through the path D_5-L_1-D_8-V_{hv}. While L_2 and C_M form a low-frequency filter between input and output, and have insignificant effects in steady state. Let us assume that the duty ratio of the switch S_3 is d_3. The volt-second balance of inductor L_1 is written as

$$(V_b - V_{hv}) * d_3 T_s = V_{hv} * (1 - d_3) T_s \tag{5.7}$$

From (5.7), the voltage conversion ratio M_3 can be expressed as

$$M_3 = \frac{V_{hv}}{V_b} = d_3 \tag{5.8}$$

5.3.3 Regenerative braking mode

The power transfer in regenerative braking takes place from the dc-link system to the battery through buck or boost mode of operation. The operation of these two modes has been explained in following Sections.

5.3.3.1 Boost operation

The operation of this mode is same as the operation of plug-in charging mode, only difference is, the input voltage in this mode, is V_{hv} instead of $V_{g,max}\ |sin(\omega t)|$. In this mode, switch S_4 is always ON and switch S_1 is gated through PWM. When S_1 is turned ON, L_1 stores energy through the path V_{hv}-S_4- L_1-D_7-V_b-V_{hv}. When S_1 turns OFF, L_1 transfers its stored energy to the capacitor C_b/battery through the path V_{hv}-S_4- L_1-S_1- V_{hv} . Let us assume the duty ratio of the switch S_1 in this mode is d_4. The volt-second through inductor L_1 in switching period T_s can be written as

$$V_h v * d_4 T_s = (V_b - V_h v) * (1 - d_4) T_s \tag{5.9}$$

The voltage conversion ratio M_4 from (5.9) is given as

$$M_4 = \frac{V_b}{V_{hv}} = \frac{1}{1 - d_4} \tag{5.10}$$

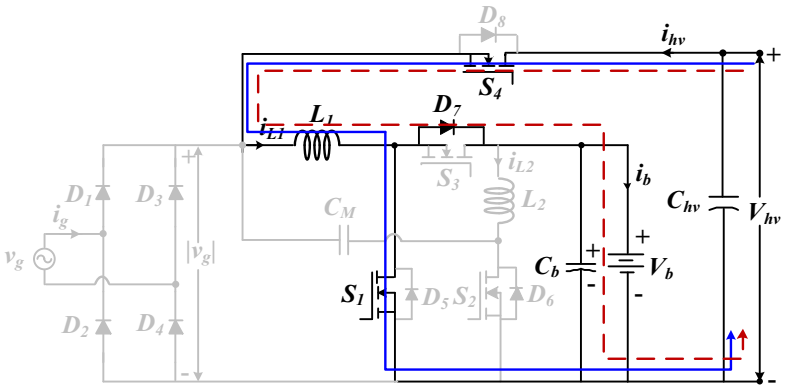

(a)

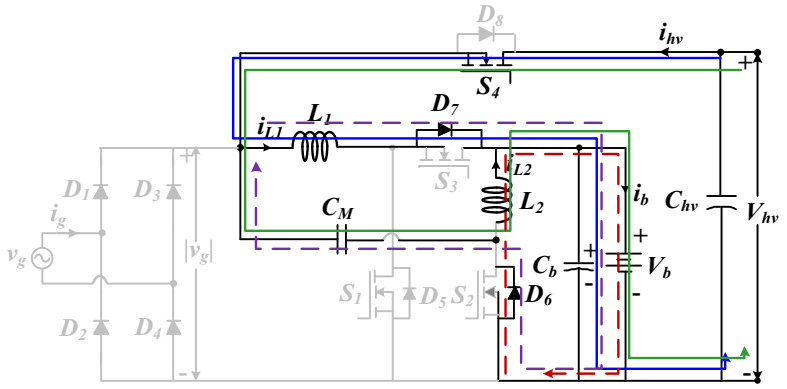

(b)

Fig. 5.5. Operation of the proposed converter during regenerative mode, (a) boost mode, (b) buck mode

5.3.3.2 Buck operation

In this mode, switch S_4 is PWM gated and all other switches are in OFF-state. When S_4 is turned ON, inductor L_1 stores energy through the path V_{hv}-S_4-L_1-D_7-V_b-V_{hv}, and inductor L_2 stores energy through the path V_{hv}-S_4-C_M-L_2-V_b. When switch S_4 is turned OFF, both inductors L_1 and L_2 supply energy to the battery and capacitor C_b through the path C_M-L_1-D_7-V_b-D_6, and L_2-D_6-V_b, respectively as shown in Fig. 5.5(b). In the steady state voltage across the capacitor, C_M will be zero. Therefore, the volt-second balance of L_1 and L_2 will be the same. Let us assume the duty ratio of the switch S_4 is d_5. The volt-second balance applied to the inductors in a switching period T_s is given as

$$(V_{hv} - V_b) * d_5 T_s = V_b * (1 - d_5) T_s \tag{5.11}$$

From (5.11), the voltage conversion ratio M_5 can be expressed as

$$M_5 = \frac{V_b}{V_{hv}} = d_5 \tag{5.12}$$

The battery current i_b is the sum of the currents through inductor L_1 and L_2.

$$i_b = i_{L1} + i_{L2} \tag{5.13}$$

The average currents of L_1 and D_7 in steady state is equal to the average dc-link current I_{hv}, then I_{L2} is expressed as

$$I_{L2} = I_b - I_{hv} \tag{5.14}$$

5.4 Comparative Analysis

5.4.1 Loss analysis

In this Section, losses of the proposed integrated converter are compared with losses integrated converter [98] shown in Fig. 5.2(b), specifically in propulsion boost mode and regenerative braking buck mode. The reasons for selection of these modes only are discussed below.

The proposed integrated converter has lower conduction losses in the propulsion boost mode than converter [98], which is explained as: when switch S_3 conducts, it carries the output current I_{hv} while counterpart switch $S_3^{'}$ of the converter [98] carries input current I_b. In the boost operation of the converter $I_{hv} < I_b$; therefore, switch S_3 has lower conduction loss than switch $S_3^{'}$. In addition to this, input current I_b is shared between two inductors, which results in lower inductor copper loss compared to the inductor copper loss of the converter [98]. The switch S_3 and inductor (L_1, L_2) conduction losses are normalized with respect to conduction losses of the switch $S_3^{'}$ and inductor L of the converter [98] as function of V_{hv}/V_b, which is shown in Fig. 5.6(a).

Furthermore, in regenerative braking buck mode, input current I_{hv} flows through diode D_7 while counterpart diode $D_7^{'}$ of the converter [98] carries output current I_b, as in buck operation $I_{hv} < I_b$. Therefore, conduction loss of diode D_7 is lower compared to conduction loss of $D_7^{'}$. In addition to this, output current I_b is shared between two inductors; therefore, inductor copper loss also reduces. The diode D_7 and inductors (L_1, L_2) conduction losses are

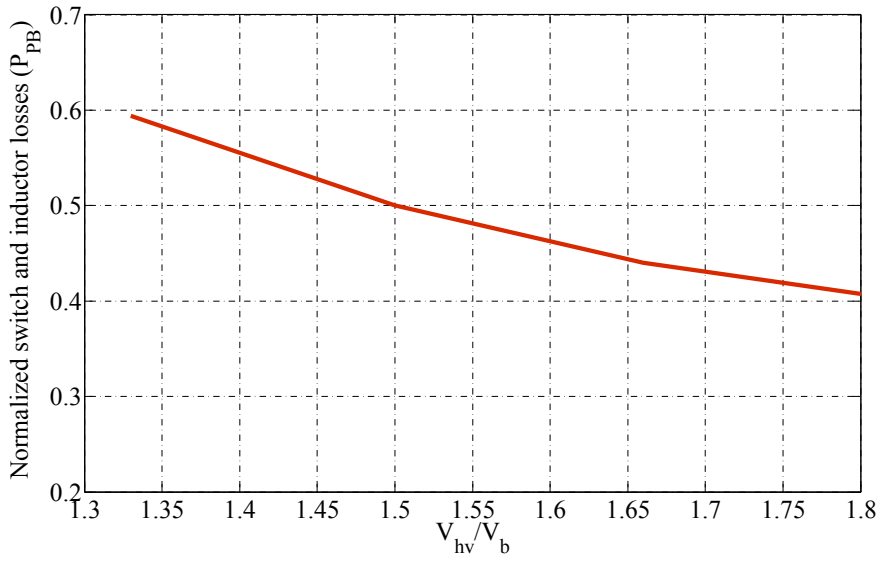

(a)

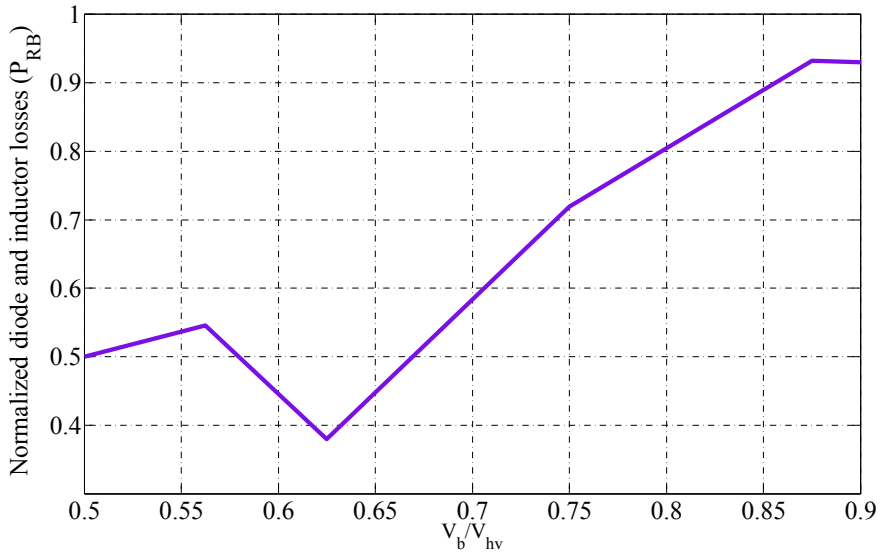

(b)

Fig. 5.6. (a) Normalized switch and inductor loss of the proposed integrated converter in propulsion boost mode, (b) Normalized diode and inductor losses of the integrated converter in regenerative buck

normalized to the conduction losses of the diode $D_7^{'}$ and inductor L of the converter [98] as function of V_b/V_{hv}, which is shown in Fig. 5.6(b).

The mathematical expressions of normalized conduction losses for propulsion boost mode (P_{PB}) and regenerative buck mode (P_{RB}) can be written as

$$P_{PB} = \frac{I_{s_3,rms}^2 * r_{ds} + (I_{L1,rms}^2 + I_{L2,rms}^2) * r_{L_{12}}}{(I_{s_3^{'},rms}^2 * r_{ds} + I_{L,rms}^2 * r_L)} \tag{5.15}$$

$$P_{RB} = \frac{I_{hv} * V_{D_7} + (I_{L1,rms}^2 + I_{L2,rms}^2) * r_{L12}}{(I_b * V_{D_7^{'}} + I_{L,rms}^2 * r_L)} \tag{5.16}$$

where $I_{s_{3,rms}}$ and $I_{s_{3,rms}^{'}}$ = RMS current of S_3 and $S_3^{'}$, respectively, $I_{L1,rms}$, $I_{L2,rms}$ and $I_{L,rms}$ = RMS current of L_1, L_2 and L, respectively; I_{hv} and I_b = average current through the dc-link and battery, respectively; V_{D_7} and $V_{D_7^{'}}$ = voltage drop of D_7 and $D_7^{'}$, respectively; $r_{L_{12}}$ = inductor resistance of L_1 and L_2; r_L = resistance of inductor L and r_{ds} = switch resistance.

The reduction of conduction losses in these two modes is desirable from battery charge point of view, which is one of the important feature of proposed converter. Since propulsion boost mode and regenerative buck mode are more common than propulsion buck mode and regenerative braking boost mode, the improvement is manifested more. Moreover, in propulsion mode, when battery SOC is low (lower battery voltage), the converter operates in boost mode. At lower battery voltage, input current will be high; thus, efficiency improvement (lower losses) in boost mode results in a longer vehicle run. In case of regenerative mode, at higher speed back EMF of the machine will be high; hence, converter must operate in buck mode to capture the braking energy. Thus, the efficiency improvement in buck mode again contribute to a longer run of vehicle.

5.4.2 Size reduction of L_2

In propulsion boost mode or regenerative braking buck mode current flows through both inductors L_1 and L_2. Due to high power rating of propulsion mode, core size and winding thickness of inductor L_2 are decided by this mode only. The core size an inductor is determined by the following equation as [116]

$$\frac{LI_m I_{RMS}}{k_W B_m J} = A_c \tag{5.17}$$

where B_m = maximum saturation flux density; K_w = window space factor; J = peak current carrying capacity; A_c = effective area for the magnetic path as well as electric current; I_m = peak current; I_{RMS} = RMS current and L = inductance value. Based on (5.17) reduction of the core size of inductance L_2 compared to single inductor converter in [98] can be examined with the following assumptions.
1) Input Peak and RMS currents are equal.
2) Peak input current through inductor L_2 in propulsion boost mode is normally higher than regenerative buck mode.

Let us take the worst situation for propulsion boost, i.e., 50% duty cycle (the dc-link voltage is twice of the battery voltage), inductor (L_2) current will be half of total input current I_b. Therefore, the effective core area of L_2 from (5.17) can be reduced by 25% compared to single inductor converter in [98]. Further, the size of winding thickness of L_2 also will be half compared to winding thickness of inductor in [98]. Therefore, the size of inductor L_2 is approximately reduced by more than 25%.

5.4.3 Comparison with conventional single-stage chargers

The conventional single-stage battery charger topologies are namely the boost PFC converter, inverting buck/boost PFC converter, SEPIC PFC converter, and Cuk PFC converter, as shown in Fig. 5.7. The proposed converter has the least number of components compared conventional topologies shown in Table 5.2. To have a fair comparison of the proposed converter with these single stage converters, the dc/dc converter connected between the battery and the dc-link is assumed to be a four-quadrant bidirectional dc.dc converter. The boost PFC converter can only charge the battery when battery voltage is more than the peak grid voltage. While inverting buck/boost and Cuk converter have negative output voltage with respect to the input. The problem with negative polarity has been discussed in Chapter 2 in Section 2.6. The Cuk and SEPIC based converter topologies have one additional inductor compared with the proposed integrated converter.

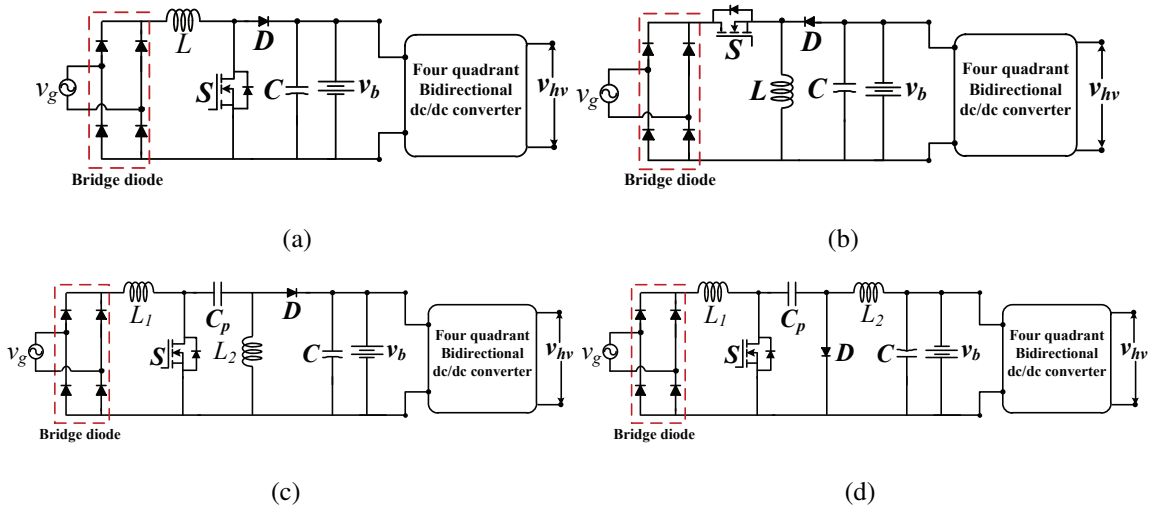

Fig. 5.7. Conventional single-stage EV battery chargers, (a) PFC boost converter, (b) inverting buck/boost PFC converter, (c) SEPIC PFC converter, (d) Cuk PFC converter

Table 5.2. Comparison of proposed charger with conventional single-stage chargers

Charger topologies	Voltage Polarity	Switch	Diode	Inductor	Capacitor	Battery voltage range
Boost PFC converter	+	5	5	2	2	$V_{grid,peak}$-$V_{b,max}$
Inverting buck/boost PFC converter	-	5	5	2	2	0-$V_{b,max}$
SEPIC PFC converter	+	5	5	3	3	0-$V_{b,max}$
Cuk PFC converter	-	5	5	3	3	0-$V_{b,max}$
Proposed integrated converter	+	4	4	2	3	$V_{grid,peak}$-$V_{b,max}$

5.5 Design of the Proposed Converter

This Section discusses the design procedure of L_1, L_2, C_M, C_b and C_{hv}.

5.5.1 Selection of L_1 and L_2

In high-power applications, CCM operation of the converter is preferred over DCM as it exhibits lower power loss. To ensure the CCM operation, it is essential to determine the value of inductance in each mode and the largest value will be chosen as final value for inductors.

5.5.1.1 Plug-in charging mode

In plug-in charging, the converter operates in boost mode. The duty cycle d_1(t) from (5.2) for operation in CCM is given as

$$d_1(t) = 1 - \frac{V_g, max\,|\sin \omega t|}{V_b} \tag{5.18}$$

The inductor L_1 current ripple is relevant for converter operation in CCM. Thus, the CCM condition can be written as

$$i_{L1} > \Delta i_{L1} \tag{5.19}$$

where

$$\Delta i_{L1} = \frac{V_g, max\,|\sin \omega t|\, d_1(t) T_s}{2L_1} \tag{5.20}$$

Combining (5.18)-(5.20), yields CCM condition as

$$L_1 > \frac{\left(1 - \frac{V_g, max|\sin \omega t|}{V_b}\right) \mathrm{R}_e T_s}{2} \tag{5.21}$$

where R_e is the emulated input resistance to a given output power. In order to ensure the CCM operation throughout line cycle under all input voltages and output power levels, from (5.21) we can write

$$L_1 > \frac{R_{e,max} T_s}{2} \tag{5.22}$$

where $R_{e,max}$ corresponds to the lowest power, and the largest input voltage ac voltage.

5.5.1.2 Propulsion mode

(a) Boost mode:

In this mode, both inductors L_1 and L_2 current ripples are relevant for operation in CCM. Therefore, the CCM condition can be written as

$$i_b = i_{L1} + i_{L2} > \Delta i_{L1} + \Delta i_{L2} \tag{5.23}$$

where inductor current ripples Δi_{L1} and Δi_{L2} is given as

$$\Delta i_{L1} = \frac{V_b d_2 T_s}{2L_1} \tag{5.24}$$

$$\Delta i_{L2} = \frac{V_b d_2 T_s}{2L_2} \tag{5.25}$$

From (5.23)-(5.25) and using the result of (5.4) yields CCM condition as

$$L_{eq} > \frac{V_b^2 \left(V_{hv} - V_b\right) RT_s}{2V_{hv}^3} \tag{5.26}$$

where $L_{eq} = L_1 L_2/(L_1 + L_2)$ and R is the output resistance.

(b) Buck mode:

In this mode, only inductor L_1 current ripple is relevant for operation in CCM. Thus, the CCM condition can be written as

$$i_{L1} > \Delta i_{L1} \tag{5.27}$$

where

$$\Delta i_{L1} = \frac{\left(V_b - V_{hv}\right) d_3 T_s}{2L_1} \tag{5.28}$$

Combining (5.27),(5.28) and using result of (5.8), yields CCM conditions as

$$L_1 > \frac{\left(1 - \frac{V_{hv}}{V_b}\right) T_s R}{2} \tag{5.29}$$

5.5.1.3 Regenerative braking mode

(a) Boost mode:

This mode is exactly same as boost operation of plug-in charging mode, therefore only inductor L_1 current ripple is relevant for CCM operation. The CCM condition can be expressed as

$$i_{hv} > \Delta i_{L1} \tag{5.30}$$

where

$$\Delta i_{L1} = \frac{V_{hv} d_4}{2L_1 f_s} \tag{5.31}$$

From (5.30), (5.31) and (5.10), the CCM condition can be written as

$$L_1 > \frac{V_{hv}^2 \left(V_b - V_{hv}\right) RT_s}{2V_b^3} \tag{5.32}$$

(b) Buck mode:

In buck mode, both inductors current ripples are responsible for operation in CCM. Therefore, the CCM condition can be written as

$$i_b = i_{L1} + i_{L2} > \Delta i_{L1} + \Delta i_{L2} \tag{5.33}$$

where inductor current ripples are expressed as

$$\Delta i_{L1} = \frac{(V_{hv} - V_b) d_5 T_s}{2L_1} \tag{5.34}$$

$$\Delta i_{L2} = \frac{(V_{hv} - V_b) d_5 T_s}{2L_2} \tag{5.35}$$

Combining (5.33)-(5.35) and using the result of (5.12) gives the CCM condition as

$$L_{eq} > \frac{\left(1 - \frac{V_b}{V_{hv}}\right) T_s R}{2} \tag{5.36}$$

Using parameters of Table 5.3, the selected value of L_1 and L_2 is 3 mH.

5.5.2 Selection of capacitor C_M

The value of capacitor C_M affects voltage V_b and V_{hv} in plug-in charging and propulsion modes, respectively as well as current through L_2-C_M path. Therefore, the natural frequency f_r of L_2 and C_M should be more than the line frequency f_L and less than switching frequency f_s; therefore, f_r can be expressed as

$$f_L < f_r < f_s \tag{5.37}$$

where

$$f_r = \frac{1}{2\pi\sqrt{L_2 C_M}} \tag{5.38}$$

For f_r = 0.2 kHz and L_2 = 3 mH, the calculated value of C_M from (5.38) is 0.63 μF.

5.5.3 Selection of capacitor C_b

With regards to the parallel capacitor across the battery terminal, twice of the line frequency voltage ripple is more critical since it directly affects the charging voltage than switching frequency voltage ripple. Therefore, capacitor C_b is determined by twice of the line frequency voltage ripple as [103]

$$C_b = \frac{P_b}{4 f_L \Delta v_b V_b} \tag{5.39}$$

where Δv_b is the capacitor C_b voltage ripple. From (5.39), the value C_b is 2.1 mF for $\Delta v_b <$ 2% of V_b.

5.5.4 Selection of capacitor C_{hv}

The dc-link capacitor C_{hv} is required to suppress the dc-link voltage ripple. The value of this capacitor is determined by propulsion operation mode then it is expressed as [105]

$$C_{hv} = \frac{d_3}{R f_s \frac{\Delta v_{hv}}{V_{hv}}} \tag{5.40}$$

where Δv_{hv} is the capacitor C_{hv} voltage ripple. From (5.40), the value of C_{hv} is 187.5 μF for $\Delta v_{hv} < 2\%$ of V_{hv}.

5.6 Control Strategy

The controller block diagram for different modes is shown in Fig. 5.8. During battery charging from grid the reference battery power is divided by instantaneous battery voltage to generate reference battery current. This reference current is compared to actual battery current and error is fed to outer proportional-integral (PI) controller G_{ib}(z), which is expressed as

$$G_{ib}(z) = K_p + \frac{K_i T_s}{z-1} \tag{5.41}$$

where K_p is the proportional gain to adjust the control bandwidth and K_i is the integral term to achieve high dc compensation gain. The outer PI controller G_{ib}(z) generates a dc signal, which is multiplied by a unit sinusoidal template to generate reference current for an inner digital PI controller, and can be expressed as

$$G_{iL}(z) = K_{pc} + \frac{K_{ic} T_s}{z-1} \tag{5.42}$$

where K_{pc} is the proportional gain and K_{ic} is the integral gain. These two coefficients should be tuned such that the bandwidth of the controller is kept between one sixth to one tenth of the switching frequency. Further, to achieve accurate current tracking and make the control system robust against supply variation, an open loop duty cycle is derived from (5.2) is added to the output of the inner PI controller $G_{iL}(z)$ to arrive final reference PWM signal, as shown in Fig. 5.8(a).

In propulsion and regenerative braking modes, an average current mode controller is used. Depending on the operating mode, appropriate switches are turned ON. In the case of propulsion mode, the dc-link voltage is regulated using a digital PI controller G_{hv}(z) by generating reference battery current for a common digital PI controller G_{ibc}(z) (used in both modes).

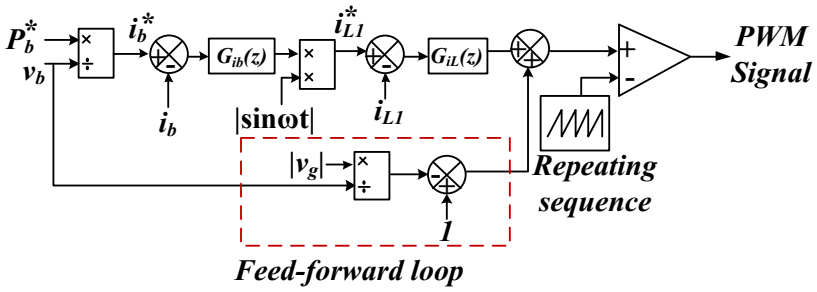

(a)

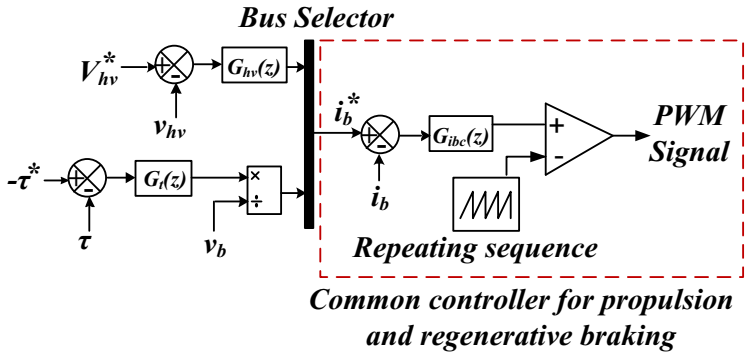

(b)

Fig. 5.8. (a) Control diagram of plug-in charging mode, (b) propulsion and regenerative braking modes

In regenerative braking, the reference quantity is usually torque. The torque is converted into reference charging power by a digital PI controller $G_t(z)$, which is divided by instantaneous battery voltage to generate a reference battery current for the inner PI controller G_{ibc}(z), as shown in Fig. 5.8(b).

5.7 Results and Discussion

5.7.1 Simulation results

The simulation study of the proposed converter was carried out in MATLAB/Simulink environment and the circuit parameters used in this study are listed in Table 5.3.

The simulation waveforms for plug-in charging at 1 kW charging power are shown in Fig. 5.9. From Fig.5.9(a), the grid voltage $v_g/$ 24 and grid current i_g are seen to be in same phase which shows converter is operating under UPF condition. The THD bar chart of input current is shown in Fig.5.10, where the THD is 3.6%. The UPF operation of converter reduces cost

of electricity usages and also mitigates the reactive power loss in grid system.

Table 5.3. Simulation circuit parameters

Parameters	**Value**s
Grid voltage (V_g)	*220/30 V*
dc-link voltage (V_{hv})	*400/50 V*
Line frequency (f_L)	*50Hz*
Battery voltage (V_b)	*345.6/36 V*
Nominal charging power (P_b)	*1kW/ 80 W*
L_1/L_2	*3 mH*
$C_{hv}/C_M/C_b$	*330/1/2200μF*

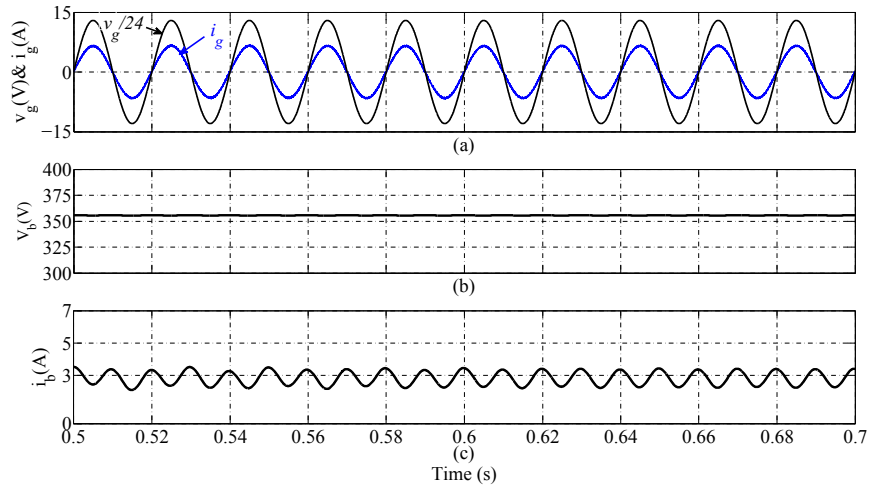

Fig. 5.9. Simulation waveforms in plug-in charging mode with 1 kW reference charging power, (a) grid voltage and current, (b) battery voltage, (c) battery current

The battery voltage is around 354 V with 20% of SOC (Fig. 5.9(b)) and the measured average battery current is 2.82 A, as shown in Fig. 5.9 (c). Further, in steady state, the voltage across coupling capacitor C_M is the difference of $|v_g|$ and V_b shown in Fig. 5.11(a), and current through C_M is almost zero, which is indicated in Fig. 5.11(b).

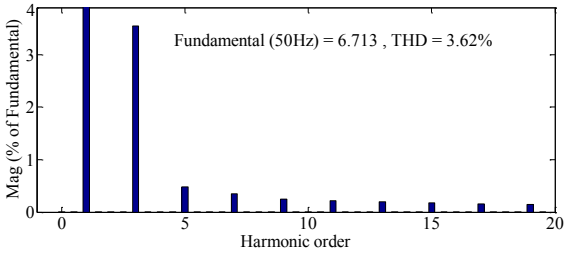

Fig. 5.10. THD of grid current

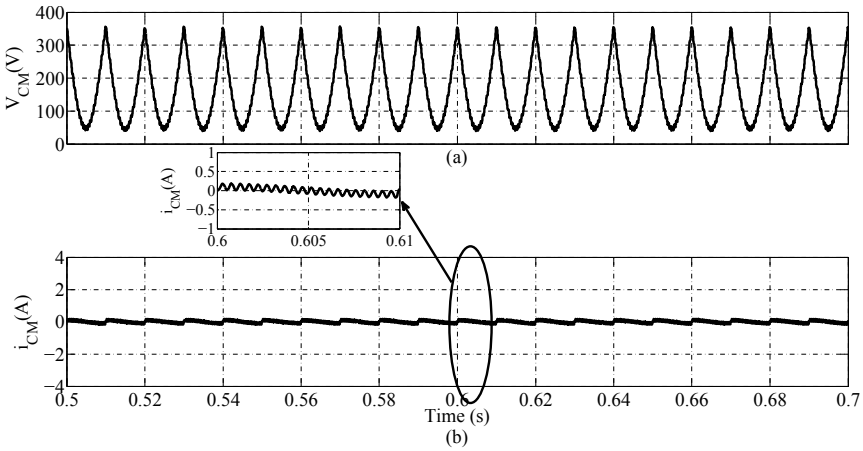

Fig. 5.11. Simulation waveforms in plug-in charging mode with 1 kW reference charging power, (a) voltage across capacitor C_{CM}, (b) current through C_{CM}

The performance of closed loop control scheme is done by step change in reference charging power which is shown in Fig. 5.12. The grid current is again in phase with the grid voltage even after the change of reference power from 1 to 1.5 kW at t = 2 s and from 1.5 to 1 kW at t = 2.5 s. The corresponding change in the battery current is shown in Fig. 5.12(c) which varies between 2.8 to 4.23 A.

In propulsion mode, the battery voltage is either stepped up or stepped down depending on the battery SOC and the dc-link voltage. The reference dc-link voltage is chosen as 400 V with 2 kW output power. Therefore, the battery voltage 345.6 V is boosted to 400 V. From Fig. 5.13(a), the dc-link voltage is regulated at 400 V, the battery terminal voltage (Fig. 5.13(b)) is around 352 V slightly less than charging mode battery voltage, it is due to drop across internal resistance of the battery and recorded battery current (Fig. 5.13(c)) is found 5.85 A. Therefore, calculated power at battery side is 2.059 kW hence, efficiency of

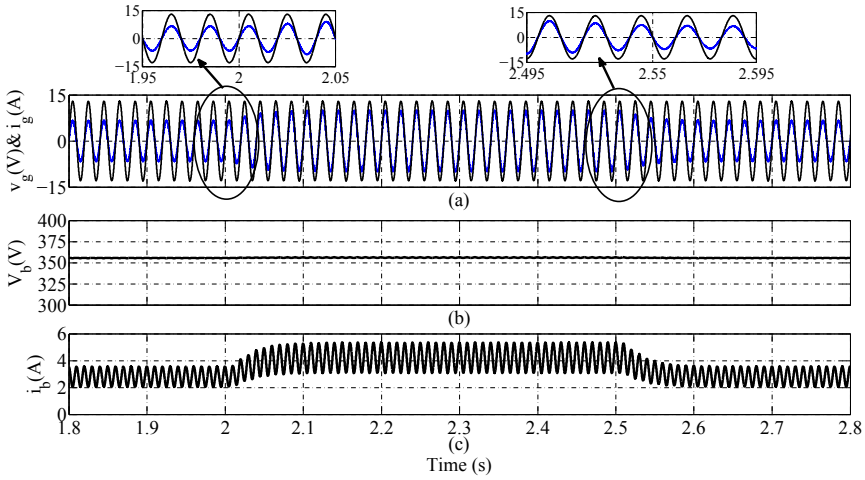

Fig. 5.12. Simulation waveforms in plug-in charging mode with change of reference charging power, (a) grid voltage and current, (b) battery voltage, (c) battery current

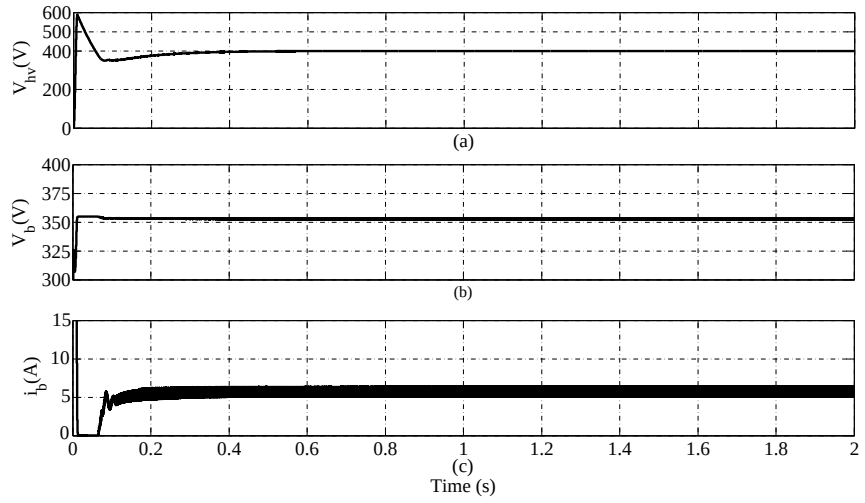

Fig. 5.13. Simulation waveforms of propulsion mode with 2 kW load, (a) dc-link voltage, (b) battery voltage, (c) battery current

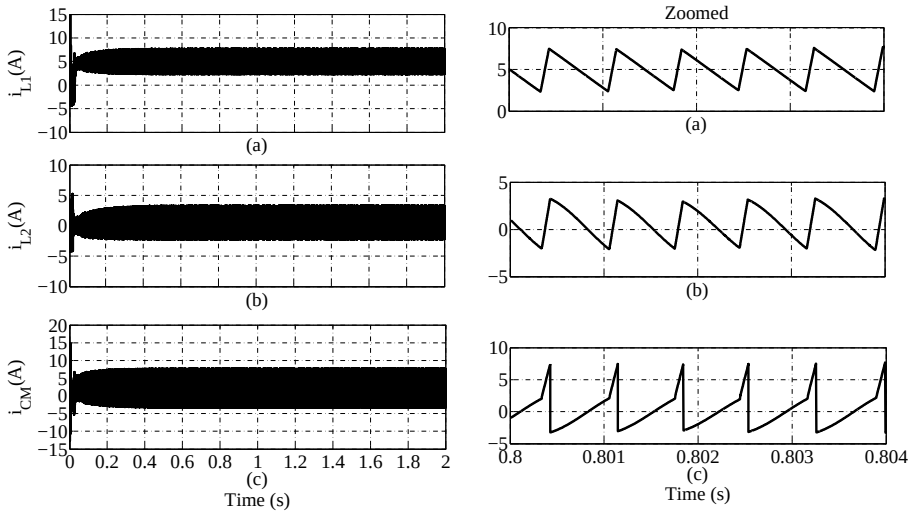

Fig. 5.14. Simulation waveforms of propulsion mode with 2 kW load, (a) Current through L_1, (b) Current through L_2, (c) Capacitor current i_{CM}

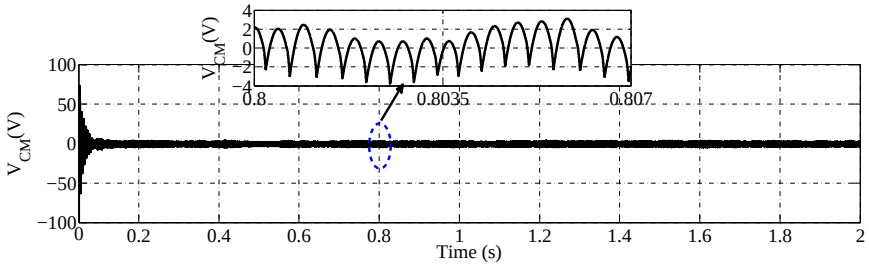

Fig. 5.15. Voltage waveform across capacitor C_M

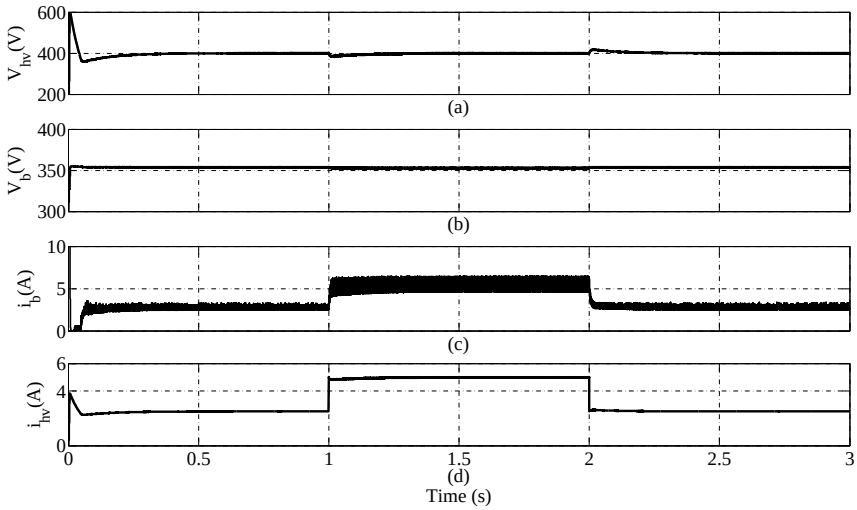

Fig. 5.16. Dynamic response of propulsion mode, (a) dc-link voltage, (b) battery voltage, (c) battery current, (d) dc-link current

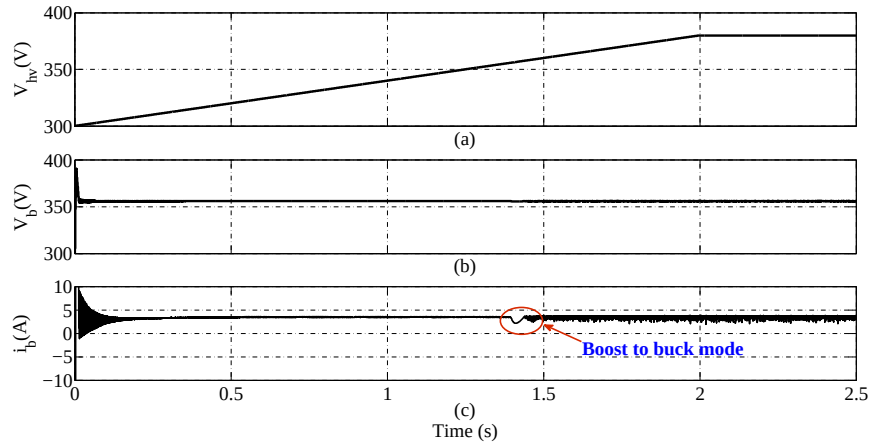

Fig. 5.17. Simulation waveforms of regenerative braking with varying dc-link voltage, (a) dc-link voltage, (b) battery voltage, (c) battery current

the converter at 2 kW load is 97.1%. The inductor currents i_{L1} and i_{L2}, and capacitor current through C_M are shown in Fig. 5.14. Fig. 5.15 shows voltage developed across C_M which is almost zero but a small voltage appears across this capacitor due to variation in current through L_1 and L_2 . The dynamic performance of the propulsion mode is tested with step load variations from 2 to 1 kW at t = 1 s and 1 to 1.5 kW at t = 2 s. The control target of this mode is to keep the dc-link voltage constant irrespective of the load variation, which is shown in Fig. 5.16(a). The corresponding change in the battery voltage, battery current and dc-link current with load variations are shown in Fig. 5.16(b), (c) and (d), respectively.

In regenerative mode, the dc-link voltage depends on back-EMF of the machine which is directly proportional to speed of the machine. The closed loop control of this mode is verified by linearly increasing the dc-link voltage from 300 V, t = 0 s to 380 V, t = 2 s then it is kept constant from t = 2 s to t = 2.5 s, which is shown in Fig. 5.17(a). The battery current is regulated at 3.5 A irrespective of the dc-link voltage variations and the battery voltage and current are shown in Fig. 5.17(b) and (c), respectively. The waveforms shown in Fig. 5.17 depicts both boost and buck operations of regenerative braking mode. In boost mode, the battery current is smooth while in buck mode (after t = 1.4 s), it is in oscillatory nature because of part of battery current flows through the L_2-C_M path which is responsible for oscillations in the battery current.

The Efficiency versus V_b/V_{hv} ratio curve of the proposed converter and converter [98] in

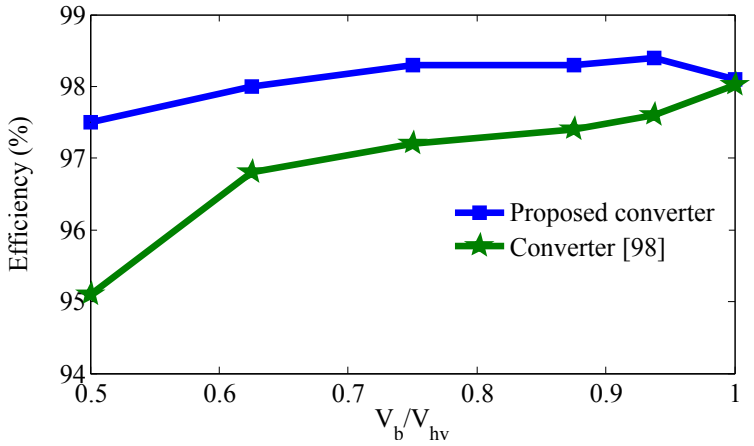

(a)

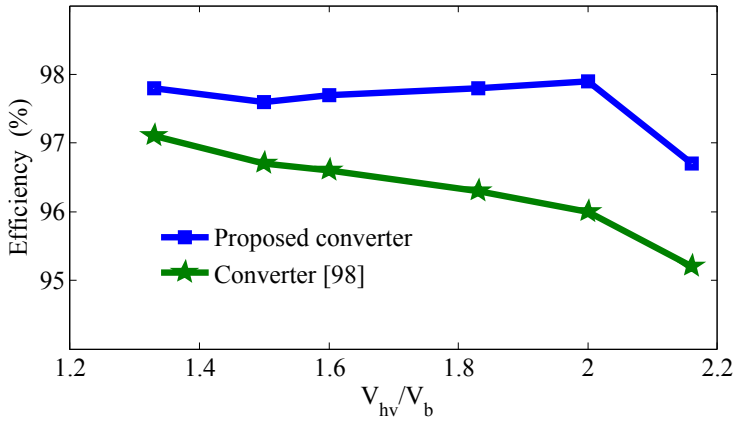

(b)

Fig. 5.18. Efficiency curves of the proposed converter and existing integrated converter (Fig. 5.2(b)), (a) regenerative braking buck mode, (b) propulsion boost mode

regenerative braking buck mode is shown in Fig. 5.18(a). It is observed that the efficiency improvement in this mode is 2-2.5% compared to the converter [98] when the ratio V_b/V_{hv} is near to 0.5. The efficiency curve in propulsion boost mode with respect to V_{hv}/V_b ratio is shown in Fig. 5.18(b). At low SOC or lower battery voltage (V_{hv}/V_b = 2), the efficiency improvement of the proposed converter is around 2% compared to converter [98].

Further, to provide consistency between simulation and hardware results, a scaled down simulation of the converter is performed with 36 V battery, 30 V grid (peak) and 50 V dc-link.

Fig. 5.19 shows simulation waveforms in plug-in charging mode; the charging power is taken as 80 W. The simulation waveforms of propulsion mode are shown in Figs. 5.20 and

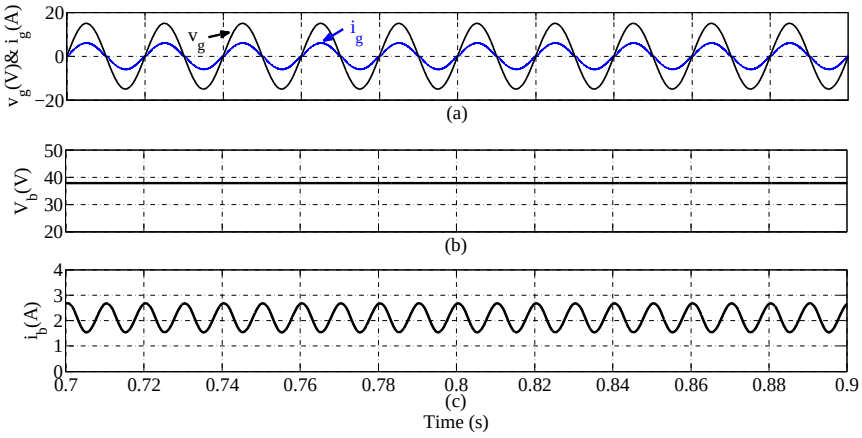

Fig. 5.19. Simulation of plug-in charging mode with 36 V battery and 80 W charging power, (a) grid voltage and current, (b) battery voltage, (c) battery current

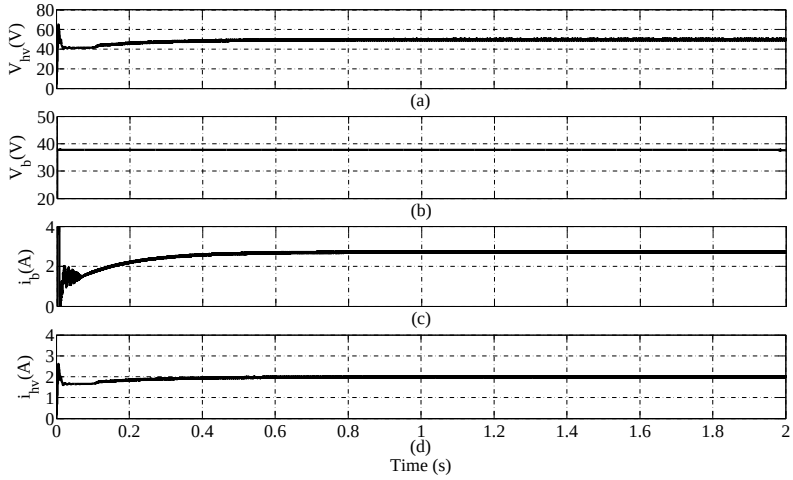

Fig. 5.20. Simulation waveforms of propulsion mode with 50 V dc-link, (a) dc-link voltage, (b) battery voltage, (c) battery current., (d) dc-link current

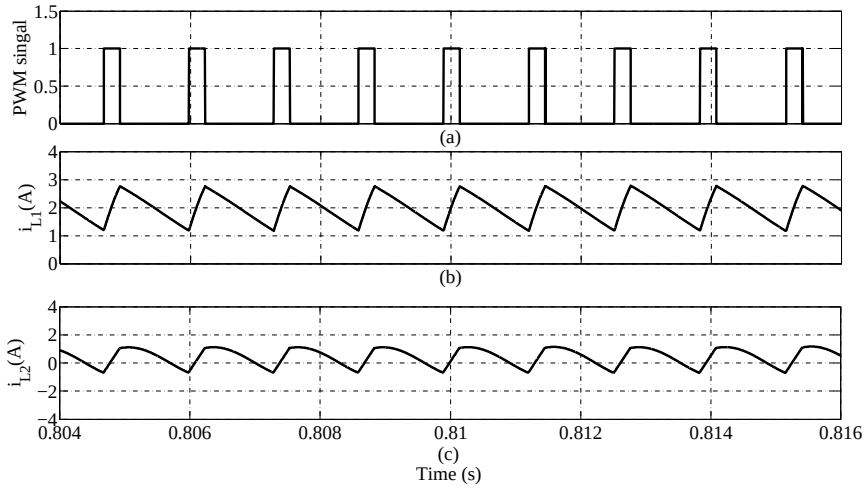

Fig. 5.21. Simulation waveforms during propulsion operation, (a) PWM signal of switch S_2, (b) current through L_1 and (c) L_2

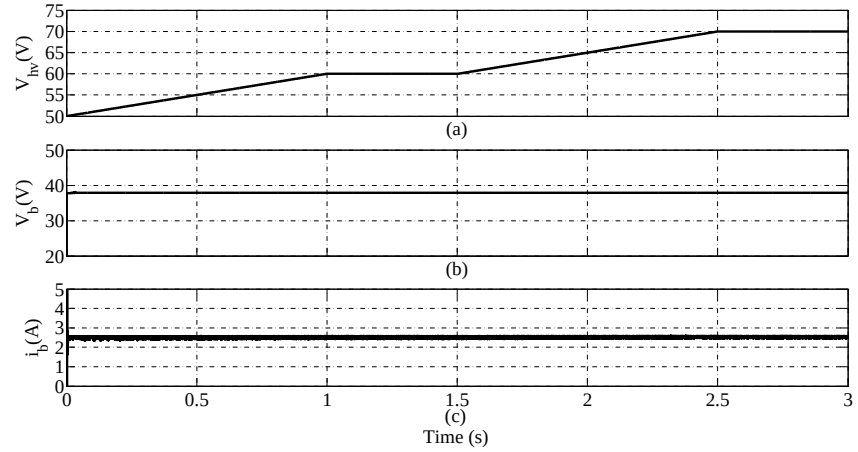

Fig. 5.22. Simulation waveforms of regenerative braking mode with dc-link voltage variations, (a) dc-link voltage, (b) battery voltage, (c) battery current

5.21. The close loop verification of regenerative braking mode is shown in Fig. 5.22.

Table 5.4. Experimental circuit parameters

Parameters	**Values**
dc-link voltage (V_{hv})	*40 V*
Line frequency (f_L)	*50Hz*
Nominal battery voltage (V_b)	*24 V*
Battery capacity	*26 Ah*
L_1/L_2	*3mH*
C_{hv}/C_M/ C_b	*330/1/2200* μF

5.7.2 Experimental results

The circuit parameters for experimental verification are listed in Table 5.4. A reduce scale laboratory prototype has been built for testing and validation of the proposed converter using 24 V battery and 40 V of dc-link voltage.

During plug-in charging mode, the average battery charging current i_b (CH4) is maintained at 1.25 A and the grid current i_g (CH2) is almost in phase with the grid voltage v_g (CH1), as shown in Fig. 5.23(a). The battery voltage V_b at CH4 is near to 24 V. The dynamic response of converter is verified by changing the reference charging power from 30-60-30 W, and corresponding variation in the grid current is shown at CH1 in Fig. 5.23(b). The grid current is still in sinusoidal shape, which shows the effectiveness of the controller.

During running mode of vehicle operation there are two modes of operation, i.e., propulsion and regenerative braking. The waveforms of propulsion mode are presented in Fig. 5.24. For satisfactory operation the inverter-drive system of the vehicle, the dc-link voltage is regulated at desired value. In the prototype model. The closed loop operation of this mode is tested by varying the load power, i.e., from 50-120-50 W while dc-link voltage regulated at 40 V shown in Fig. 5.24(a) at CH1. The corresponding variations in the battery voltage and the dc-link current are shown in Fig. 5.24(a) at CH2 and CH3, respectively.

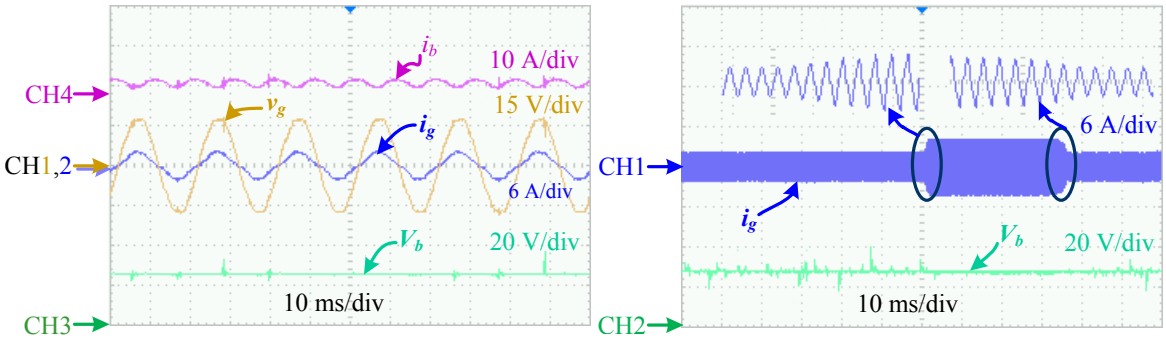

(a) (b)

Fig. 5.23. (a) Experimental waveforms in plug-in charging mode (CH1: grid voltage, CH2: grid current, CH3: battery voltage and CH4: battery current), (b) dynamic response of plug-in charging mode by increase and decrease of reference charging power

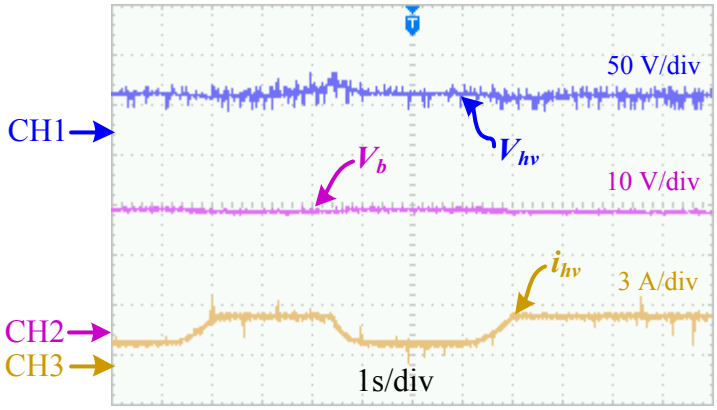

Fig. 5.24. Experimental waveforms in propulsion mode (CH1: dc-link voltage, CH2: battery voltage and CH3: dc-link current)

In regenerative mode, the battery is charged through braking energy of the motor. The relevant waveforms of this mode are presented in Figs. 5.25 and 5.26. The closed loop operation of this mode is verified by increasing the dc-link voltage from 40 to 55 V and the battery current is well regulated at 1.62 A, as shown in Fig. 5.26(a) at CH3. The closed-loop control of the converter is also tested by decrease of the dc-link voltage from 40 to 30 V, which is shown in Fig. 5.26(b).

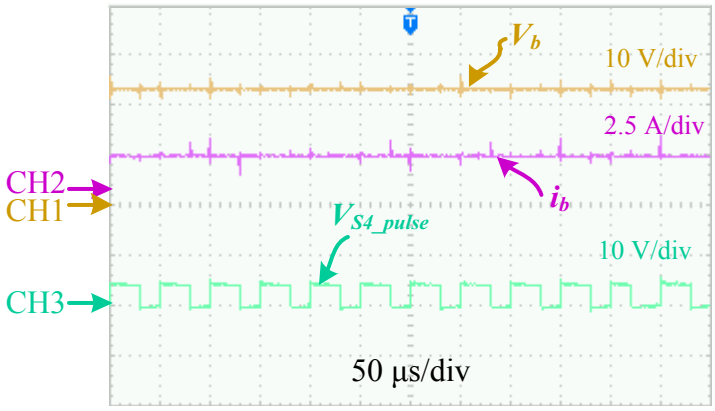

Fig. 5.25. Experimental waveforms in regenerative braking operation (CH1: battery voltage, CH2: battery current and CH3: PWM signal of switch S_4)

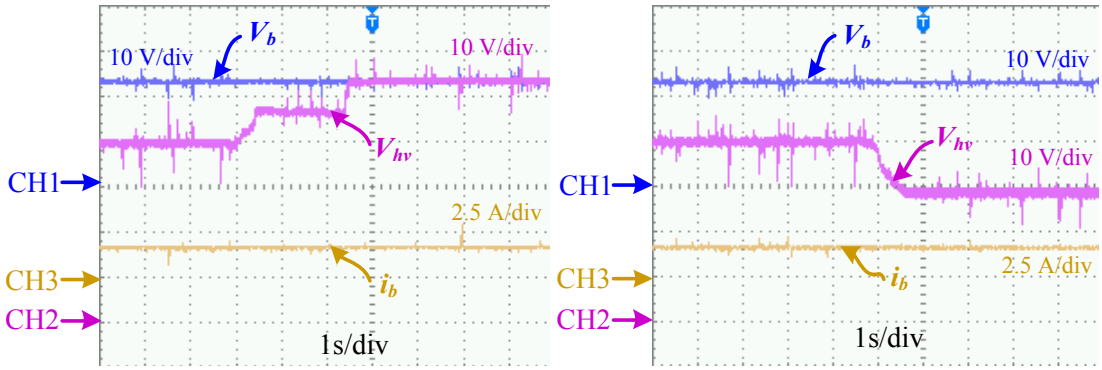

(a) (b)

Fig. 5.26. Experimental waveforms during regenerative mode, (a) verification of closed loop control of by increasing the dc-link voltage (CH1: battery voltage, CH2: dc-link voltage and CH3: battery current), (b) by decreasing the dc-link voltage

5.8 Conclusion

The integrated converter proposed in this chapter has been shown to operate for all modes of vehicle employing a single power electronic converter. In addition, this topology has an efficiency improvement 2-2.5% in boost mode of propulsion and buck mode of regenerative braking over existing integrated converters. Since propulsion boost mode and regenerative buck mode are more common than propulsion buck mode and regenerative braking boost mode then efficiency improvement leads to a long run of vehicle. The closed loop operation of each mode is verified by variations of relevant parameters in the simulation as well as

in hardware. Even though two inductors are used in the proposed converter, but the size of the second inductor is reduced by more than 25% compared to the single inductor integrated converter. Therefore, addition of second inductor is not much disadvantageous.

CHAPTER 6

CONCLUSION AND FUTURE SCOPE OF WORK

6.1 Conclusion

This thesis presented evolution of power converter topologies for on-board applications of PEVs, which were essentially based on single-stage conversion. These converters are capable of multi-mode operation to achieve battery charging, vehicle propulsion and regenerative braking. This feature of multi-mode operation is reflected in calling them as integrated converters. After evaluating the existing converter typologies, four integrated converter topologies were proposed in this thesis. These topologies are shown to achieves all modes of operation, i.e., plug-in charging,vehicle propulsion and regenerative braking. To validate the effectiveness of the proposed topologies, they are compared with existing integrated converters. Each proposed topology is supported by relevance analysis, MATLAB based simulation results and finally development of prototype hardware with experimental waveforms under various operating conditions.

The work in this thesis begins with literature review (Chapter 1) in the area relevant to research being carried out. The emphasis is placed on classification of chargers and review of conventional single-stage and integrated chargers. The non-isolated converters are found more suitable for on-board EV applications. Review of integrated chargers has been divided into two groups: a) integrated chargers that use machine winding as energy storage elements into the charging circuit with utilization of inverter switches and b) integrated chargers using diode rectifier in ac/dc stage, and bidirectional dc/dc converter incorporated into the charging circuit. Review of each topology is focused on their merits and demerits. Based on this literature review, the research objectives for present work were formulated in Chapter 1.

The research work contributed in this thesis is to development of the integrated converters. Even though conclusion has been given at the end of each chapter, the following points are concluded by comparing the proposed topologies with each other.

- The proposed ZETA-SEPIC based integrated converter has buck/boost operation in each mode, as shown in Table 6.1. But this topology has the limitation of high volt-

Table 6.1. Comparative study of the proposed converters in terms of mode of operation and number of components.

Proposed topologies	Mode of operation			Number of components				
	Plug-in charging	Propulsion	Regenerative braking	Switch	Diode	Inductor	Capacitor	Sensor
ZETA-SEPIC based Integrated converter	Boost/buck	Buck/boost	Buck/boost	3	4	2	3	5
Modified ZETA based Integrated converter	Buck/boost	Boost	Buck	3	4	2	3	5
SEPIC based Integrated converter	Buck/boost	Boost	Buck	2	5	2	3	4
Integrated converter with reduced conduction losses	Boost	Buck/boost	Buck/boost	4	4	2	3	5

age/current stresses (sum of input/output quantities (voltage/current)) on semiconductor devices in each mode, as shown in Table 6.2. Due to high stresses, efficiency of the converter in each mode is lower compared to other proposed converters (except plug-in charging mode of modified ZETA based converter), which is shown in Fig. 6.1.

- The modified ZETA based integrated converter has low stresses (either input or output voltage/current) in propulsion and regenerative braking modes. Also, this converter has the highest peak efficiency in propulsion and regenerative braking modes, as shown in Fig. 6.1.

- The SEPIC based integrated converter has low stresses in propulsion and regenerative braking modes same as the modified ZETA based integrated converter. Moreover, this converter has fewer number of components compared to other proposed converters, as shown in Table 6.1.

- The TSBuB based integrated converter has low stresses in each mode compared to other proposed converters, as shown in Table 6.2. This converter has higher efficiency similar to modified ZETA based converter in propulsion boost mode and regenerative braking buck mode.

Table 6.2. Voltage and current stresses on semiconductors in each mode

Proposed topologies	Plug-in charging		Propulsion		Regenerative braking	
	Voltage	Current	Voltage	Current	Voltage	Current
ZETA-SEPIC based Integrated converter	$V_{out} + V_{in}$	$I_{out} + I_{in}$	$V_{out} + V_{in}$	$I_{out} + I_{in}$	$V_{out} + V_{in}$	$I_{out} + I_{in}$
Modified ZETA based Integrated converter	$V_{out} + V_{in}$	$I_{out} + I_{in}$	V_{out} or V_{in}	I_{out} or I_{in}	V_{out} or V_{in}	I_{out} or I_{in}
SEPIC based Integrated converter	$V_{out} + V_{in}$	$I_{out} + I_{in}$	V_{out} or V_{in}	I_{out} or I_{in}	V_{out} or V_{in}	I_{out} or I_{in}
Integrated converter with reduced conduction losses	V_{out} or V_{in}	I_{out} or I_{in}	V_{out} or V_{in}	I_{out} or I_{in}	V_{out} or V_{in}	$I_{out} + I_{in}$

where V_{out}, I_{out}, I_{in} and V_{in}, are the output voltage, output current, input voltage and input current of operating mode, respectively.

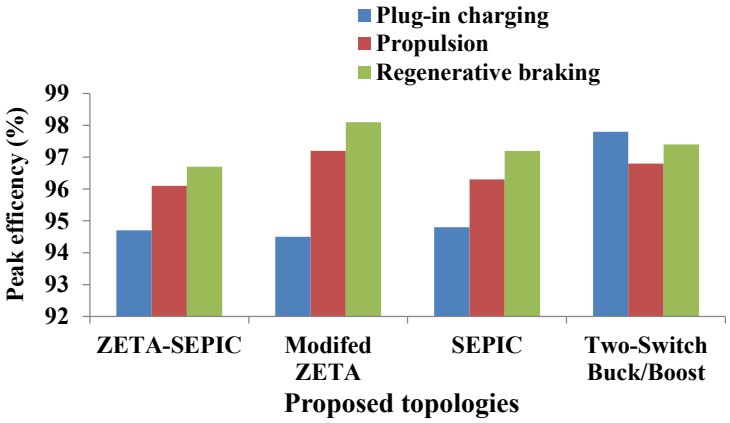

Fig. 6.1. Peak efficiency plot of the proposed converters

6.2 Future Scope of Work

The research work presented in this thesis focuses on converter part of PEVs. The different integrated converters were proposed. Future expansion of presented work in this thesis will include:

- The drive system of the vehicle can be included to interface various types of motors such as induction, PMSM and SRM with the integrated converters.

- It is possible to use the solar photovoltaic (PV) system for battery charging which requires a dc/dc converter that interfaces PV system with integrated converter. When solar power is available, the battery will be charged through it, if it is not available, plug-in charging mode can be activated. This will save the fossil fuel based electricity and such EVs can be more environmental friendly and attractive for users.

- Use of super capacitor with PV interfaced integrated converter can be another future scope of this work. The high power density super capacitor can be used in the two ways in the vehicles; a) with battery or b) in stand-alone mode. When super capacitor is used with battery, either it can be directly connected to the dc-link or through a dc/dc converter depending on application. Further, stand-alone mode of super-capacitor is not much attractive due to low energy density and capacitor can not hold charge for long as does the battery. The major challenges of these future works are addition of dc/dc converters that will add weight in OBC. Control complexity will increase when both PV and super capacitor are used simultaneously.

BIBLIOGRAPHY

[1] C. C. Chan and K. T. Chau, "An overview of power electronics in electric vehicles," *IEEE Transactions on Industrial Electronics*, vol. 44, no. 1, pp. 3–13, Feb. 1997.

[2] A. Emadi, Y. J. Lee, and K. Rajashekara, "Power electronics and motor drives in electric, hybrid electric, and plug-in hybrid electric vehicles," *IEEE Transactions on Industrial Electronics*, vol. 55, no. 6, pp. 2237–2245, Jun. 2008.

[3] A. K. Singh and M. K. Pathak, "An improved two-stage non-isolated converter for on-board plug-in hybrid EV battery charger," in *2016 IEEE 1st International Conference on Power Electronics, Intelligent Control and Energy Systems (ICPEICES)*, pp. 1–6, Jul. 2016.

[4] F. Musavi, M. Edington, W. Eberle, and W. G. Dunford, "Evaluation and efficiency comparison of front end AC-DC plug-in hybrid charger topologies," *IEEE Transactions on Smart Grid*, vol. 3, no. 1, pp. 413–421, Mar. 2012.

[5] B. P. McGrath, D. G. Holmes, P. J. McGoldrick, and A. D. McIver, "Design of a soft-switched 6-kw battery charger for traction applications," *IEEE Transactions on Power Electronics*, vol. 22, no. 4, pp. 1136–1144, Jul. 2007.

[6] C. C. Chan and K. T. Chau, "Power electronics challenges in electric vehicles," in *Industrial Electronics, Control, and Instrumentation, 1993. Proceedings of the IECON '93., International Conference on*, pp. 701–706 vol.2, Nov. 1993.

[7] I. A. Khan, "Battery chargers for electric and hybrid vehicles," in *Proceedings of 1994 IEEE Workshop on Power Electronics in Transportation*, pp. 103–112, Oct. 1994.

[8] J. C. Gomez and M. M. Morcos, "Impact of EV battery chargers on the power quality of distribution systems," *IEEE Transactions on Power Delivery*, vol. 18, no. 3, pp. 975–981, Jul. 2003.

[9] F. L. Mapelli, D. Tarsitano, and M. Mauri, "Plug-in hybrid electric vehicle: Modeling, prototype realization, and inverter losses reduction analysis," *IEEE Transactions on Industrial Electronics*, vol. 57, no. 2, pp. 598–607, Feb. 2010.

[10] M. M. Morcos, N. G. Dillman, and C. R. Mersman, "Battery chargers for electric vehicles," *IEEE Power Engineering Review*, vol. 20, no. 11, pp. 8–11, 18, Nov. 2000.

[11] J. Dixon, I. Nakashima, E. F. Arcos, and M. Ortuzar, "Electric vehicle using a combination of ultracapacitors and ZEBRA battery," *IEEE Transactions on Industrial Electronics*, vol. 57, no. 3, pp. 943–949, Mar. 2010.

[12] Z. Amjadi and S. S. Williamson, "Power-electronics-based solutions for plug-in hybrid electric vehicle energy storage and management systems," *IEEE Transactions on Industrial Electronics*, vol. 57, no. 2, pp. 608–616, Feb. 2010.

[13] S. Bala, T. Tengnr, P. Rosenfeld, and F. Delince, "The effect of low frequency current ripple on the performance of a lithium iron phosphate LFP battery energy storage system," in *2012 IEEE Energy Conversion Congress and Exposition (ECCE)*, pp. 3485–3492, Sep. 2012.

[14] H. Z. Z. Beh, G. A. Covic, and J. T. Boys, "Effects of pulse and DC charging on lithium iron phosphate (LiFePO4) batteries," *2013 Ieee Ecce*, pp. 315–320, 2013.

[15] S. Haghbin, S. Lundmark, M. Alakula, and O. Carlson, "Grid-connected integrated battery chargers in vehicle applications: Review and new solution," *IEEE Transactions on Industrial Electronics*, vol. 60, no. 2, pp. 459–473, Feb. 2013.

[16] K. M. S. Y. Konara and M. L. Kolhe, "Charging management of grid integrated battery for overcoming the intermittency of re sources," in *2016 IEEE International Conference on Information and Automation for Sustainability (ICIAfS)*, pp. 1–6, Dec. 2016.

[17] L. Shi, A. Meintz, and M. Ferdowsi, "Single-phase bidirectional AC-DC converters for plug-in hybrid electric vehicle applications," in *2008 IEEE Vehicle Power and Propulsion Conference*, pp. 1–5, Sep. 2008.

[18] *SAE Electric Vehicle and Plug-in Hybrid Electric Vehicle Conductive Charge Coupler, SAE Std. J1772, 2010*.

[19] M. Grenier, M. G. H. Aghdam, and T. Thiringer, "Design of on-board charger for plug-in hybrid electric vehicle," in *5th IET International Conference on Power Electronics, Machines and Drives (PEMD 2010)*, pp. 1–6, Apr. 2010.

[20] M. Yilmaz and P. T. Krein, "Review of battery charger topologies, charging power levels, and infrastructure for plug-in electric and hybrid vehicles," *IEEE Transactions on Power Electronics*, vol. 28, no. 5, pp. 2151–2169, May. 2013.

[21] O. C. Onar, J. Kobayashi, D. C. Erb, and A. Khaligh, "A bidirectional high-power-quality grid interface with a novel bidirectional noninverted buck-boost converter for PHEVs," *IEEE Transactions on Vehicular Technology*, vol. 61, no. 5, pp. 2018–2032, Jun. 2012.

[22] J. C. Bendien, G. Fregien, and J. D. van Wyk, "High-efficiency on-board battery charger with transformer isolation, sinusoidal input current and maximum power factor," *IEE Proceedings B - Electric Power Applications*, vol. 133, no. 4, pp. 197–204, Jul. 1986.

[23] M. Pahlevaninezhad, P. Das, J. Drobnik, P. K. Jain, and A. Bakhshai, "A new control approach based on the differential flatness theory for an AC/DC converter used in electric vehicles," *IEEE Transactions on Power Electronics*, vol. 27, no. 4, pp. 2085–2103, Apr. 2012.

[24] A. K. Verma, B. Singh, and D. T. Shahani, "Grid to vehicle and vehicle to grid energy transfer using single-phase bidirectional ac-dc converter and bidirectional dc-dc converter," in *2011 International Conference on Energy, Automation and Signal*, pp. 1–5, Dec. 2011.

[25] A. K. Singh, M. K. Pathak, and Y. S. Rao, "A new two-stage converter with reduction of DC-link capacitor for plug-in electric vehicle battery charger," in *2017 3rd International Conference on Computational Intelligence Communication Technology (CICT)*, pp. 1–6, Feb. 2017.

[26] M. G. Egan, D. L. O'Sullivan, J. G. Hayes, M. J. Willers, and C. P. Henze, "Power-factor-corrected single-stage inductive charger for electric vehicle batteries," *IEEE Transactions on Industrial Electronics*, vol. 54, no. 2, pp. 1217–1226, Apr. 2007.

[27] D. Patil, M. Sinha, and V. Agarwal, "A Cuk converter based bridgeless topology for high power factor fast battery charger for electric vechicle application," in *2012 IEEE Transportation Electrification Conference and Expo (ITEC)*, pp. 1–6, Jun. 2012.

[28] D. Patil and V. Agarwal, "Compact onboard single-phase EV battery charger with novel low-frequency ripple compensator and optimum filter design," *IEEE Transactions on Vehicular Technology*, vol. 65, no. 4, pp. 1948–1956, Apr. 2016.

[29] P. Y. Kong, J. A. Aziz, M. R. Sahid, and L. W. Yao, "A bridgeless PFC converter for on-board battery charger," in *2014 IEEE Conference on Energy Conversion (CENCON)*, pp. 383–388, Oct. 2014.

[30] C.-Y. Oh, D.-H. Kim, D.-G. Woo, W.-Y. Sung, Y.-S. Kim, and B.-K. Lee, "A high-efficient nonisolated single-stage on-board battery charger for electric vehicles," *IEEE Transactions on Power Electronics*, vol. 28, no. 12, pp. 5746–5757, Dec. 2013.

[31] S. Haghbin, S. Lundmark, M. Alakula, and O. Carlson, "Grid-connected integrated battery chargers in vehicle applications: Review and new solution," *IEEE Transactions on Industrial Electronics*, vol. 60, no. 2, pp. 459–473, Feb. 2013.

[32] J.-S. Kim, G.-Y. Choe, H.-M. Jung, B.-K. Lee, Y.-J. Cho, and K.-B. Han, "Design and implementation of a high-efficiency on- board battery charger for electric vehicles with frequency control strategy," in *2010 IEEE Vehicle Power and Propulsion Conference*, pp. 1–6, Sep. 2010.

[33] I. Aharon and A. Kuperman, "Topological overview of powertrains for battery-powered vehicles with range extenders," *IEEE Transactions on Power Electronics*, vol. 26, no. 3, pp. 868–876, Mar. 2011.

[34] C. Liu, B. Gu, J. S. Lai, M. Wang, Y. Ji, G. Cai, Z. Zhao, C. L. Chen, C. Zheng, and P. Sun, "High-efficiency hybrid full-bridge-half-bridge converter with shared ZVS lagging leg and dual outputs in series," *IEEE Transactions on Power Electronics*, vol. 28, no. 2, pp. 849–861, Feb. 2013.

[35] Y. Du, S. Lukic, B. Jacobson, and A. Huang, "Review of high power isolated bi-directional DC-DC converters for PHEV/EV DC charging infrastructure," in *2011 IEEE Energy Conversion Congress and Exposition*, pp. 553–560, Sep. 2011.

[36] E. Sortomme and M. A. El-Sharkawi, "Optimal charging strategies for unidirectional vehicle-to-grid," *IEEE Transactions on Smart Grid*, vol. 2, no. 1, pp. 131–138, Mar. 2011.

[37] F. Musavi, W. Eberle, and W. G. Dunford, "A high-performance single-phase bridgeless interleaved PFC converter for plug-in hybrid electric vehicle battery chargers," *IEEE Transactions on Industry Applications*, vol. 47, no. 4, pp. 1833–1843, Jul. 2011.

[38] A. K. Singh, M. K. Pathak, and Y. S. Rao, "A multi-device front-end power factor converter for EV battery charger," in *2017 3rd International Conference on Computational Intelligence Communication Technology (CICT)*, pp. 1–6, Feb. 2017.

[39] C. Shi, H. Wang, S. Dusmez, and A. Khaligh, "A SiC-based high-efficiency isolated onboard PEV charger with ultrawide dc-link voltage range," *IEEE Transactions on Industry Applications*, vol. 53, no. 1, pp. 501–511, Jan. 2017.

[40] M. Pahlevaninezhad, P. Das, J. Drobnik, P. K. Jain, and A. Bakhshai, "A ZVS interleaved boost AC/DC converter used in plug-in electric vehicles," *IEEE Transactions on Power Electronics*, vol. 27, no. 8, pp. 3513–3529, Aug. 2012.

[41] "Combined motor drive and battery recharge system," U.S. patentus 5 341 075, 1994.

[42] "AC propulsion EV drive system specifications, 2008. AC propulsion inc. technical note." Tech. Rep.

[43] "Integrated traction inverter and battery charger apparatus," U.S. patentus 4 920 475, Apr., 1990.

[44] "Integrated motor drive and recharge system," U.S. patentus 5 099 186,, Mar. 24, 1992.

[45] L. D. Sousa, B. Silvestre, and B. Bouchez, "A combined multiphase electric drive and fast battery charger for electric vehicles," in *2010 IEEE Vehicle Power and Propulsion Conference*, pp. 1–6, Sep. 2010.

[46] A. Bruyre, L. D. Sousa, B. Bouchez, P. Sandulescu, X. Kestelyn, and E. Semail, "A multiphase traction/fast-battery-charger drive for electric or plug-in hybrid vehicles: Solutions for control in traction mode," in *2010 IEEE Vehicle Power and Propulsion Conference*, pp. 1–7, Sep. 2010.

[47] S. Lacroix, E. Laboure, and M. Hilairet, "An integrated fast battery charger for electric vehicle," in *2010 IEEE Vehicle Power and Propulsion Conference*, pp. 1–6, Sep. 2010.

[48] L. De-Sousa and B. Bouchez, "Combined electric device for powering and charging," patentus WO 2010/057 892 A1, May, 2010.

[49] L. De-Sousa and B. Bouchez,, "Method and electric combined device for powering and charging with compensation means," patentus WO 2010/057 893 A1, May, 2010.

[50] H. C. Chang and C. M. Liaw, "Development of a compact switched-reluctance motor drive for EV propulsion with voltage-boosting and PFC charging capabilities," *IEEE Transactions on Vehicular Technology*, vol. 58, no. 7, pp. 3198–3215, Sep. 2009.

[51] C. Gan, J. Wu, Y. Hu, S. Yang, W. Cao, and J. M. Guerrero, "New integrated multilevel converter for switched reluctance motor drives in plug-in hybrid electric vehicles with flexible energy conversion," *IEEE Transactions on Power Electronics*, vol. 32, no. 5, pp. 3754–3766, May. 2017.

[52] C. Shi, Y. Tang, and A. Khaligh, "A single-phase integrated onboard battery charger using propulsion system for plug-in electric vehicles," *IEEE Transactions on Vehicular Technology*, vol. PP, no. 99, pp. 1–1, 2017.

[53] I. Subotic, N. Bodo, and E. Levi, "An EV drive-train with integrated fast charging capability," *IEEE Transactions on Power Electronics*, vol. 31, no. 2, pp. 1461–1471, Feb. 2016.

[54] I. Subotic, N. Bodo, E. Levi, and M. Jones, "Onboard integrated battery charger for EVs using an asymmetrical nine-phase machine," *IEEE Transactions on Industrial Electronics*, vol. 62, no. 5, pp. 3285–3295, May. 2015.

[55] I. Subotic, N. Bodo, E. Levi, M. Jones, and V. Levi, "Isolated chargers for EVs incorporating six-phase machines," *IEEE Transactions on Industrial Electronics*, vol. 63, no. 1, pp. 653–664, Jan. 2016.

[56] I. Subotic, N. Bodo, and E. Levi, "Single-phase on-board integrated battery chargers for EVs based on multiphase machines," *IEEE Transactions on Power Electronics*, vol. 31, no. 9, pp. 6511–6523, Sep. 2016.

[57] I. Subotic, E. Levi, and N. Bodo, "A fast on-board integrated battery charger for EVs using an asymmetrical six-phase machine," in *2014 IEEE Vehicle Power and Propulsion Conference (VPPC)*, pp. 1–6, Oct. 2014.

[58] S. K. Biswas, C. Chakraborty, B. Basak, and D. P. S. Gupta, "Performance analysis of an asymmetrical phase-converter-fed induction motor," *IEEE Transactions on Industry Applications*, vol. 34, no. 5, pp. 1049–1058, Sep. 1998.

[59] S. Taghavi and P. Pillay, "A comparative study of synchronous reluctance machine performance with different pole numbers for automotive applications," in *IECON 2014 - 40th Annual Conference of the IEEE Industrial Electronics Society*, pp. 3812–3818, Oct. 2014.

[60] Q. Zheng, J. X. Xu, and S. K. Panda, "A study on torque modelling of switched reluctance motors," in *2013 American Control Conference*, pp. 321–326, Jun. 2013.

[61] B. K. Bose, *Motion Control with Induction Motors*. Wiley-IEEE Press, 1997.

[62] B. K. Bose, *Modern Power Electronics and AC Drive*. Prentice Hall PTR, 2002.

[63] A. K. Singh, A. Dalal, and P. Kumar, "Analysis of induction motor for electric vehicle application based on drive cycle analysis," in *2014 IEEE International Conference on Power Electronics, Drives and Energy Systems (PEDES)*, pp. 1–6, Dec. 2014.

[64] C.-M. Ta, C. Chakraborty, and Y. Hori, "Efficiency maximization of induction motor drives for electric vehicles based on actual measurement of input power," in *Industrial Electronics Society, 2001. IECON '01. The 27th Annual Conference of the IEEE*, vol. 3, pp. 1692–1697 vol.3, 2001.

[65] S. K. Panda, J.-X. Xu, and W. Qian, "Review of torque ripple minimization in PM synchronous motor drives," in *2008 IEEE Power and Energy Society General Meeting - Conversion and Delivery of Electrical Energy in the 21st Century*, pp. 1–6, Jul. 2008.

[66] G. Xie, K. Lu, S. K. Dwivedi, J. R. Rosholm, and F. Blaabjerg, "Minimum-voltage vector injection method for sensorless control of PMSM for low-speed operations," *IEEE Transactions on Power Electronics*, vol. 31, no. 2, pp. 1785–1794, Feb. 2016.

[67] R. K. Singh and S. Mishra, "A magnetically coupled feedback-clamped optimal bidirectional battery charger," *IEEE Transactions on Industrial Electronics*, vol. 60, no. 2, pp. 422–432, Feb. 2013.

[68] V. Chitransh, A. Singh, and R. K. Singh, "A clamped feedback based digital versatile optimal bidirectional battery charger for HEV/PHEV," in *2015 IEEE 11th International Conference on Power Electronics and Drive Systems*, pp. 1138–1143, Jun. 2015.

[69] A. Ahmed, M. A. Khan, M. Badawy, Y. Sozer, and I. Husain, "Performance analysis of bi-directional DC-DC converters for electric vehicles and charging infrastructure," in *2013 IEEE Energy Conversion Congress and Exposition*, pp. 1401–1408, Sep. 2013.

[70] A. Choudhury, P. Pillay, and S. S. Williamson, "Comparative analysis between two-level and three-level DC/AC electric vehicle traction inverters using a novel DC-link voltage balancing algorithm," *IEEE Journal of Emerging and Selected Topics in Power Electronics*, vol. 2, no. 3, pp. 529–540, Sep. 2014.

[71] S. Umashankar, V. K. A. Shankar, G. Jain, and M. L. Kolhe, "Comparative evaluation of pulse width modulation techniques on effective dc link voltage utilization of grid connected inverter," in *2016 International Conference on Electrical, Electronics, and Optimization Techniques (ICEEOT)*, pp. 2376–2383, Mar. 2016.

[72] T. Roy, N. Aarzoo, P. K. Sadhu, C. Jena, and S. Mohapatra, "A novel symmetrical switched capacitor based three-phase cascaded multi-level inverter," in *2016 IEEE International Conference on Power Electronics, Drives and Energy Systems (PEDES)*, pp. 1–6, Dec. 2016.

[73] A. B. Shitole, H. M. Suryawanshi, G. G. Talapur, and S. Sathyan, "Performance improvement of grid interfaced three level diode clamped inverter under various power quality events," in *2017 IEEE 26th International Symposium on Industrial Electronics (ISIE)*, pp. 821–826, Jun. 2017.

[74] W. Qian, H. Cha, F. Z. Peng, and L. M. Tolbert, "55-kW variable 3X DC-DC converter for plug-in hybrid electric vehicles," *IEEE Transactions on Power Electronics*, vol. 27, no. 4, pp. 1668–1678, Apr. 2012.

[75] T. Park and T. Kim, "Novel energy conversion system based on a multimode single-leg power converter," *IEEE Transactions on Power Electronics*, vol. 28, no. 1, pp. 213–220, Jan. 2013.

[76] A. K. Sahoo, R. Otero-De-Leon, and N. Mohan, "Review of modular multilevel converters for teaching a graduate-level course of power electronics in power systems," in *2013 North American Power Symposium (NAPS)*, pp. 1–6, Sep. 2013.

[77] S. Rodrigues, A. Papadopoulos, E. Kontos, T. Todorcevic, and P. Bauer, "Steady-state loss model of half-bridge modular multilevel converters," *IEEE Transactions on Industry Applications*, vol. 52, no. 3, pp. 2415–2425, May. 2016.

[78] S. Karmakar, T. Roy, P. K. Sadhu, and S. Mondal, "Analysis and simulation of a new topology of single phase multi-level inverter," in *2016 IEEE 1st International Conference on Power Electronics, Intelligent Control and Energy Systems (ICPEICES)*, pp. 1–6, Jul. 2016.

[79] H. M. Suryawanshi, K. L. Thakre, S. G. Tarnekar, D. P. Kothari, and A. G. Kothari, "Power factor improvement and closed loop control of an AC-to-DC resonant converter," *IEE Proceedings - Electric Power Applications*, vol. 149, no. 2, pp. 101–110, Mar. 2002.

[80] P. F. de Melo, R. Gules, E. F. R. Romaneli, and R. C. Annunziato, "A modified SEPIC converter for high-power-factor rectifier and universal input voltage applications," *IEEE Transactions on Power Electronics*, vol. 25, no. 2, pp. 310–321, Feb. 2010.

[81] W. Wei, L. Hongpeng, J. Shigong, and X. Dianguo, "A novel bridgeless buck-boost PFC converter," in *2008 IEEE Power Electronics Specialists Conference*, pp. 1304–1308, Jun. 2008.

[82] J. W. Yang and H. L. Do, "Bridgeless SEPIC converter with a ripple-free input current," *IEEE Transactions on Power Electronics*, vol. 28, no. 7, pp. 3388–3394, Jul. 2013.

[83] Y. Jang and M. M. Jovanovic, "Interleaved boost converter with intrinsic voltage-doubler characteristic for universal-line PFC front end," *IEEE Transactions on Power Electronics*, vol. 22, no. 4, pp. 1394–1401, Jul. 2007.

[84] A. M. A. Gabri, A. A. Fardoun, and E. H. Ismail, "Bridgeless PFC-modified SEPIC rectifier with extended gain for universal input voltage applications," *IEEE Transactions on Power Electronics*, vol. 30, no. 8, pp. 4272–4282, Aug. 2015.

[85] A. A. Fardoun, E. H. Ismail, N. M. Khraim, A. J. Sabzali, and M. A. Al-Saffar, "Bridgeless high-power-factor buck-converter operating in discontinuous capacitor voltage mode," *IEEE Transactions on Industry Applications*, vol. 50, no. 5, pp. 3457–3467, Sep. 2014.

[86] E. H. Ismail, "Bridgeless SEPIC rectifier with unity power factor and reduced conduction losses," *IEEE Transactions on Industrial Electronics*, vol. 56, no. 4, pp. 1147–1157, Apr. 2009.

[87] B. Singh, B. N. Singh, A. Chandra, K. Al-Haddad, A. Pandey, and D. P. Kothari, "A review of single-phase improved power quality AC-DC converters," *IEEE Transactions on Industrial Electronics*, vol. 50, no. 5, pp. 962–981, Oct. 2003.

[88] B. Singh, B. P. Singh, and S. Dwivedi, "Improved power quality ac-dc flyback converter for variable speed permanent magnet synchronous motor drive," in *2006 IEEE Power India Conference*, pp. 8 pp.–, Apr. 2006.

[89] B. Singh, S. Singh, A. Chandra, and K. Al-Haddad, "Comprehensive study of single-phase AC-DC power factor corrected converters with high-frequency isolation," *IEEE Transactions on Industrial Informatics*, vol. 7, no. 4, pp. 540–556, Nov. 2011.

[90] A. K. Singh and M. K. Pathak, "An improved two-stage non-isolated converter for on-board plug-in hybrid EV battery charger," in *2016 IEEE 1st International Conference on Power Electronics, Intelligent Control and Energy Systems (ICPEICES)*, pp. 1–6, Jul. 2016.

[91] S. Singh, B. Singh, G. Bhuvaneswari, and V. Bist, "Power factor corrected Zeta converter based improved power quality switched mode power supply," *IEEE Transactions on Industrial Electronics*, vol. 62, no. 9, pp. 5422–5433, Sep. 2015.

[92] V. Bist, B. Singh, A. Chandra, and K. Al-Haddad, "An adjustable speed PFC bridgeless-SEPIC fed brushless DC motor drive," in *2015 IEEE Energy Conversion Congress and Exposition (ECCE)*, pp. 4886–4893, Sep. 2015.

[93] B. Singh, B. P. Singh, and S. Dwivedi, "Performance comparison of high frequency isolated AC-DC converters for power quality improvement at input AC mains," in *2006 International Conference on Power Electronic, Drives and Energy Systems*, pp. 1–6, Dec. 2006.

[94] S. S. Tanavade, H. M. Suryawanshi, and K. L. Thakre, "Novel single-phase AC-to-DC convertor using three-phase modified series-parallel resonant convertor," *IEE Proceedings - Electric Power Applications*, vol. 152, no. 4, pp. 1027–1035, Jul. 2005.

[95] Y. J. Lee, A. Khaligh, and A. Emadi, "Advanced integrated bidirectional AC/DC and DC/DC converter for plug-in hybrid electric vehicles," *IEEE Transactions on Vehicular Technology*, vol. 58, no. 8, pp. 3970–3980, Oct. 2009.

[96] H. Chen, X. Wang, and A. Khaligh, "A single stage integrated bidirectional ac/dc and dc/dc converter for plug-in hybrid electric vehicles," in *2011 IEEE Vehicle Power and Propulsion Conference*, pp. 1–6, Sep. 2011.

[97] Dusmez, Serkan and Khaligh, Alireza, "A novel low cost integrated on-board charger topology for electric vehicles and plug-in hybrid electric vehicles," *Conference Proceedings - IEEE Applied Power Electronics Conference and Exposition - APEC*, pp. 2611–2616, 2012.

[98] S. Dusmez and A. Khaligh, "A compact and integrated multifunctional power electronic interface for plug-in electric vehicles," *IEEE Transactions on Power Electronics*, vol. 28, no. 12, pp. 5690–5701, Dec. 2013.

[99] S. Dusmez and A. Khaligh, "A charge-nonlinear-carrier-controlled reduced-part single-stage integrated power electronics interface for automotive applications," *IEEE Transactions on Vehicular Technology*, vol. 63, no. 3, pp. 1091–1103, Mar. 2014.

[100] Y. Tang, D. Zhu, C. Jin, P. Wang, and F. Blaabjerg, "A three-level quasi-two-stage single-phase PFC converter with flexible output voltage and improved conversion efficiency," *IEEE Transactions on Power Electronics*, vol. 30, no. 2, pp. 717–726, Feb. 2015.

[101] B. Sahu and G. A. Rincon-Mora, "A low voltage, dynamic, noninverting, synchronous buck-boost converter for portable applications," *IEEE Transactions on Power Electronics*, vol. 19, no. 2, pp. 443–452, Mar. 2004.

[102] V. Vlatkovic, D. Borojevic, and F. C. Lee, "Input filter design for power factor correction circuits," *IEEE Transactions on Power Electronics*, vol. 11, no. 1, pp. 199–205, Jan. 1996.

[103] M. Mahdavi and H. Farzanehfard, "Bridgeless SEPIC PFC rectifier with reduced components and conduction losses," *IEEE Transactions on Industrial Electronics*, vol. 58, no. 9, pp. 4153–4160, 2011.

[104] S. Singh, B. Singh, G. Bhuvaneswari, and V. Bist, "A power quality improved bridgeless converter-based computer power supply," *IEEE Transactions on Industry Applications*, vol. 52, no. 5, pp. 4385–4394, Sep. 2016.

[105] D. Hart, *Power Electronics*. McGraw-Hill, 2011.

[106] T. M. U. N. Mohan and W. P. Robbins, *Power Electronics: Converters, Applications and Design*. New York, NY, USA: Wiley, 2009.

[107] M. H. Rashid, *Power Electronics Handbook*. Academic Press, 2001.

[108] W. Tang, F. C. Lee, and R. B. Ridley, "Small-signal modeling of average current-mode control," *IEEE Transactions on Power Electronics*, vol. 8, no. 2, pp. 112–119, Apr. 1993.

[109] G. Sen and M. E. Elbuluk, "Voltage and current-programmed modes in control of the Z-source converter," *IEEE Transactions on Industry Applications*, vol. 46, no. 2, pp. 680–686, Mar. 2010.

[110] V. S. C. Raviraj and P. C. Sen, "Comparative study of proportional-integral, sliding mode, and fuzzy logic controllers for power converters," *IEEE Transactions on Industry Applications*, vol. 33, no. 2, pp. 518–524, Mar. 1997.

[111] H. S. Youn, J. S. Park, K. B. Park, J. I. Baek, and G. W. Moon, "A digital predictive peak current control for power factor correction with low-input current distortion," *IEEE Transactions on Power Electronics*, vol. 31, no. 1, pp. 900–912, Jan. 2016.

[112] M. Marvi and A. Fotowat-Ahmady, "A fully ZVS critical conduction mode boost PFC," *IEEE Transactions on Power Electronics*, vol. 27, no. 4, pp. 1958–1965, Apr. 2012.

[113] R. W. Erickson and D. Maksimovic, *Fundamentals of Power Electronics*, second edition, Ed. Springer, 2005.

[114] K. M. Smedley and S. Cuk, "One-cycle control of switching converters," *IEEE Transactions on Power Electronics*, vol. 10, no. 6, pp. 625–633, Nov. 1995.

[115] Z. Lai, K. M. Smedley, and Y. Ma, "Time quantity one-cycle control for power-factor correctors," *IEEE Transactions on Power Electronics*, vol. 12, no. 2, pp. 369–375, Mar. 1997.

[116] *'http://www.allaboutcircuits.com/technical-articles/basic-inductor-design-constraints/'*.

APPENDIX A

SIMULATION AND EXPERIMENTAL SETUP

This appendix explains about more detail of simulation and experimental setup that have been conducted in order to investigate the performance of the proposed converters in each mode of vehicle operation.

A.1 Simulation Setup

The simulations were conducted in MATLAB/Simulink environment. MATLAB is widely used as an interactive tool for modeling, analysis and visualization of systems, which itself contains more than 600 mathematical functions and supports additional toolboxes to make it more comprehensive. Simulink is a MATLAB add-on software that enables block diagram based modeling and analysis of linear, nonlinear, discrete, and continuous and hybrid systems. The power circuit of the proposed topologies has been modeled using SimPowerSystems toolbox of 2013a MATLAB version. The control circuit has been developed using 'Math Operations', 'Signal Routing, 'Discrete', 'Sink' and 'Source' blocks of Simulink. The simulation sample time has been kept $1e^{-6}s$ for the execution of power circuit.

A.2 Experimental Setup

The prototype model of experimental setup and its block diagram are shown in Fig. A.1 and A.2, respectively. The PWM signal for MOSFET (IRFP460) switches is applied through FPGA based controller dSPACE-1104 which has been interfaced with desktop computer (A.3(a)). The dSPACE-1104 has 8 ADC/DAC channels, as shown in Fig. A.3(b) which has two operating modes, i.e., Master and Slave. For higher switching frequency (5-30 kHz) operation, Slave mode is used, while for low switching frequency range (0-5 kHz), Master

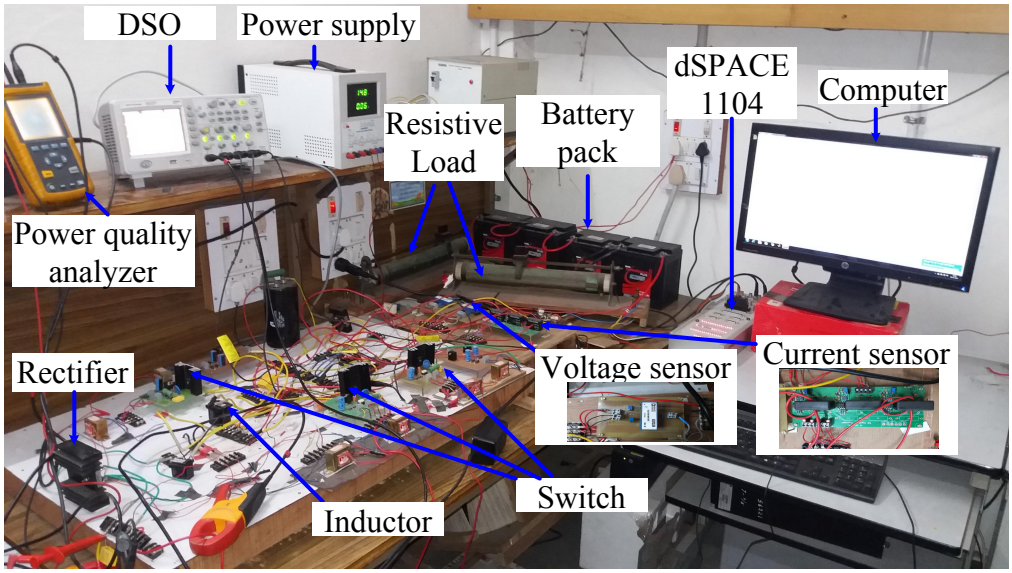

Fig. A.1. Photo of experimental setup

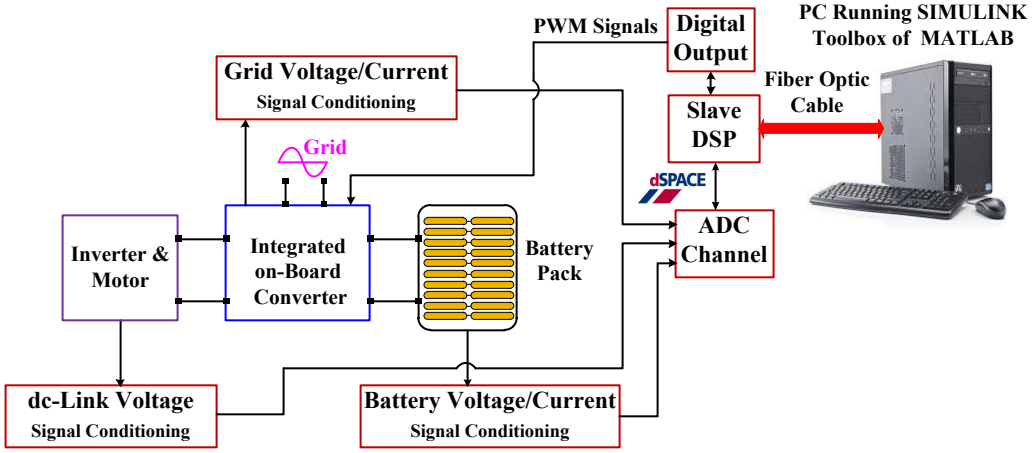

Fig. A.2. Block diagram of experimental setup

mode is used. A single-phase variac shown in Fig. A.3(c) has output voltage range of 0-260 V, which is used during plug-in charging and regenerative braking modes. In regenerative braking mode, the variac is used to form a dc-link by utilizing a rectifier and a large capacitor (4700μF). In Fig. A.3 (d), the battery stack of four units is shown and rating of each unit is 12 V, 26 Ah. For powering the voltage and current sensors, a Scientific multiple power supply PSD 3304 is used which has three supply terminals as: +30 V/2 A, 5 V/ 5 A and $\pm$15 V/ 1 A. All experimental waveforms are recorded in Agilent Technology, DSO1014A, as shown in Fig. A.3(e). In the following Sections, development of MOSFET driver circuit and measurement circuits, i.e., voltage and current sensors are discussed.

A.2.1 MOSFET driver

A circuit diagram the MOSFET driver is made using 8-pin TLP 250 optocoupler which can be operated upto 25 kHz of switching frequency . However, in this research, the switching frequency was selected as 20 kHz. The driver circuit comprises of + 15 V supply, TLP optocoupler and voltage protection for switch shown in Fig. A.4(a). The PWM pulses from the controller are fed between second and third terminals of TLP optocoupler and magnified PWM pulses are taken at output terminal seven which is connected to gate terminal of the switch. The printed cicuit board (PCB) layout and photograph of driver circuit for experimental setup are shown in Figs. A.4(b) and (c), respectively.

A.2.2 Voltage sensor

The voltages (ac or dc) are sensed to through AD202JN isolation amplifier which is powered by $+$15 V supply. In addition, two potentiometers and two resistances are used for the operation of sensing circuit. The main features of AD202JN are: 1) small physical size, 2) High accuracy, 3) Low power consumption and 4) Wide bandwidth. Fig. A.5(a) shows a cicuit diagram of voltage sensor where sensed voltage is at output terminal 19 of AD202JN. The output of voltage sensor is scaled properly to meet the requirement of the control circuit and is fed to the dSPACE via its ADC channel for further processing. The PCB layout and photograph of voltage sensor for experimental setup are shown in Figs. A.5(b) and (c), respectively.

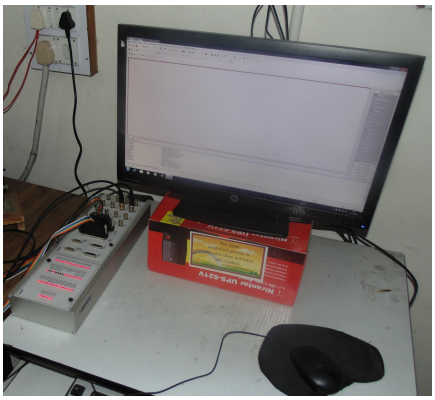

(a) Computer

(b) dSPACE Kit

(c) Single-phase auto transformer

(d) battery pack

(e) Multiple power supply

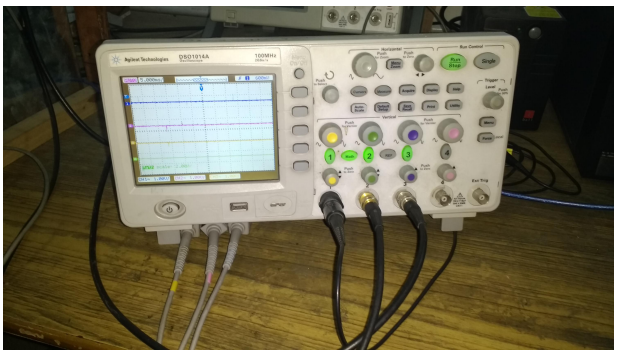

(f) DSO

(g) Power quality analyzer

Fig. A.3. Discrete components of experimental setup

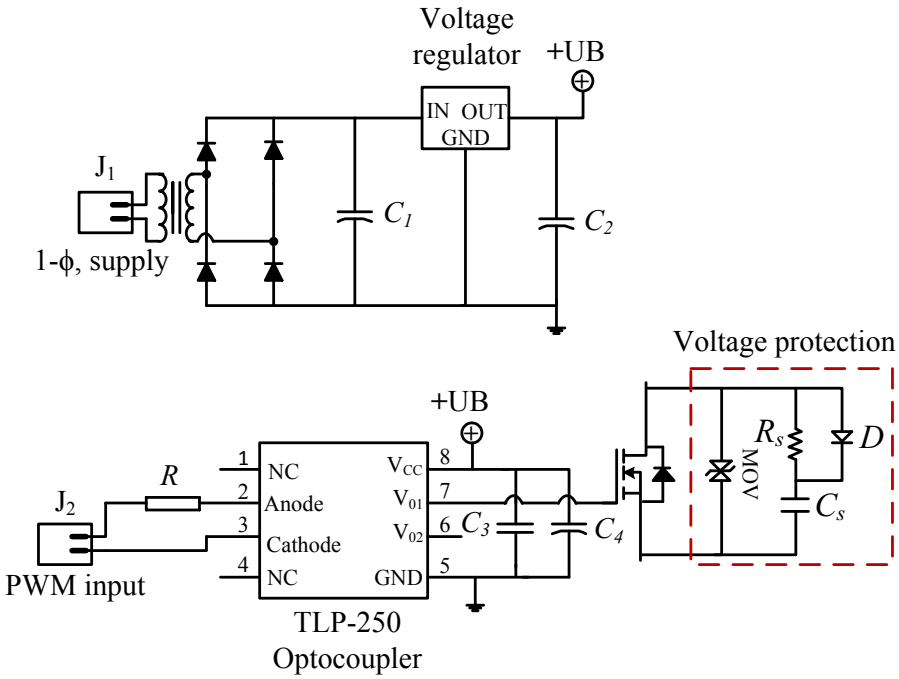

(a)

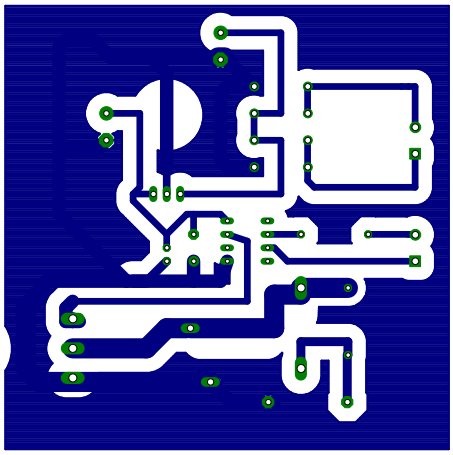

(b)

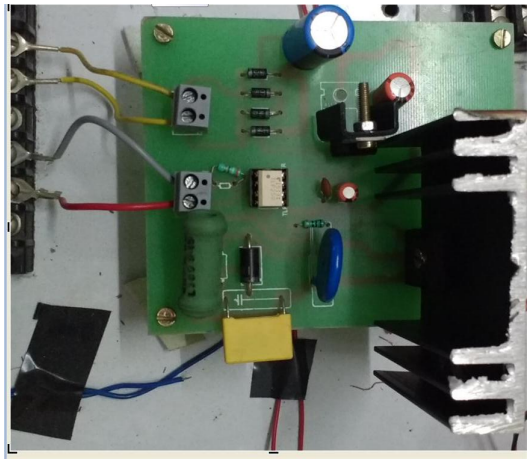

(c)

Fig. A.4. (a) Cicuit diagram of MOSFET driver using TLP-250 Optocoupler, (b) PCB layout of driver circuit, (c) photo of driver cicuit for experimental setup

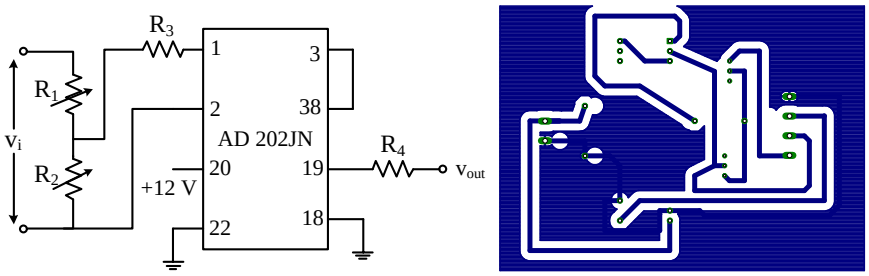

(a) (b)

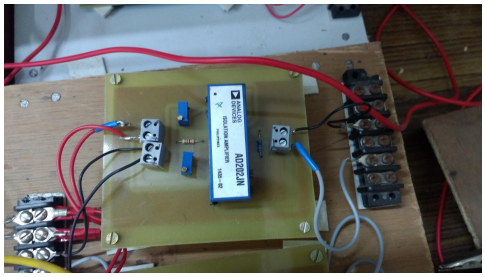

(c)

Fig. A.5. (a) Circuit diagram of voltage sensor using AD202JN, (b) PCB layout of voltage sensor, (c) photo of voltage sensor in experimental setup

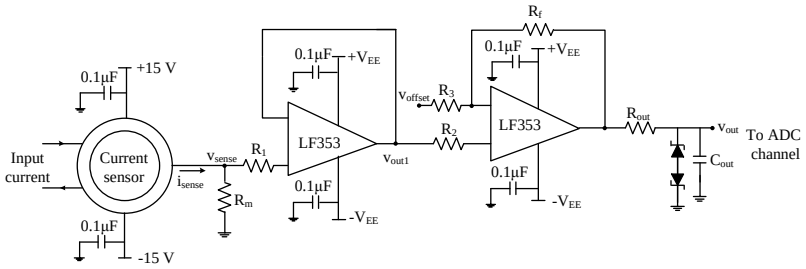

(a)

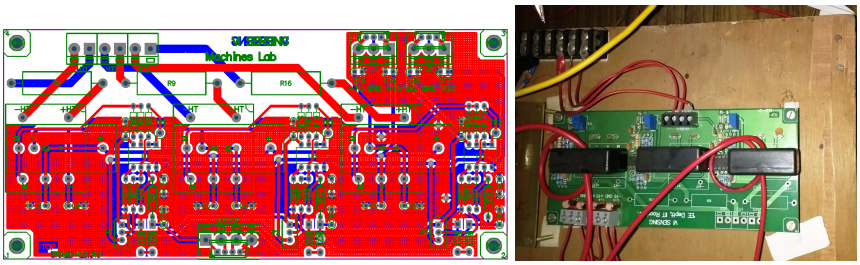

(b) (c)

Fig. A.6. (a) Cicuit diagram of current sensor using TELCON HTP25, (b) PCB layout of current sensor, (c) photo of current sensor in experimental setup

A.2.3 Current sensor

The ac or dc current is sensed using Hall effect sensor (TELCON HTP25). The HTP25 is Hall effect current transformer suitable for measuring current up to 25 A. The current sensors provide the galvanic isolation between the high voltage power circuit and the low voltage control circuit and require a nominal supply voltage of the range $\pm$ 12V to $\pm$ 15V. A dual supply based two operation amplifiers (LF353) is used to convert current signal into voltage signal and scales down the voltage signal at a required magnitude for ADC channel. A PCB layout of current sensor and photo of current sensor for experimental setup are shown in Figs. A.6 (b) and (c), respectively.

APPENDIX B

LIST OF PUBLICATIONS

JOURNALS

1. A. K. Singh and M. K. Pathak, "Single-Phase Bidirectional ac/dc Converter for Plug-in Electric Vehicles with Reduced Conduction Losses," *IET Power Electronics*, vol. 11, no. 1, pp. 140–148, 2018.

2. A. K. Singh and M. K. Pathak, "A Single-Stage ZETA-SEPIC Based Multifunctional Integrated Converter for Plug-in Electric Vehicles," *IET Electrical System in Transportation*, vol. 8, no. 2, pp. 101–111, 2018.

3. A. K. Singh and M. K. Pathak, "A Multifunctional Single-Stage Power Electronic Interface for Plug-in Electric Vehicles Application", *Electrical Power components and Systems*, vol. 46, no. 2, pp. 135–148, 2018.

4. A. K. Singh and M. K. Pathak, "A Non-Linear Carrier Control Based Compact Converter For Plug-in Electric Vehicles",*IEEE Transaction on Industrial Informatics* (Accepted with minor revision).

CONFERENCES

5. A. K. Singh, M. K. Pathak, and Y. S. Rao, "A New Two-Stage Converter with Reduction of dc-link Capacitor for Plug-in Electric Vehicle Battery Charger," in *2017 3rd International Conference on Computational Intelligence Communication Technology (CICT)*, pp. 1–6, Feb. 2017.

6. A. K. Singh and M. K. Pathak, "An Improved Two-Stage Non-isolated Converter for On-board Plug-in Hybrid EV Battery Charger," in *2016 IEEE 1st International Conference on Power Electronics, Intelligent Control and Energy Systems (ICPEICES)*, pp. 1–6, Jul. 2016.

7. A. K. Singh, M. K. Pathak, and Y. S. Rao, “A Multi-Device Front-end Power Factor Converter For EV Battery Charger,” in *2017 3rd International Conference on Computational Intelligence Communication Technology (CICT)*, pp. 1–6, Feb. 2017.

8. A. K. Singh and M. K. Pathak “A Comprehensive Review of Integrated Charger for On-board Battery Charging Applications of Electric Vehicles: Topology,” *Electrical Power and Energy Conference*, Toronto, Canada (Under Review)